The Dissertation Committee for David Paul Ostrowski Certifies that this is the approved version of the following dissertation:

Methods Development and Measurements for Understanding Morphological Effects on Electronic and Optical Properties in Solution Processable Photovoltaic Materials

Committee:

David A. Vanden Bout, Supervisor

Peter J. Rossky

Bradley J. Holliday

Brian A. Korgel

Ananth J. Dodabalapur

Methods Development and Measurements for Understanding Morphological Effects on Electronic and Optical Properties in Solution Processable Photovoltaic Materials

by

David Paul Ostrowski, B. A.

Dissertation

Presented to the Faculty of the Graduate School of

The University of Texas at Austin

in Partial Fulfillment

of the Requirements

for the Degree of

Doctor of Philosophy

The University of Texas at Austin

December, 2012

Dedication

To my parents, brother and sister.

Acknowledgements

I have always considered it a great privilege to have the opportunity to research solar energy at The University of Texas at Austin. The experience of living in Austin, TX and working toward this degree has allowed for a lot of personal and professional growth. I have been fortunate to interact and learn from many great professors and students, along with experiencing the fun-loving character and open-minded culture of Austin, TX.

I want to thank my advisor David Vanden Bout for being my research mentor over the years of this doctorate degree. His ability to explain complicated phenomenon in understandable ways is unprecedented. He was almost always up for a scientific discussion and he repeatedly helped me to see the forest while I was focusing too much on the trees or in some cases even the branches and leaves. There have also been many Vanden Bout Lab group members that contributed to this work: Craig Cone, Katie Clark, Micah Glaz, Jon Travis, Takuji Adachi, Zhongjian Hu, Omar Fabian, Johanna Brazard, Jan Vogelsang, Albert Lu, Lynn Rozanski, Yeon-Ho Kim, Joyce-Wei, Joseph Imhoff, Tom Doyle, Matt Wallack and Leigh Kruger to name most of them.

I want to thank a number of professors as well, mainly my dissertation committee members. I was able to collaborate with them and some of their students during my time at UT Austin. These interactions lead to a valuable exchange of knowledge, ideas and most importantly new samples to characterize! Professors: Brian Korgel, Brad Holliday, Ananth Dodabalapur, Peter Rossky, Keith Stevenson and Paul Barbara. Students: Lauren Lytwak, Taylor Harvey, Jackson Stolle, Vahid Akhavan, Brian Goodfellow, Matthew Panthani, Alex Veneman, Christopher Lombardo and Lawrence Dunn.

The staff for the chemistry department also proved invaluable. Tim Hooper provided much needed help in electrical areas that I hardly knew anything about upon

arriving at UT Austin. The machine and glass shop (Terry Watts, Charles Thonig and Michael Ronalter) always had helpful suggestions when I would stop by with a new approach for an instrumental improvement and contributed many gadgets that aided the work. The administrative staff, Penny Kile and Betsy Hamblen, were always supportive and helpful as well.

I want to thank my chemistry professors at Northwestern University for a great undergraduate education and for motivating me towards this path of research. In particular, I would like to thank Professors Franz Geiger, Barry Coddens, Fred Northrup, Ken Poeppelmeier, Eberhard Zwergel and Chad Mirkin. Also, I am thankful for my experiences at Welch Vacuum under the guidance of Dr. John Balamuta and in Professor Stephan Borrmann's lab at the Max-Planck Institute for Chemistry in Mainz, Germany. Through those experiences in an industrial and an academic lab setting, I found an increased motivation to pursue a research career. Also, from the experience in Germany I first learned that it is not always the answers that are most important, one has to be sure to ask the right questions.

Without the support of family and friends I would not have been able to finish this degree as well. My parents have always been a strong guiding force in my life and I thank them for all their love and support, along with the support of my brother and sister. I also want to thank Kaitlin Farrell who contributed in many ways to this degree in terms of support and intellectual curiosity, along with helping to keep me on track at times. I have grown a lot through my relationship with all of them.

I also want to thank Andrew Davidson and his extended family (the Davidson's, Kroll's and Attwood's) out in Dripping Springs, TX. They were always welcoming to me during my time here. If Andrew had not invited me to visit Austin during our undergrad years I might have never thought to apply to UT Austin. Andrew was also my

introduction to the EWRE (Environmental and Water Resources Engineering) Department here at UT Austin, which is a great community of people. Over the years, I have played a lot of IM sports with them and made many quality friends from that department, way too numerous to include them all here.

Methods Development and Measurements for Understanding Morphological Effects on Electronic and Optical Properties in Solution Processable Photovoltaic Materials

David Paul Ostrowski, Ph. D.

The University of Texas at Austin, 2012

Supervisor: David A. Vanden Bout

The effects of morphology on electronic and optical properties in solution processable photovoltaic (PV) materials have been studied through two different approaches. One approach, scanning photocurrent (PC) and photoluminescence (PL) microscopy, involved mapping PC generation and PL in functional PV devices on the length scale of around 250-500 nm. Additionally, local diode characteristics were studied from regions of interest in the PV through local voltage-dependent photocurrent (LVPC) measurements. In a PV made from a Copper Indium Gallium Selenide (CIGS) nanocrystal (NC) "ink", two morphological features were found to cause the spatial heterogeneity in PC generation. Cadmium Sulfide (CdS) aggregates lowered PC generation by blocking incident light to the photoactive layer, and cracks in the CIGS-NC film enhanced PC generation through improved charge carrier extraction. LVPC measurements showed all regions to have similar diode characteristics with the main difference being the PC generated at zero bias voltage. For another PV made from a donor/acceptor blend of poly(9,9-dioctylfluorene-*co*-*bis*-*N*,*N*-(4-butylphenyl)-*bis*-*N*,*N*-phenyl-1,4-phenylenediamine (PFB) and poly(9,9-dioctylfluorene-*co*-benzothiadiazole)

(F8BT), two incident laser wavelengths were used to selectively illuminate only one or both polymers. The results showed that when F8BT is illuminated, the PFB-rich regions produced the most PC and when both polymers are illuminated (but mostly PFB), the F8BT-rich regions produce the most PC; showing PC generation is more affective when less absorber material is present in the morphology.

The other approach to study morphological effects on PV properties was to fabricate particles that mimicked morphological variations known to occur in solution-processable PVs. Through solution processing of an oligothiophene molecule, a range of weakly coupled H-aggregate particles were made. These particles, identifiable by shape, were shown to have a varying degree of energetic disorder (as gauged by the 0-0 vibronic band intensity in the emission spectrum), despite all particles showing a similarly high degree of molecular order from fluorescence dichroism (FD) measurements. A trend was observed correlating a decrease in energetic disorder with an increase in the local contact potential (LCP) difference as measured with Kelvin probe force microscopy (KPFM). The LCP difference was found to range by 70 mV between particles of moderate to low energetic disorder.

Table of Contents

List of Figures

Chapter 1: Introduction and Dissertation Overview

1.1 Introduction

As the world's energy demand continues to grow there is an increased need for more energy sources, preferably environmentally friendly energy sources. Presently, the main sources of energy are based on fossil fuels of which there is a finite supply. Fossil fuels are also difficult to harvest from the earth and have detrimental effects on the environment. One promising source for environmentally friendly energy production is photovoltaic (PV) technology or solar energy.[1,2] However, the present PV technology remains too expensive for commercial viability and wide spread use.

A potential low cost, mass scalable PV technology is that of solution processable PV materials. This technology focuses on two classes of materials: inorganic nanoparticles[3-7] and semiconducting organic materials.[1,2,8-11] The low cost of these technologies results from the ease of fabrication due to room temperature, solution deposition processing techniques.[12-15] However, the efficiency of this class of PV materials is currently too low for commercially viable, wide spread energy production.[1]

One factor that significantly affects these PVs is heterogeneous morphology and chemical composition variations across the device, both of which have been found to have a significant effect on the local PV performance.[15-18] The heterogeneity results from the solution deposition process. While the particles or molecules are in solution they possess freedom of motion, however, once the solution is deposited onto the substrate and the solvent begins to dry, the freedom of motion gradually decreases until it is lost completely when the solvent is gone. Often the materials will begin to order or phase separate during this post-deposition solvent drying process, but rarely do the materials reach an equilibrium, steady state morphology by the time the solvent has dried. As a

result, the materials end up trapped in a kinetically determined morphology. The result is non-uniform films with much structural and chemical heterogeneity. This is of particular importance in bulk heterojunction (BHJ) donor/acceptor blend PVs. In these devices, charge separation occurs at the interface of the donor and acceptor, but continuous charge transport pathways of both donor and acceptor materials are needed for the respective separated charge carriers to reach the electrodes and produce photocurrent (PC). Thus, the interplay of the morphology and fine scale mixing of donor/acceptor have substantial implications on PV performance.[19] Generally, these devices are spin cast from a blend of donor/acceptor in the same solution, which produces a wide range of complex morphologies, even in a single PV device. Efforts are underway to produce films that will self-assemble into a more uniform equilibrium morphology, however, in order to know the best morphology to target for such systems, a better understanding of the morphological effects on PV performance is needed.[12]

In order for this type of PV technology to move forward, the connection between morphology on PV properties must be understood. However, the effect of these morphological heterogeneities on PV performance are not well characterized through the universally accepted methods of PV characterization, and thus these systems have inspired novel characterization methods to study PVs on a tens of nanometers to micron length scale.

The universal method for characterizing PV performance involves two current-voltage (IV) measurements: one in the dark and one with the entire PV device under illumination. These measurements involve monitoring the current produced in the PV while sweeping the bias voltage applied to the device and allow for determination of short-circuit current (J_{sc}), open circuit voltage (V_{oc}), fill factor (FF), maximum power

point (P_m) and power conversion efficiency (PCE). **Figure 1.1** shows data representative of this type of 'bulk' characterization along with illustrating the terms just described.

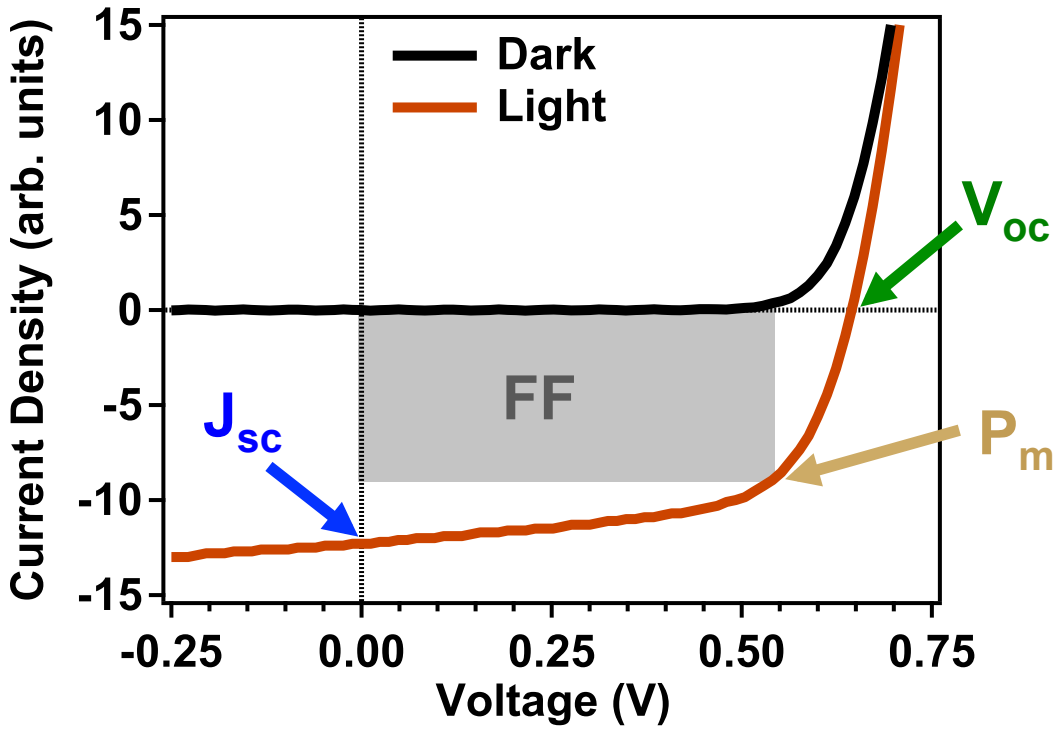

Figure 1.1: Demonstrates the commonly used 'bulk' characterization of a PV device, where current-voltage (IV) measurements are taken with the entire device under dark and illuminated conditions. The graph also illustrates meaningful parameters determined by these measurements: J_{sc}, V_{oc}, P_m and FF.

The J_{sc} is the photocurrent generated at zero applied bias. The V_{oc} is the applied bias when the photocurrent equals zero. P_m is the point of maximum power in the device, where the photocurrent times the applied bias is maximized in the fourth quadrant. FF is the ratio of the P_m to the product of J_{sc} and V_{oc}. PCE is the ratio of the power output of the device compared to the incident light intensity. In another common characterization technique a majority of the device is illuminated with a specific wavelength and the external quantum efficiency (EQE) is measured. Through measuring the power of the incident light and the photocurrent generated at a range of different wavelengths, an EQE spectrum is collected. While these 'bulk' IV measurements provide useful information about the device, they also blend together any effect of local heterogeneity in PV performance. Thus, in order to truly understand this class of PV materials, new characterization techniques are needed that are capable of studying the specific effects of local heterogeneities on PV performance.

As a result of this need, there have been efforts made in recent years to develop instrumentation that allows for characterization of PVs on a morphologically relevant length scale.[16,20-22] These techniques generally involve two methods for localizing the measurement of PV properties. One method is to illuminate a small region of the device and measure the light-induced properties from only that location of the device. The sample is then scanned over this focused light beam while the PC generation at each point is measured, thus creating an image map of local PC generation that highlights any performance heterogeneities in the device. This method is commonly referred to as light beam induced current (LBIC) microscopy[21-29] and is used to study functional PV devices. The other method for measurement localization involves the electrical modes of atomic force microscopy (AFM).[16,20,21,30-41] As AFM operates by measuring tip-sample

interactions, these measurements are localized to the region of the sample directly below the metalized cantilever. The cantilever is then scanned over the sample mapping out the local heterogeneity. Images can be collected in a variety of electrical AFM modes with the sample under dark or illuminated conditions.

1.2 Light Beam Induced Current (LBIC) Microscopy

This technique involves illuminating only a small region of the device at a time and scanning sample over the light beam, creating image maps of light-induced photocurrent (IPC). LBIC measurements have mostly been used on a larger length scale to study fabrication defects and performance quality in silicon-based PVs.[42,43] However, in recent years LBIC has been used to study the complex morphology of solution processable PV materials. For this technique to be on a relevant length scale of the morphological variations in these materials, the incident light beam must be focused to the diffraction limit or beyond through the use of a microscope objective or near-field optics, respectively. In recent years, LBIC has been demonstrated with both scanning confocal microscopy and scanning near-field optical microscopy (SNOM). SNOM-LBIC measurements allowed for simultaneous collection of the photoactive layer topography with IPC.[23-26,43] The technique was demonstrated on various donor/acceptor BHJ PVs composed of organic semiconducting materials, of which the topography provides valuable structural information and is also a marker to correlate regions with morphological information gained from other experiments. This technique requires use of either lateral device geometry[26] or a thin semi-transparent metallic top-electrode in a vertical device architecture.[23-25] The thin electrode allows the light to be transmitted through this typically opaque contact, and for the topography of the photoactive layer to show through. Scanning confocal microscope LBIC measurements have been coupled

with numerous optical spectroscopy methods to simultaneously collect valuable optical information with the IPC map. The optical properties measured have included: fluorescence (FL), photoluminescence (PL), PL spectra and Resonance Raman spectroscopy.[22,26-29] The simultaneous collection of optical properties is a direct means of correlating IPC with variations in chemical composition, aggregation, and the intensity of radiative loss mechanisms across a PV device. This also opens the door for further optical spectroscopy techniques to be coupled with LBIC, such as time-resolved PL, polarized PL and absorption or reflection modes.[44-49] The LBIC technique does involve using much higher laser powers than the typical solar intensity, and also must be done at a particular illumination wavelength rather than using the full solar spectrum. However, LBIC yields valuable information towards understanding performance heterogeneities present in a functional PV device.

1.3 Electronic Modes of Atomic Force Microscopy (AFM)

The other method to localize PV performance measurements is through electronic modes of atomic force microscopy (AFM).[16,21,34,41] These techniques localize the measurement through monitoring the tip-sample interaction directly below a conductive AFM tip, which is then scanned across the sample to map out local performance heterogeneities. The resolution of this technique is dependent on the size of the AFM tip and is on the order of tens of nanometers.[16,35] In some instances, the metal cantilever is used as the top electrode of the device so that the PV is only completed in the region underneath the AFM tip.[21] In other instances, local contact potential (LCP) difference (or surface potential difference) between the tip and sample is measured under both dark and illuminated conditions with Kelvin probe force microscopy (KPFM).[32] The local surface potential has yielded information on work function variations, magnitude and orientation

of interface dipoles, separation of charge carriers, charge distribution and rates.[30,40,50-52] While these techniques measure PV properties on a lower length scale than LBIC, the studies are done on PV relevant materials systems outside of a functional PV device.

In recent years, these techniques have been applied in multiple ways for studying the complex morphology present in solution processable PV devices. The local surface potential under dark and illuminated conditions has been mapped in many donor/acceptor films.[32,34,40,41,53] The LCP map in the dark provides information into variations of the local work function across the sample. These variations typically result from differences in local composition of donor and acceptor material. The change of LCP between the dark and illuminated conditions maps the differences in charge distribution across the film that results from the build up of separated charges in particular regions. Where this LCP change is the highest is where the most PC would be generated in a PV device based on the material system studied, if charge collection variations at the electrode were negligible.

Through KPFM measurements on a sample of scattered particles, each composed of either donor or acceptor, a quantification of the number of charges separated by the donor/acceptor system was demonstrated.[52] This was done by comparing the magnitude of the LCP change, under dark and light conditions, between that of isolated and overlapping donor and acceptor particles.

The LCP measurement has also been extended to measure the local charging rates after illumination. Ginger and coworkers have demonstrated correlation between the external quantum efficiency (EQE) of the device and the rate of photo-induced charging (as measured with time resolved electronic force microscopy, tr-EFM).[30] Thus, through mapping the local photo-induced charging rates, the effects of morphology on EQE are

studied. This technique has been applied to study both morphology and induced oxidative defects in PV material systems.[38]

Another useful AFM mode is conductive AFM (c-AFM), for this the metalized cantilever is scanned in contact with the sample surface, measuring the amount of local current traveling between the AFM tip and the sample at each point in the scan.[20,21,36] The sample for this technique is deposited onto a conductive electrode to allow a bias to be applied between the AFM tip and conductive substrate. Depending on the direction of the bias applied, the contrast in the c-AFM map shows variations in charge transport properties for either electrons or holes.[54] This technique has also been used to measure the local space charge limited current for quantitative determination of local charge mobility.[37]

The c-AFM mode has also been coupled with a light source (either a laser or white light) in order to map out the local PC generated in the device, this is called photocurrent-AFM (pc-AFM).[21,55] This is the same measurement as c-AFM but has the added feature of illuminating the sample beneath the AFM tip. For these measurements the AFM-tip acts as the top electrode of the device, completing the device geometry only in the region of the sample directly below the AFM-tip. Both c-AFM and pc-AFM allow for local current-voltage (IV) measurements in the dark and light, by locating the tip to a region of interest on the sample and sweeping the applied bias. This provides information on variation in the local diode characteristics of the PV materials system.

The last few paragraphs have provided an overview of research being done along similar lines as the work presented in this dissertation. The examples described have demonstrated the value of novel methods of LBIC and electronic modes of AFM in order to better characterize and understand PV performance.[23] In this dissertation both novel characterization methodologies and results from those studies are presented.

1.3 Dissertation Overview

This dissertation presents two approaches to better characterize the local heterogeneity present in solution processable PV technology. One approach couples LBIC with simultaneous photoluminescence (PL) measurements, such as total PL intensity and a local PL spectrum at each point in the PC image map. This approach is referred to as scanning photocurrent (PC) and photoluminescence (PL) microscopy and is capable of resolving features on the order of 250-500 nm with oil immersion and traditional optics, respectively (scanning PC microscopy is also referred to as LBIC microscopy). A valuable extension of this approach is to further study local diode characteristics from regions of interest within the device by measuring the local voltage dependent photocurrent (LVPC). This yields information into variations in diode characteristics with morphology on a functional, as-fabricated device.

Another approach for studying morphological effects on PV properties involves fabrication of unique particles that mimic the local morphological heterogeneities in a typical PV device. Then, studying the electronic and optical properties of specific particles, identifiable by shape. This involved collecting PL emission spectra of individual particles and using the spectral features to gauge the extent of energetic disorder within the particles. These values were then correlated with local contact potential (LCP) differences as measured with Kelvin probe force microscopy (KPFM). A trend of decreasing LCP with and increase in energetic disorder was observed. Through these approaches valuable insight is gained into the effects that morphological heterogeneities have on solution processable PV materials. The techniques are not unique to the systems studied but are applicable to other material systems as well. The information gained from local characterization is essential to truly understand the complex nature of these materials and allow this technology to advance.

CHAPTER 2: MAPPING SPATIAL HETEROGENEITY IN CIGS ($Cu(In_{1-x}Ga_x)Se_2$) NANOCRYSTAL-BASED PHOTOVOLTAICS WITH SCANNING PHOTOCURRENT AND FLUORESCENCE MICROSCOPY

A novel approach of light beam induced current (LBIC) microscopy coupled with fluorescence (FL) microscopy is applied to study the response of as-fabricated, functional PV devices. LBIC microscopy is also referred to as scanning photocurrent (PC) microscopy. Simultaneous collection of fluorescence and PV response enables spatial correlation of the optical and electronic properties with the morphology of the device. Furthermore, local voltage-dependent photocurrent (LVPC) measurements are possible on particular regions of interest of the PV. A demonstration of this technique is presented from studies on a Copper Indium Gallium Selenide (CIGS) nanocrystal (NC) PV device. Significant correlation is made between structural and chemical composition variations with the PV performance of the device. There was an anti-correlation found between PC generation and FL, along with three distinct regions of performance: high, average and low PC. The regions of highest PC correlated to cracks in the CIGS-NC film observed from scanning electron microscopy (SEM). This result is contributed to better charge extraction within these regions due to the increased interfacial area with the electrode and hence lower distances of exciton diffusion needed to reach the electrode. The low PC regions were determined to be a result of aggregate formation within the Cadmium Sulfide (CdS) buffer layer. From atomic force microscopy (AFM) topography and absorbance measurements it was estimated that these aggregates were absorbing greater than 98% of the light before it could reach the photoactive CIGS-NC layer substantially lowering PC generation in these areas. A FL microscopy scan of just the CdS layer on glass also showed similar FL features as the PV device studied. From the shape of the LVPC measurements on the three regions it was observed that there were similar diode characteristics within all three and the only significant change being in the amount of PC

generation, best observed through the PC generated at zero bias. From an area calculation of all three regions it was determined that the power conversion efficiency could be increased by over 50% if the entire device were to function as well as the high PC generating regions. The understanding of morphological effects on PV performance gained from this work offer a guide for device fabrication and are being incorporated by our collaborators in the Korgel Lab at The University of Texas at Austin in order to make more efficient CIGS-NC PV devices, which includes methods for increasing the surface roughness of the back electrode to improve charge carrier extraction, and a method for removing the CdS aggregates before deposition of the top electrode of the PV device.

CHAPTER 3: CORRELATION OF MORPHOLOGY WITH PHOTOCURRENT GENERATION IN A POLYMER BLEND PHOTOVOLTAIC DEVICE

Morphological effects on photovoltaic (PV) properties were studied through scanning photocurrent (PC) and photoluminescence (PL) microscopy of a solution processed, polymer blend PV device composed of PFB [poly(9,9'-dioctylfluorene-*co*-*bis*-*N*,*N*-(4-butylphenyl)-*bis*-*N*,*N*-phenyl-1,4-phenylenediamine] and F8BT [poly(9,9'-dioctylfluorene-*co*-benzothiadiazole]. As PFB and F8BT have unique absorbance bands, it was possible to selectively excite only F8BT (488 nm) or both PFB and F8BT (408 nm). Local voltage-dependent photocurrent (LVPC) measurements from particular regions of interest in the PV showed that the diode characteristics between different morphologies were basically the same, except in regard to the magnitude of PC generated. A local PL spectrum was measured simultaneously with PC generation at each pixel in the image maps. Through integration of the local PL spectrum over particular wavelength ranges, PL image maps were created of PFB-PL (435 to 475 nm), F8BT-PL (530 to 570 nm), exciplex-PL (620 to 685 nm) and total-PL (entire spectrum). These data, along with line scan comparisons and statistical linear correlation tests, allowed direct

correlation of PC generation with local chemical composition variations within the PV device. PL image maps showed morphological variations on the order of 0.5 to 1 microns of alternating PFB-rich and F8BT-rich phases. While illuminating only F8BT (488 nm light), the PFB-rich phases produced the most PC, however, while illuminating both polymers but mostly PFB (408 nm light), the F8BT-rich phases produced the most PC. These results show that in the morphology where the light absorber material is less concentrated, the PC generation is increased. Also, the exciplex-PL is found to not be a significant radiative loss mechanism of charge carriers for PC generation.

CHAPTER 4: THE EFFECTS OF AGGREGATION ON ELECTRONIC AND OPTICAL PROPERTIES OF OLIGOTHIOPHENE PARTICLES

Solution processing of oligothiophene molecules is shown to produce a range of particles with distinct morphologies. Once isolated on a substrate, the optical and electronic properties of individual particles were studied. From polarized scanning confocal microscopy experiments, distinct particles that are identifiable by shape were shown to have similar emission spectra except in regard to the 0-0 vibronic band intensity. This suppression of the 0-0 vibronic band correlates to the amount of energetic disorder present in a weakly coupled H-aggregate. The studied particles ranged from moderate to almost complete suppression of the 0-0 vibronic band when compared to the emission spectrum of the isolated molecule in solution. All particles were found to have a high degree of geometric order (molecular alignment) as observed from the fluorescence dichroism (FD) values of around 0.7-0.8 for all the studied morphologies. The structural and electronic properties of the particles were investigated with Kelvin probe force microscopy (KPFM) to measure the local contact potential (LCP) difference, a quantity that is closely related to the differences in intermolecular charge distribution between the oligothiophene particles. The LCP was found to vary by as much as 70 mV between

different oligothiophene particles and a trend was observed that correlated the LCP changes with the amount of energetic disorder present, as signified by the suppression of the 0-0 vibronic peak in the emission spectra. Combined polarized scanning confocal microscopy studies, along with KPFM measurements, help to provide fundamental insights into the role of morphology, molecular packing, and intermolecular charge distributions in oligiothiophene particles.

CHAPTER 5: FUTURE WORK

Future work would include extensions of the techniques described here. The scanning PC and PL microscopy experimental setup (described in Chapters 2 and 3) could be used to map out a more comprehensive view of the voltage-dependent photocurrent properties. The optical collection could also be extended to measure electroluminescence (EL) and Raman spectra. These measurements would yield information into the variations in voltage at zero PC, local radiative defects and charge transfer (CT) state intensity in the device. The Raman spectroscopy information would give a more quantitative determination of the local chemical composition and order.

The work described in Chapter 4 could be extended to quantify how the effective work function shift observed in the oligothiophene particles affects charge separation at a donor/acceptor heterojunction. This would involve island growth of an acceptor material, such as C_{60}, through thermal deposition on the particle samples. Through KPFM measurements in the dark and light the quantity of charges separated between donor (particle) and acceptor (C_{60}) could be calculated for the different particle morphologies in an experiment similar to the one described in reference 52.

1.4 REFERENCES

1. Brabec, C. J.; Gowrisanker, S.; Halls, J. J. M.; Laird, D.; Jia, S.; Williams, S. P., Polymer–Fullerene Bulk-Heterojunction Solar Cells. *Advanced Materials* **2010**, *22*, 3839-3856.

2. Bredas, J.-L.; Durrant, J. R., Organic Photovoltaics. *Accounts of Chemical Research* **2009**, *42*, 1689-1690.

3. Panthani, M. G.; Akhavan, V.; Goodfellow, B.; Schmidtke, J. P.; Dunn, L.; Dodabalapur, A.; Barbara, P. F.; Korgel, B. A., Synthesis of $CuInS_2$, $CuInSe_2$, and $Cu(In_xGa_{1-X})Se_2$ (CIGS) Nanocrystal "Inks" for Printable Photovoltaics. *J Am Chem Soc* **2008**, *130*, 16770-16777.

4. Hibberd, C. J.; Chassaing, E.; Liu, W.; Mitzi, D. B.; Lincot, D.; Tiwari, A. N., Non-Vacuum Methods for Formation of $Cu(In,Ga)(Se,S)_2$ Thin Film Photovoltaic Absorbers. *Progress in Photovoltaics: Research and Applications* **2010**, *18*, 434-452.

5. Tang, J. A.; Sargent, E. H., Infrared Colloidal Quantum Dots for Photovoltaics: Fundamentals and Recent Progress. *Advanced Materials* **2011**, *23*, 12-29.

6. Kamat, P. V., Quantum Dot Solar Cells. Semiconductor Nanocrystals as Light Harvesters. *Journal of Physical Chemistry C* **2008**, *112*, 18737-18753.

7. Nozik, A. J., Quantum Dot Solar Cells. *Physica E-Low-Dimensional Systems & Nanostructures* **2002**, *14*, 115-120.

8. Brabec, C. J., Organic Photovoltaics: Technology and Market. *Solar Energy Materials and Solar Cells* **2004**, *83*, 273-292.

9. Brabec, C. J.; Durrant, J. R., Solution-Processed Organic Solar Cells. *MRS Bulletin* **2008**, *33*, 670-675.

10. Cai, W. Z.; Gong, X.; Cao, Y., Polymer Solar Cells: Recent Development and Possible Routes for Improvement in the Performance. *Solar Energy Materials and Solar Cells* **2010**, *94*, 114-127.

11. Gunes, S.; Neugebauer, H.; Sariciftci, N. S., Conjugated Polymer-Based Organic Solar Cells. *Chemical Reviews* **2007**, *107*, 1324-1338.

12. Krebs, F. C., Fabrication and Processing of Polymer Solar Cells: A Review of Printing and Coating Techniques. *Solar Energy Materials and Solar Cells* **2009**, *93*, 394-412.

13. Mitzi, D. B.; Yuan, M.; Liu, W.; Kellock, A. J.; Chey, S. J.; Deline, V.; Schrott, A. G., A High-Efficiency Solution-Deposited Thin-Film Photovoltaic Device. *Advanced Materials* **2008**, *20*, 3657-3662.

14. Krebs, F. C.; Tromholt, T.; Jorgensen, M., Upscaling of Polymer Solar Cell Fabrication Using Full Roll-to-Roll Processing. *Nanoscale* **2010**, *2*, 873-886.

15. Yang, X.; Loos, J., Toward High-Performance Polymer Solar Cells: The Importance of Morphology Control. *Macromolecules* **2007**, *40*, 1353-1362.

16. Groves, C.; Reid, O. G.; Ginger, D. S., Heterogeneity in Polymer Solar Cells: Local Morphology and Performance in Organic Photovoltaics Studied with Scanning Probe Microscopy. *Accounts of Chemical Research* **2010**, *43*, 612-620.

17. Lloyd, M. T.; Anthony, J. E.; Malliaras, G. G., Photovoltaics from Soluble Small Molecules. *Materials Today* **2007**, *10*, 34-41.

18. Walker, B.; Kim, C.; Nguyen, T. Q., Small Molecule Solution-Processed Bulk Heterojunction Solar Cells. *Chemistry of Materials* **2011**, *23*, 470-482.

19. Watkins, P. K.; Walker, A. B.; Verschoor, G. L. B., Dynamical Monte Carlo Modelling of Organic Solar Cells: The Dependence of Internal Quantum Efficiency on Morphology. *Nano Letters* **2005**, *5*, 1814-1818.

20. Douheret, O.; Swinnen, A.; Bertho, S.; Haeldermans, I.; D'Haen, J.; D'Olieslaeger, M.; Vanderzande, D.; Manca, J. V., High-Resolution Morphological and Electrical Characterisation of Organic Bulk Heterojunction Solar Cells by Scanning Probe Microscopy. *Progress in Photovoltaics* **2007**, *15*, 713-726.

21. Bull, T. A.; Pingree, L. S. C.; Jenekhe, S. A.; Ginger, D. S.; Luscombe, C. K., The Role of Mesoscopic PCBM Crystallites in Solvent Vapor Annealed Copolymer Solar Cells. *Acs Nano* **2009**, *3*, 627-636.

22. Ostrowski, D. P.; Glaz, M. S.; Goodfellow, B. W.; Akhavan, V. A.; Panthani, M. G.; Korgel, B. A.; Vanden Bout, D. A., Mapping Spatial Heterogeneity in $Cu(In_{1-X}Ga_x)Se_2$ Nanocrystal-Based Photovoltaics with Scanning Photocurrent and Fluorescence Microscopy. *Small* **2010**, *6*, 2832-2836.

23. McNeill, C. R.; Frohne, H.; Holdsworth, J. L.; Dastoor, P. C., Near-Field Scanning Photocurrent Measurements of Polyfluorene Blend Devices: Directly Correlating Morphology with Current Generation. *Nano Letters* **2004**, *4*, 2503-2507.

24. McNeill, C. R.; Frohne, H.; Holdsworth, J. L.; Furst, J. E.; King, B. V.; Dastoor, P. C., Direct Photocurrent Mapping of Organic Solar Cells Using a Near-Field Scanning Optical Microscope. *Nano Letters* **2004**, *4*, 219-223.

25. McNeill, C. R.; Frohne, H.; Holdsworth, J. L.; Dastoor, P. C., Direct Influence of Morphology on Current Generation in Conjugated Polymer:Methanofullerene Solar Cells Measured by Near-Field Scanning Photocurrent Microscopy. *Synthetic Metals* **2004**, *147*, 101-104.

26. Riehn, R.; Stevenson, R.; Richards, D.; Kang, D. J.; Blamire, M.; Downes, A.; Cacialli, F., Local Probing of Photocurrent and Photoluminescence in a Phase-

Separated Conjugated-Polymer Blend by Means of Near-Field Excitation. *Advanced Functional Materials* **2006**, *16*, 469-476.

27. Gao, Y. Q.; Martin, T. P.; Thomas, A. K.; Grey, J. K., Resonance-Raman Spectroscopic and Photocurrent Imaging of Polythiophene/Fullerene Solar Cells. *Journal of Physical Chemistry Letters* **2010**, *1*, 178-182.

28. Gao, Y. Q.; Martin, T. P.; Niles, E. T.; Wise, A. J.; Thomas, A. K.; Grey, J. K., Understanding Morphology-Dependent Polymer Aggregation Properties and Photocurrent Generation in Polythiophene/Fullerene Solar Cells of Variable Compositions. *Journal of Physical Chemistry C* **2010**, *114*, 15121-15128.

29. Brenner, T. J. K.; McNeill, C. R., Spatially Resolved Spectroscopic Mapping of Photocurrent and Photoluminescence in Polymer Blend Photovoltaic Devices. *Journal of Physical Chemistry C* **2011**, *115*, 19364-19370.

30. Coffey, D. C.; Ginger, D. S., Time-Resolved Electrostatic Force Microscopy of Polymer Solar Cells. *Nature Materials* **2006**, *5*, 735-740.

31. Coffey, D. C.; Reid, O. G.; Rodovsky, D. B.; Bartholomew, G. P.; Ginger, D. S., Mapping Local Photocurrents in Polymer/Fullerene Solar Cells with Photoconductive Atomic Force Microscopy. *Nano Letters* **2007**, *7*, 738-744.

32. Hoppe, H.; Glatzel, T.; Niggemann, M.; Hinsch, A.; Lux-Steiner, M. C.; Sariciftci, N. S., Kelvin Probe Force Microscopy Study on Conjugated Polymer/Fullerene Bulk Heterojunction Organic Solar Cells. *Nano Letters* **2005**, *5*, 269-274.

33. Milner, R. G.; Arias, A. C.; Stevenson, R.; Mackenzie, J. D.; Richards, D.; Friend, R. H.; Kang, D. J.; Blamire, M., Phase Separation in Polyfluorene Blends Investigated with Complementary Scanning Probe Microscopies. *Materials Science and Technology-London* **2002**, *18*, 759-762.

34. Palermo, V.; Otten, M. B. J.; Liscio, A.; Schwartz, E.; de Witte, P. A. J.; Castriciano, M. A.; Wienk, M. M.; Nolde, F.; De Luca, G.; Cornelissen, J. J. L. M.; Janssen, R. A. J.; Müllen, K.; Rowan, A. E.; Nolte, R. J. M.; Samori, P., The Relationship between Nanoscale Architecture and Function in Photovoltaic Multichromophoric Arrays as Visualized by Kelvin Probe Force Microscopy. *Journal of the American Chemical Society* **2008**, *130*, 14605-14614.

35. Palermo, V.; Palma, M.; Samori, P., Electronic Characterization of Organic Thin Films by Kelvin Probe Force Microscopy. *Advanced Materials* **2006**, *18*, 145-164.

36. Pingree, L. S. C.; Reid, O. G.; Ginger, D. S., Electrical Scanning Probe Microscopy on Active Organic Electronic Devices. *Advanced Materials* **2009**, *21*, 19-28.

37. Reid, O. G.; Munechika, K.; Ginger, D. S., Space Charge Limited Current Measurements on Conjugated Polymer Films Using Conductive Atomic Force Microscopy. *Nano Letters* **2008**, *8*, 1602-1609.

38. Reid, O. G.; Rayermann, G. E.; Coffey, D. C.; Ginger, D. S., Imaging Local Trap Formation in Conjugated Polymer Solar Cells: A Comparison of Time-Resolved Electrostatic Force Microscopy and Scanning Kelvin Probe Imaging†. *The Journal of Physical Chemistry C* **2010**, *114*, 20672-20677.

39. Romero, M. J.; Morfa, A. J.; Reilly, T. H., III; van de Lagemaat, J.; Al-Jassim, M., Nanoscale Imaging of Exciton Transport in Organic Photovoltaic Semiconductors by Tip-Enhanced Tunneling Luminescence. *Nano Letters* **2009**, *9*, 3904-3908.

40. Shikler, R.; Chiesa, M.; Friend, R. H., Photovoltaic Performance and Morphology of Polyfluorene Blends: The Influence of Phase Separation Evolution. *Macromolecules* **2006**, *39*, 5393-5399.

41. Palermo, V.; Liscio, A.; Palma, M.; Surin, M.; Lazzaroni, R.; Samori, P., Exploring Nanoscale Electrical and Electronic Properties of Organic and Polymeric Functional Materials by Atomic Force Microscopy Based Approaches. *Chemical Communications*. **2007**, 3326-3337.

42. Thantsha, N. M.; Macabebe, E. Q. B.; Vorster, F. J.; van Dyk, E. E., Opto-Electronic Analysis of Silicon Solar Cells by Lbic Investigations and Current-Voltage Characterization. *Physica B-Condensed Matter* **2009**, *404*, 4445-4448.

43. Acciarri, M.; Binetti, S.; Racz, A.; Pizzini, S.; Agostinelli, G., Fast LBIC in-Line Characterization for Process Quality Control in the Photovoltaic Industry. *Solar Energy Materials and Solar Cells* **2002**, *72*, 417-424.

44. Cadby, A.; Khalil, G.; Fox, A. M.; Lidzey, D. G., Mapping Exciton Quenching in Photovoltaic-Applicable Polymer Blends Using Time-Resolved Scanning near-Field Optical Microscopy. *Journal of Applied Physics* **2008**, *103*, 093715.

45. Cadby, A. J.; Dean, R.; Elliott, C.; Jones, R. A. L.; Fox, A. M.; Lidzey, D. G., Imaging the Fluorescence Decay Lifetime of a Conjugated-Polymer Blend by Using a Scanning near-Field Optical Microscope. *Advanced Materials* **2007**, *19*, 107-111.

46. Kwak, E. S.; Kang, T. J.; Bout, D. A. V., Fluorescence Lifetime Imaging with Near-Field Scanning Optical Microscopy. *Analytical Chemistry* **2001**, *73*, 3257-3262.

47. Kwak, E. S.; Kang, T. J.; Teetsov, J.; Vanden Bout, D. A., Fluorescence Lifetime Imaging of Organic Thin Films in Near-Field Scanning Optical Microscopy. *Abstracts of Papers of the American Chemical Society* **2000**, *220*, U89-U89.

48. Teetsov, J.; Vanden Bout, D. A., Near-Field Scanning Optical Microscopy Studies of Nanoscale Order in Thermally Annealed Films of Poly(9,9-diakylfluorene). *Langmuir* **2002**, *18*, 897-903.

49. Teetsov, J.; Vanden Bout, D. A., Near-Field Scanning Optical Microscopy (NSOM) Studies of Nanoscale Polymer Ordering in Pristine Films of Poly(9,9-dialkylfluorene). *Journal of Physical Chemistry B* **2000**, *104*, 9378-9387.

50. Sugimura, H.; Hayashi, K.; Saito, N.; Nakagiri, N.; Takai, O., Surface Potential Microscopy for Organized Molecular Systems. *Applied Surface Science* **2002**, *188*, 403-410.

51. Maldonado, S.; Smith, T. J.; Williams, R. D.; Morin, S.; Barton, E.; Stevenson, K. J., Surface Modification of Indium Tin Oxide Via Electrochemical Reduction of Aryldiazonium Cations. *Langmuir* **2006**, *22*, 2884-2891.

52. Liscio, A.; De Luca, G.; Nolde, F.; Palermo, V.; Müllen, K.; Samori, P., Photovoltaic Charge Generation Visualized at the Nanoscale: A Proof of Principle. *Journal of the American Chemical Society* **2007**, *130*, 780-781.

53. Chiesa, M.; Burgi, L.; Kim, J. S.; Shikler, R.; Friend, R. H.; Sirringhaus, H., Correlation between Surface Photovoltage and Blend Morphology in Polyfluorene-Based Photodiodes. *Nano Letters* **2005**, *5*, 559-563.

54. Dante, M.; Peet, J.; Nguyen, T. Q., Nanoscale Charge Transport and Internal Structure of Bulk Heterojunction Conjugated Polymer/Fullerene Solar Cells by Scanning Probe Microscopy. *Journal of Physical Chemistry C* **2008**, *112*, 7241-7249.

55. Dang, X. D.; Tamayo, A. B.; Seo, J.; Hoven, C. V.; Walker, B.; Nguyen, T. Q., Nanostructure and Optoelectronic Characterization of Small Molecule Bulk Heterojunction Solar Cells by Photoconductive Atomic Force Microscopy. *Advanced Functional Materials* **2010**, *20*, 3314-3321.

Chapter 2: Mapping Spatial Heterogeneity in CIGS ($Cu(In_{1-x}Ga_x)Se_2$) Nanocrystal-Based Photovoltaics with Scanning Photocurrent and Fluorescence Microscopy

This chapter was reproduced in part from: Ostrowski, D. P.; Glaz, M. S.; Goodfellow, B. W.; Akhavan, V. A.; Panthani, M. G.; Korgel, B. A.; Vanden Bout, D. A., Mapping Spatial Heterogeneity in $Cu(In_{1-X}Ga_x)Se_2$ Nanocrystal-Based Photovoltaics with Scanning Photocurrent and Fluorescence Microscopy. *Small* **2010**, *6*, 2832-2836.

2.1 INTRODUCTION

The widespread use of photovoltaic (PV) devices to harvest energy from the sun requires significant reduction in the cost of solar cell technology.[1,2] One approach to lowering manufacturing cost is to use solution-processable materials that can be printed onto various substrates, including plastics, under ambient conditions with high throughput techniques like roll-to-roll printing.[3,4] While many soluble photovoltaic materials have been developed in recent years, the efficiency of these devices is still too low for commercial viability.[5–7] In order to improve efficiency, a more detailed understanding of PV performance is needed. One factor that can limit the performance of thin film PVs is structural, chemical, and electronic heterogeneity in the device.[3,8–16] These variations can occur on the sub-micrometer length scale, thus requiring microscopic techniques that can examine functioning devices with sufficient resolution to observe these kinds of effects. Here, we present a microscopy technique, capable of studying as-fabricated PV devices, that allows local PV performance to be measured with sub-micron resolution and correlated with the optical properties of the materials. The technique is used here to examine PV devices fabricated with $Cu(In_{1-x}Ga_x)Se_2$ (CIGS) nanocrystal "inks."

Numerous microscopy techniques have been developed to study local variations in PV performance. Scanning probe techniques, such as conductive probe atomic force microscopy (AFM) and Kelvin force microscopy (KFM), have been used to relate morphology to local variations in properties, including photoresponse and surface potential.[9,17–25] Since these tools operate by monitoring tip-sample interaction, the measurements are localized to the region of the sample directly below the metalized cantilever. These techniques cannot be applied to as-fabricated PV devices, and are instead useful for measuring the electrical properties of model thin films. One way to probe the local photovoltaic response of a device is to only illuminate a small region of the device with a microscopically focused beam of light. Only the light-induced electrical properties of the illuminated region contribute to the measured performance; this technique can map the induced photocurrent and is known as light beam induced current microscopy (LBIC).[24,26–31] The spatial resolution depends on the size of the illumination spot, which through focusing the incident light via a microscope objective can reach the diffraction limit and beyond with near-field techniques. By raster-scanning the device across the focused light spot, a map of local PV response can be generated, highlighting spatial heterogeneities in photocurrent generation across the device.

LBIC measurements have been used to test for fabrication defects and performance quality in silicon-based PVs,[27,32] and to study heterogeneity in organic bulk heterojunction PVs.[24,28–31,33] Most of these studies have utilized conventional microscopy; a few studies achieved higher spatial resolution on the order of 200 nm by utilizing near-field scanning optical microscopy.[28–30,33]

Here we report a novel approach of LBIC microscopy coupled with fluorescence microscopy that we apply to study the response of as-fabricated, functional PV devices. As this technique illuminates the PV through the transparent electrode, there is no need

for constructing planar devices[33] or ones with a thin, semi-transparent metal electrode.[28–30] Simultaneous collection of fluorescence and PV response enables spatial correlation of the optical and electronic properties with the morphology of the device. It should also be possible to couple other optical microscopy techniques with the LBIC method, such as time-resolved fluorescence, polarized fluorescence, and absorption or reflection modes, which can yield valuable information into specific PV characteristics such as charge separation, molecular orientation, local crystallinity and absorption.[12,14–16,31] For example, LBIC coupled with Resonance Raman spectroscopy has recently been demonstrated.[31] In addition to imaging, the technique presented here is capable of collecting local voltage-dependent photocurrent data. Here, the technique is applied to a solution processed CIGS nanocrystal-based PV device.

2.2 Experimental Methods

Synthesis of CIGS nanocrystal ink: $Cu(In_{1-x}Ga_x)Se_2$ (x = 0.25 targeted) nanocrystals were synthesized by arrested precipitation using standard Schlenk line techniques as previously reported.[34] The washed and purified CIGS NPs were dispersed in toluene at a concentration of 20 mg/mL to make the 'ink' used in device fabrication.

CIGS nanocrystal-based PV device fabrication: Polished float glass substrates with dimensions 25 x 25 x 1.1 mm (Delta Technologies, Ltd.) were cleaned by sonication in a 50/50 mixture of acetone and isopropanol followed by sonication in deionized water. Each sonication lasted 5 min and was followed by drying in a nitrogen stream. The glass substrates were then exposed to a 100 W oxygen plasma for 5 min to remove any organic residue on the surface. After cleaning, 5 nm of chromium and 60 nm of gold were thermally evaporated to form the metal back contact of the devices. A 600 nm CIGS nanocrystal absorber layer was then deposited by spray coating from an ink (described

above) using a commercially available airbrush (iwata Eclipse HP-CS) operated at 50 psig of head pressure. A CdS buffer layer was deposited by a modified chemical bath deposition following procedures outlined by McCandless and Shafarman.[37] The device was placed on a hotplate at 90 °C for 5 min after which an aqueous solution of 3 mM cadmium sulfate ($CdSO_4$, Aldrich, 99.999%), 0.53 M thiourea (Fluka, 99.999%), and 8.1 M ammonium hydroxide (NH_3, Fisher, ACS certified) was deposited onto the device which was then covered with a glass petri dish to prevent evaporation. After 2 min, the device was removed from the hotplate and rinsed with deionized water and then left flat to dry. Next a window layer consisting of i-ZnO and ITO were deposited by RF sputtering. A 50 nm layer of ZnO (target 99.9%, Lesker) was first sputtered in an atmosphere of 0.5% O_2 in Ar (99.95%, Praxair) with a 150 W plasma. This was followed by a 300 nm layer of ITO (target 99.99% In_2O_3: SnO_2 90:10, Lesker) sputtered in an Ar atmosphere (research grade, Praxair) with a 180 W plasma. The final active area of the device was 8 mm^2 (a 4 x 2 mm rectangle). A small dab of conductive silver paint (SPI supplies) was placed on all contact pads to improve contact with the testing apparatus.

'Bulk' photovoltaic characterization: Conventional current-voltage response was with a Keithley 2400 General Purpose Sourcemeter using a Xenon Lamp Solar Simulator (Newport) equipped with an AM1.5 filter as an illumination source. External Quantum Efficiency (EQE) spectra were gathered using a chopper (Stanford Research Systems, model SR540), a lock-in amplifier (Stanford Research Systems, model SR830), a monochromator (Newport Cornerstone 260 1/4M), and a Si photodiode calibrated by the manufacturer (Hamamatsu).

Morphological and Spectral characterization: Scanning electron microscopy (SEM) images were acquired using a Zeiss Supra 40 VP SEM operating at 10 keV accelerating voltages and using an in-lens detector. Atomic force microcopy (AFM)

images were acquired using a Digital Instruments multimode AFM (model MMAFM-2). Ultraviolet-visible (UV-VIS) spectra were collected using an Agilent 8453 UV-VIS.

Photocurrent and Fluorescence image maps were obtained using a Coherent 408 nm diode laser as the excitation light source, which was focused through a 50x Olympus objective. The size of the focal spot was ~ 275 nm in diameter as determined by scanning across a step edge in a patterned metal film. The typical incident laser power was 1.5 μW, which yields a power density of ~ 2.53 kW/cm^2 after the light is focused through the objective. For sample scanning capabilities a Physik Instrumente (PI) piezoelectric stage (model E-501.00) was mounted onto a Nikon Diaphot 300 inverted microscope. The excitation beam was chopped at 174 Hz using a Digirad chopper (model C-980) and the photocurrent of the device was amplified 10^4 times using a transimpedance amplifier built in house. The fluorescence was collected using a Perkin Elmer APD (model SPCM-CD290) and the amplified current was collected using an EG&G DSP lock-in amplifier (model 7220). The LVPC curves were obtained by sweeping the applied voltage across the device, sourced from a serial digital to analog (D/A) converter built onto the circuit board of the pre-amplifier, and recording the output signal from the lock-in with a Keithley 2400 General Purpose Sourcemeter. The serial D/A was controlled with LabVIEW.

2.3 Results and Discussion

Figure 2.1A shows the structure of the CIGS nanocrystal PV device that was studied. The device consists of a light-absorbing layer of CIGS nanocrystals deposited on a gold back-contact. Cadmium sulfide (CdS) is added as a buffer layer on top of the nanocrystal layer by chemical bath deposition, followed by a 50 nm thick zinc oxide (ZnO) window layer and 300 nm of indium tin oxide (ITO) deposited by RF sputtering.

Figure 2.1B shows the device response in the dark and under AM1.5 illumination. The short-circuit current density (J_{sc}), open-circuit voltage (V_{oc}), fill factor (FF), and power conversion efficiency (PCE) were 3.5 mA cm^{-2}, 0.38 V, 0.41, and 0.51%, respectively. **Figure 2.1C** shows the wavelength-dependent external quantum efficiency (EQE) measured for the same device. The EQE is a measure of zero-bias current generated per incident photon on the device. The excitation source for the LBIC measurements had a wavelength of 408 nm, on the high energy edge of the EQE spectrum. The shape of the EQE curve is a result of the optical characteristics of both the CIGS nanocrystal absorber layer and the ZnO/ITO window layer.[34]

Figure 2.2 shows a schematic of the LBIC microscopy setup. The sample is illuminated with 408 nm laser-light focused to a 275 nm diameter spot size. The photogenerated current is measured, along with fluorescence from the sample. As the sample is raster-scanned across the illumination spot, measurements are collected at each step to generate an image map of the measured, local properties.

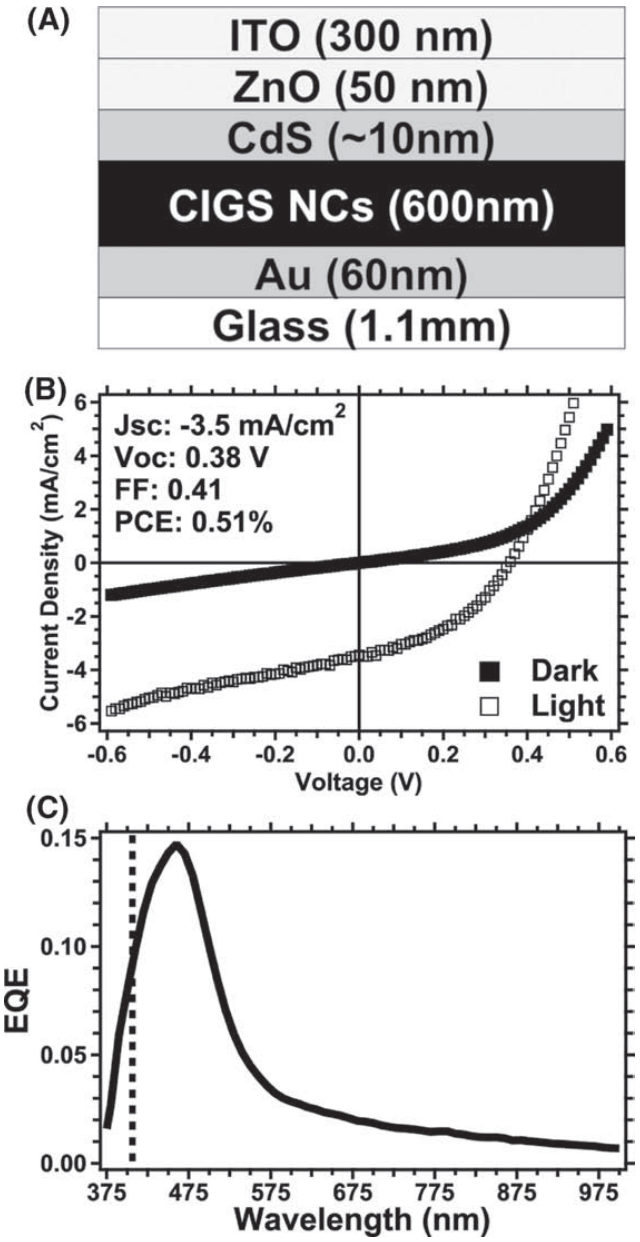

Figure 2.1: (**A**) Schematic of a CIGS nanocrystal (NC) based PV device. (**B**) J-V measurements performed under dark and AM1.5 illumination conditions. (**C**) External Quantum Efficiency (EQE) measured as a function of wavelength (vertical dotted line marks the laser excitation wavelength used for LBIC, 408 nm).

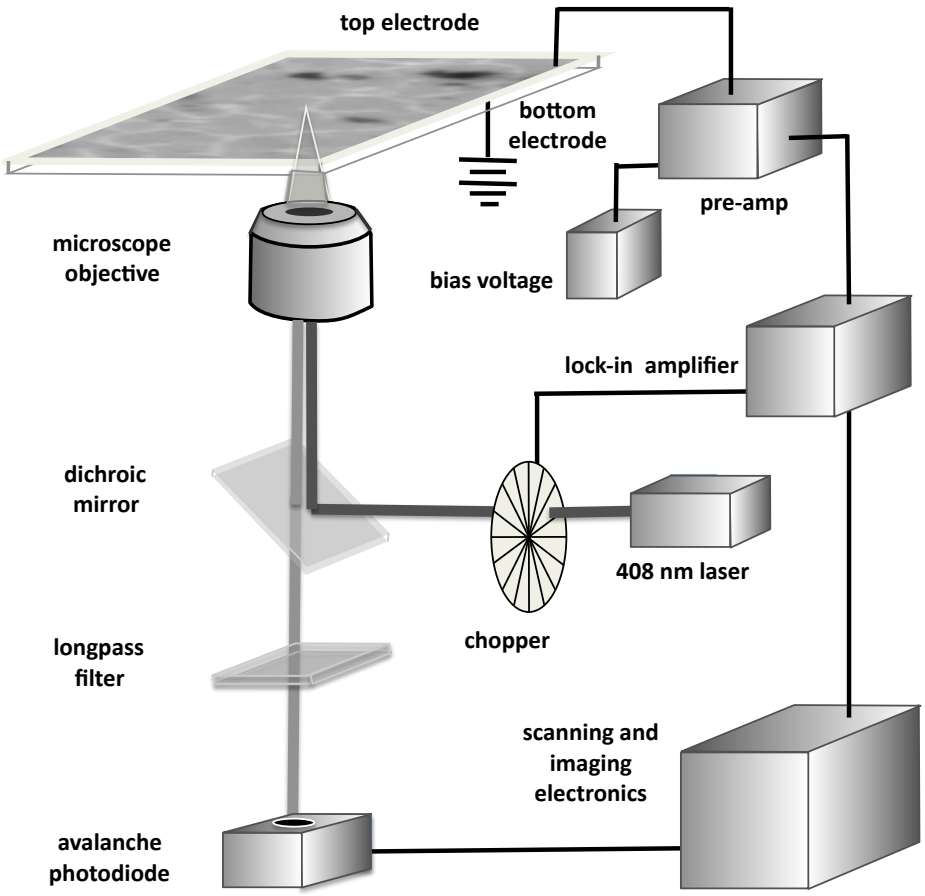

Figure 2.2: Schematic of the scanning Light Beam Induced Current (LBIC) and fluorescence microscopy experimental setup.

One challenge of mapping the photocurrent is that the entire device is active but only a microscopic region is being illuminated. The induced photocurrent (IPC) signals from the focused laser spot are on the order of 1 and 40 nA. However, these signals are on top of a comparatively large background from the dark current of the full device, which also varies non-linearly with applied bias voltage. As such, current amplification and lock-in detection were necessary to obtain sufficient signal to noise. Signal amplification was accomplished with a transimpedance amplifier (or current to voltage converter) built in-house with a gain of 10,000x. The incident light beam is chopped and output signal of the device is measured with a lock-in amplifier. Therefore, the IPC that is measured represents the difference between the current measured during illumination and the dark current.

An LBIC image map of a CIGS nanocrystal based PV is shown in **Figure 2.3A**. There is significant heterogeneity in device response, with micrometer-scale regions of both increased and decreased IPC generation compared to the average response of the device. The higher performance regions appear filamentary (Region B), while the lowest performance regions have a circular shape with typical diameters of 1-2 microns (Region C). These regions of high and low response are scattered throughout relatively homogeneous regions with average device response (Region A). From the image it is observed that regions A, B and C correspond to 75%, 20% and 5% of the device, respectively (see supporting information). **Figure 2.3B** shows the fluorescence microscopy image that was acquired simultaneously with the LBIC measurement. It is clear that the local variations in IPC have corresponding variations in fluorescence.

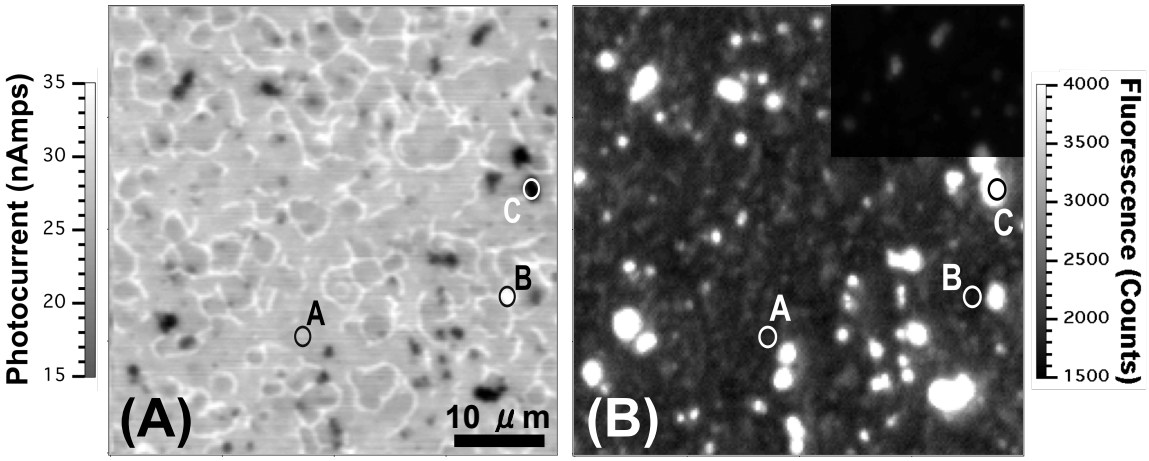

Figure 2.3: Image maps of (**A**) zero-bias induced photocurrent (IPC) and (**B**) fluorescence intensity for a CdS-capped CIGS nanocrystal PV device. Overlay in upper right corner of (B): that area of the fluorescence image shown at a different, non-saturated contrast scale of 1,500 to 27,000 counts.

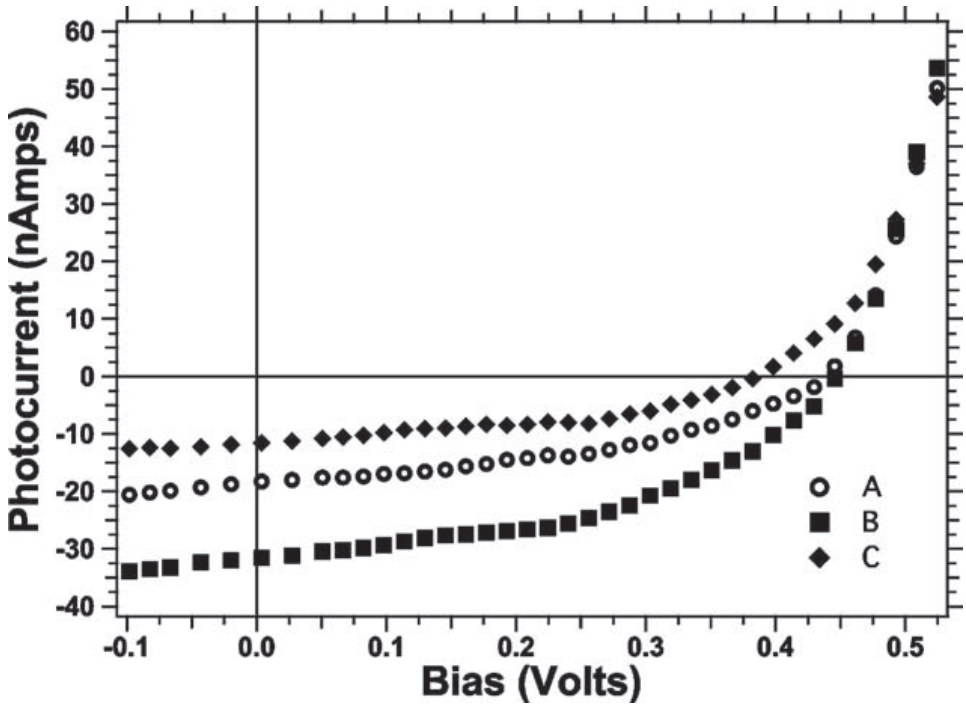

Figure 2.4: Local voltage-dependent photocurrent (LVPC) measured with the focused light beam positioned at locations A, B and C labeled on the images shown in Figure 2.3. These LVPC measurements are representative of the response from regions of the device with average, high and low IPC.

The fluorescence intensity, which relates to the local chemical composition and the extent of radiative charge recombination, is inversely correlated with the IPC signal in the image. For instance, areas of the device like Region C have high fluorescence intensity with low IPC, and areas like Region B show lower fluorescence and exhibit higher IPC (see also supporting information). This is consistent with what one would expect: regions with higher fluorescence have higher radiative recombination and fewer charge carriers available for extraction as IPC.

This technique provides another useful feature: after an image map is collected, the beam can be repositioned to illuminate a selected region of the sample to measure the local voltage-dependent photocurrent (LVPC). **Figure 2.4** shows the local photocurrent traces obtained at points labeled A, B, and C in Figure 2.3; the traces are representative of the three distinct types of regions found across the device. The main difference between regions is the magnitude of the photocurrent at zero bias. The general shape of the LVPC curve is similar for the three different regions. There is a slight decrease of ~0.06 V for region C in the bias at which the LVPC is zero, however, the decrease is close to the error in the voltage measurement of ±0.05 V. This difference may result from lower charge carrier densities in these regions as they have an associated high fluorescence intensity, which is shown to be from CdS (see further discussion below).

It is important to note the LVPC is not the same as the conventional I-V response measured with the device exposed to light. As a result of the lock-in detection, the measured current reflects only the additional current induced by the local illumination since the dark current has been subtracted from the signal. This means that the bias at which the LVPC is zero (induced photocurrent equals zero) is not the same as the V_{oc} (total current equals zero). As a result, a local power conversion efficiency cannot be

calculated. However, relative efficiencies can be estimated since the only significant difference between the LVPC response of the different regions is the current at zero bias.

From the data in Figure 2.4, the LVPC at zero bias in regions A, B and C are 18.3, 31.6 and 11.6 nA, respectively, with an error of ±1.5 nA. Thus, the regions of higher photocurrent are nearly a factor of two greater than the average, while the regions of low response are over one-third decreased from the average. It is interesting to consider that if the device were composed entirely of the regions of greatest photocurrent (region B), there would be more than 50% enhancement in the power conversion efficiency of the device. While this would still be far below other reported CIGS device efficiencies,[35] these results identify specific pathways for substantially improving the performance of this emerging, solution-deposited photovoltaic system.

The high IPC regions in the device, Regions B, have a filamentary morphology. As shown in **Figure 2.5A**, cracks in the nanocrystal films observed by SEM have a similar morphology. Therefore, it appears that these cracked regions are giving rise to the observed increased photocurrent in the device. Higher IPC is most likely due to the fact that the nanocrystal film is thinner in this region and therefore, more of the photogenerated carriers can be extracted from the layer before being eliminated by recombination. Increased photocurrent could also stem from increased interfacial contact area between the CdS layer and CIGS nanocrystal film, as a result of CdS penetrating into the cracks. This type of structure would also require shorter distances for minority charge carriers to travel to reach the interface. These regions also have lower fluorescence (see Figure 2.3 and supporting information), indicating that there is less radiative charge recombination.

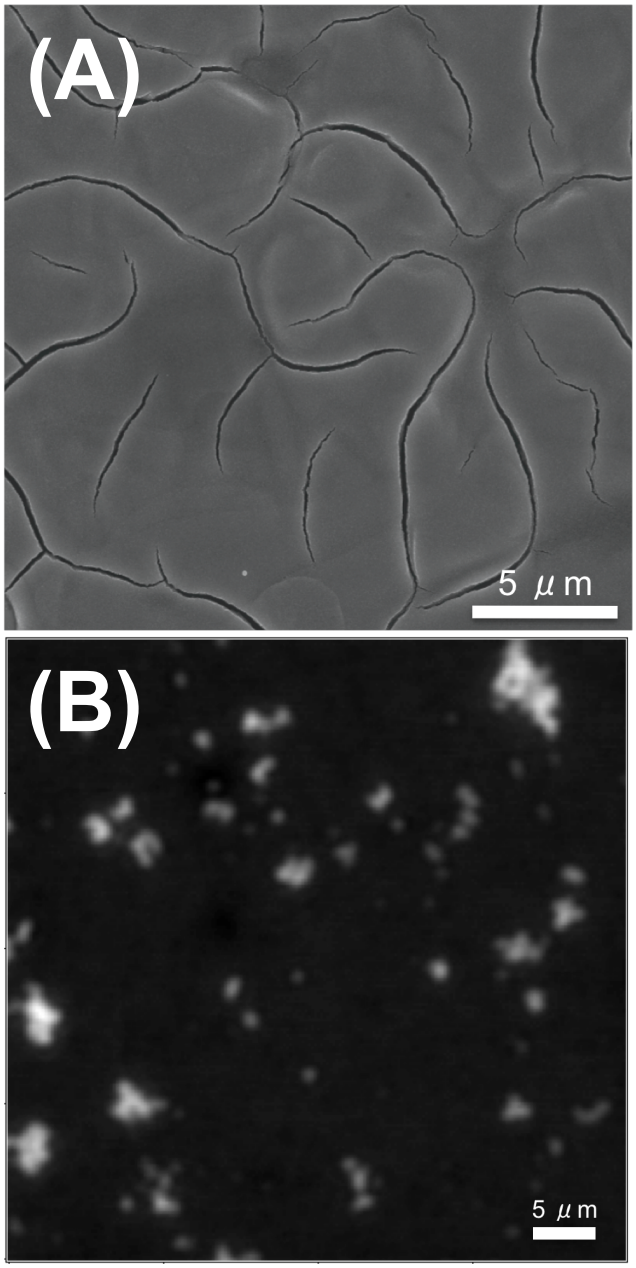

Figure 2.5: (**A**) Scanning electron microscope image of the CIGS nanocrystal layer of the device. (**B**) Fluorescence image of a CdS layer deposited on glass, intensity scale is 10,000 to 50,000 counts.

AFM images of the CdS buffer layer showed that occasionally large aggregates form in the thin film as a result of homogeneous nucleation in the deposited solution (see supporting information). To investigate if Region C areas corresponded to CdS aggregates, fluorescence image maps were separately collected from each layer of the device on glass: ZnO/ITO, CdS, CIGS nanocrystal and blank glass. While the fluorescence image of the CdS showed highly fluorescent features, **Figure 2.5B**, none of the other layers showed fluorescence contrast. The similarity between the fluorescence images of the CdS films (Figure 2.5B) and the fluorescence from the device (Figure 2.3B) confirms that Regions C correspond to places in the device in which the CdS aggregates are present. As the illumination must pass through the CdS layer before reaching the photoactive layer, one possibility for the lower response of these regions is that the aggregate may absorb most of the incident light, limiting transmission to the photoactive CIGS nanocrystal layer. The thickness of the CdS aggregates was assessed with a height analysis of the AFM topography images and the aggregates were found to range from 250 nm to greater than 1000 nm in height. The transmission of the aggregates was estimated to be at most 1.7% for the 250 nm aggregates and even as low as 10^{-4}% transmission for aggregates at 1000 nm.[36] Thus, when the aggregates are present, essentially no light is reaching the photoactive CIGS nanocrystal layer and one may expect the IPC in these regions to drop to zero. However, the IPC in these regions fall by at most half the IPC from that of Region A (average IPC). This could be a result of fluorescence from or incident light scattered off of the aggregates being reabsorbed by the CIGS nanocrystal layer and leading to IPC. Alternatively, light absorbed by the CdS layer may also generate current, albeit not as efficiently as the CIGS nanocrystal layer.

2.4 CONCLUSION

In summary, microscopic imaging of a CIGS nanocrystal-based PV device has revealed substantial spatial heterogeneity in the photoresponse. Distinct regions of both higher and lower photocurrent could be observed on a variety of length scales ranging from hundreds of nanometers to tens of microns. Two morphological features were found to cause the heterogeneity: CdS aggregates that lowered IPC and cracks in the CIGS nanocrystal absorber layer that produced higher IPC. The performance differences between regions could be quantified using LVPC measurements and show the cracked regions to have had a zero bias photocurrent that was nearly double that of an average region. This information along with the photocurrent maps allow for an estimation of efficiency from a theoretical device composed entirely of the high IPC regions; such a device would have an increase of more than 50% in power conversion efficiency compared to the device studied. Efforts are currently underway to leverage this information to design new fabrication techniques that will improve the device efficiency of CIGS nanocrystal PVs. The coupling of microscopy, spectroscopy and electrical characterization presented here is applicable not only to these systems but any PV device. As such, direct measurements of how morphology affects performance can be used to guide device design and fabrication in the development of future high efficiency PVs.

2.5 SUPPORTING INFORMATION

Figure 2.6 shows the Beer's law plot used to estimate the absorbance of the CdS aggregates along with topographical AFM data used to determine the aggregate thicknesses. It is apparent that the aggregates range from 250 nm to greater than 1000 nm, with transmission estimated at 1.7% and 10^{-4}%, respectively.

Figure 2.7 demonstrates that the CdS aggregates formed when deposited on a CIGS nanocrystal film are of similar size range as when CdS layer is deposited on glass (Figure 2.6). The roughness of the CIGS nanocrystal film makes it difficult to precisely tell the height of the CdS aggregates, however, they appear to be on the order of 500 nm. This height is within the height range (250 to 1000 nm) of the more precisely measured CdS aggregates on glass.

Figure 2.8 shows that the CdS aggregates are scattered over the CIGS nanocrystal film and rarely correlate with a crack in the CIGS nanocrystal film, which shows the CdS aggregates are not nucleating at defects in the underlying film but rather result from homogeneous nucleation in solution. This theory is further supported from the spherical morphology of the aggregates.

Figure 2.9 shows that the areas of high IPC (Region B) correspond to lower fluorescence, which means there is less extent of radiative charge recombination in those areas of the device. The opposite is true for the CdS aggregates of Region C that show increased radiative charge recombination and decreased IPC.

Figure 2.10 shows the threshold levels used to determine the percentages of the IPC image that correlate to high and low photocurrents, Regions B and C respectively. The high photocurrent threshold (B) and low photocurrent threshold (C) included 20% and 5% respectively of the image area.

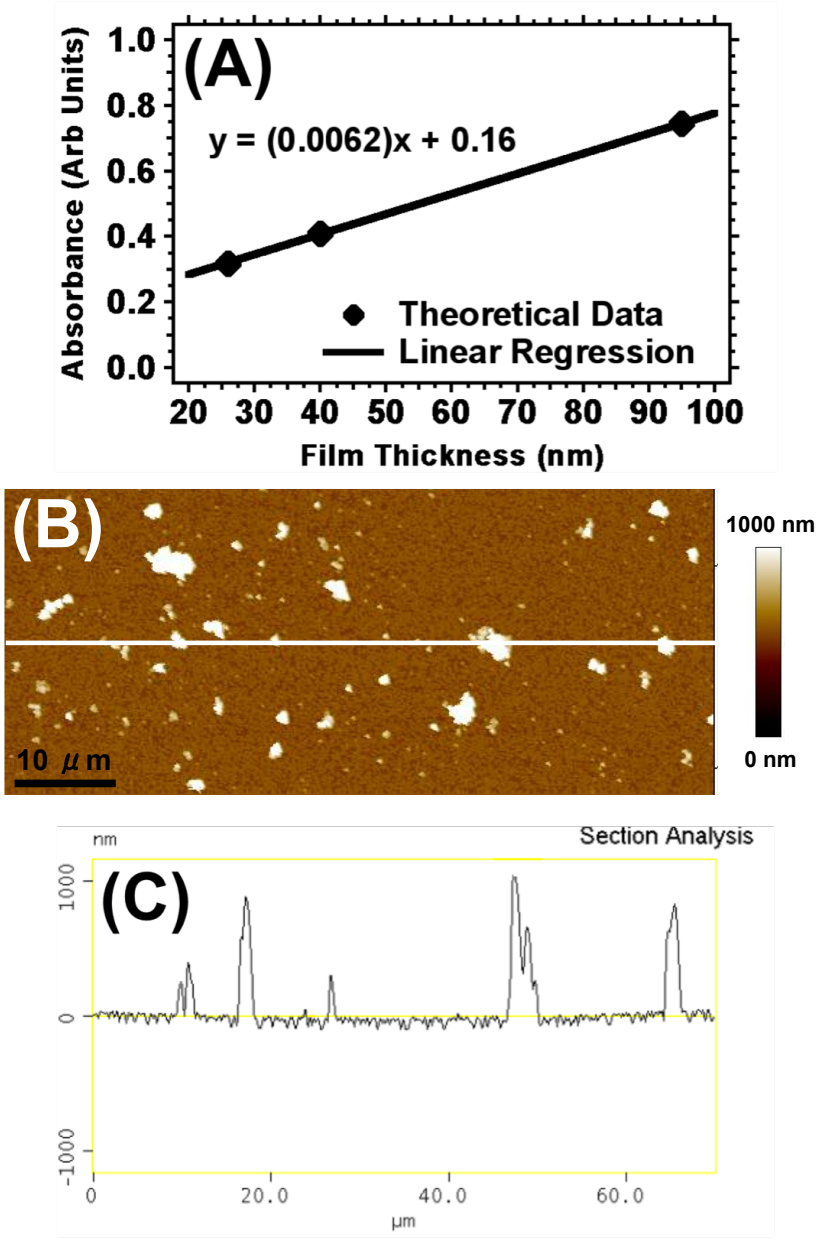

Figure 2.6: **(A)** Beer's Law plot of CdS absorbance at 408 nm wavelength light, constructed from theoretically calculated data from Derkaoui and co-workers.[36] **(B)** Topographic AFM image of CdS layer deposited on a glass substrate. **(C)** Line scan (section analysis) of the AFM topography taken along the white line in (B).

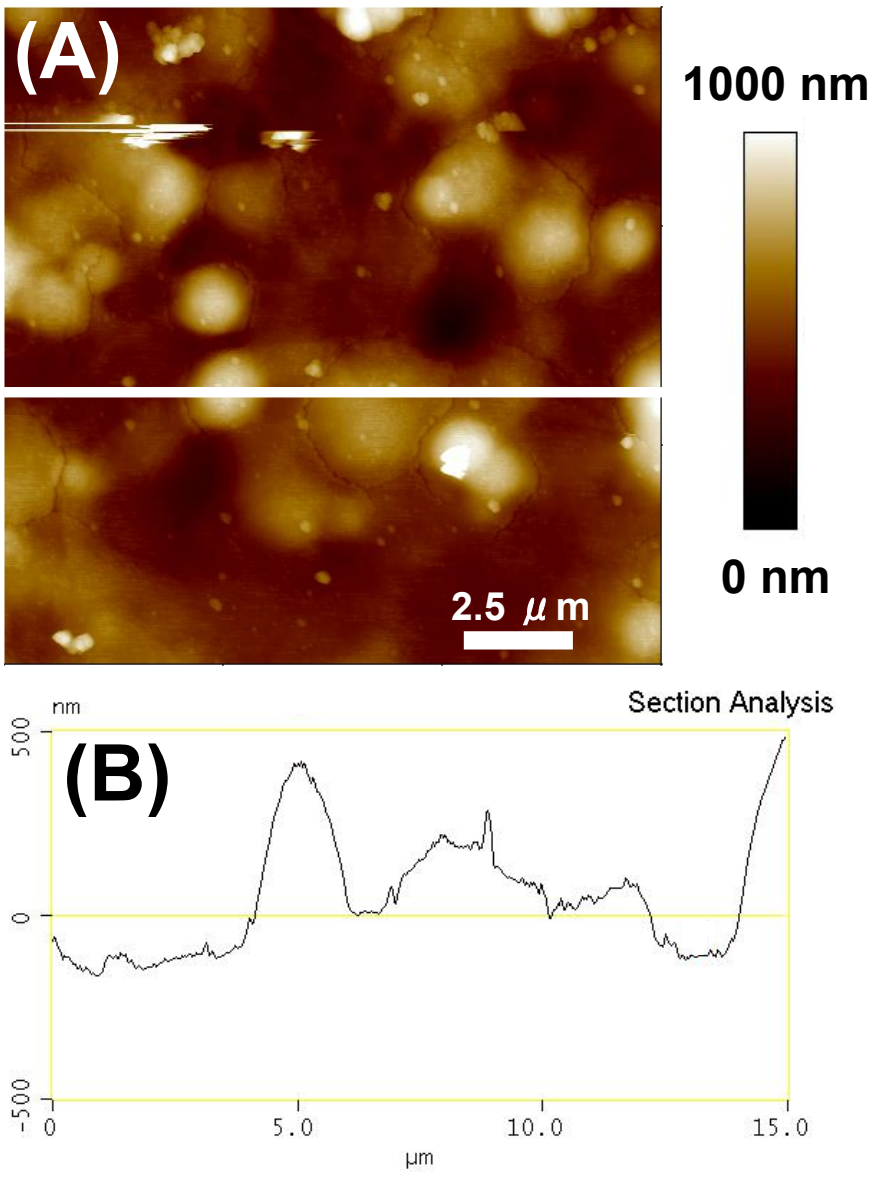

Figure 2.7: **(A)** Topographic AFM image of CdS layer on the CIGS nanocrystal film. **(B)** Line scan (section analysis) of the AFM topography taken along the white line in image (A).

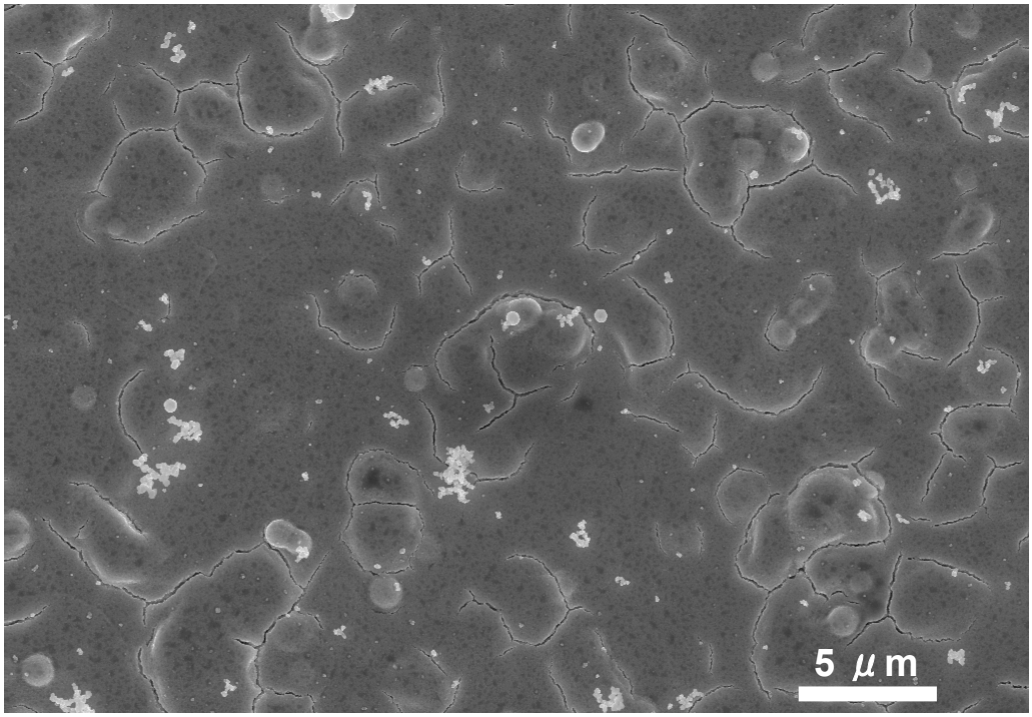

Figure 2.8: Scanning electron microscope (SEM) image of the CIGS nanocrystal layer of the device capped with the CdS layer.

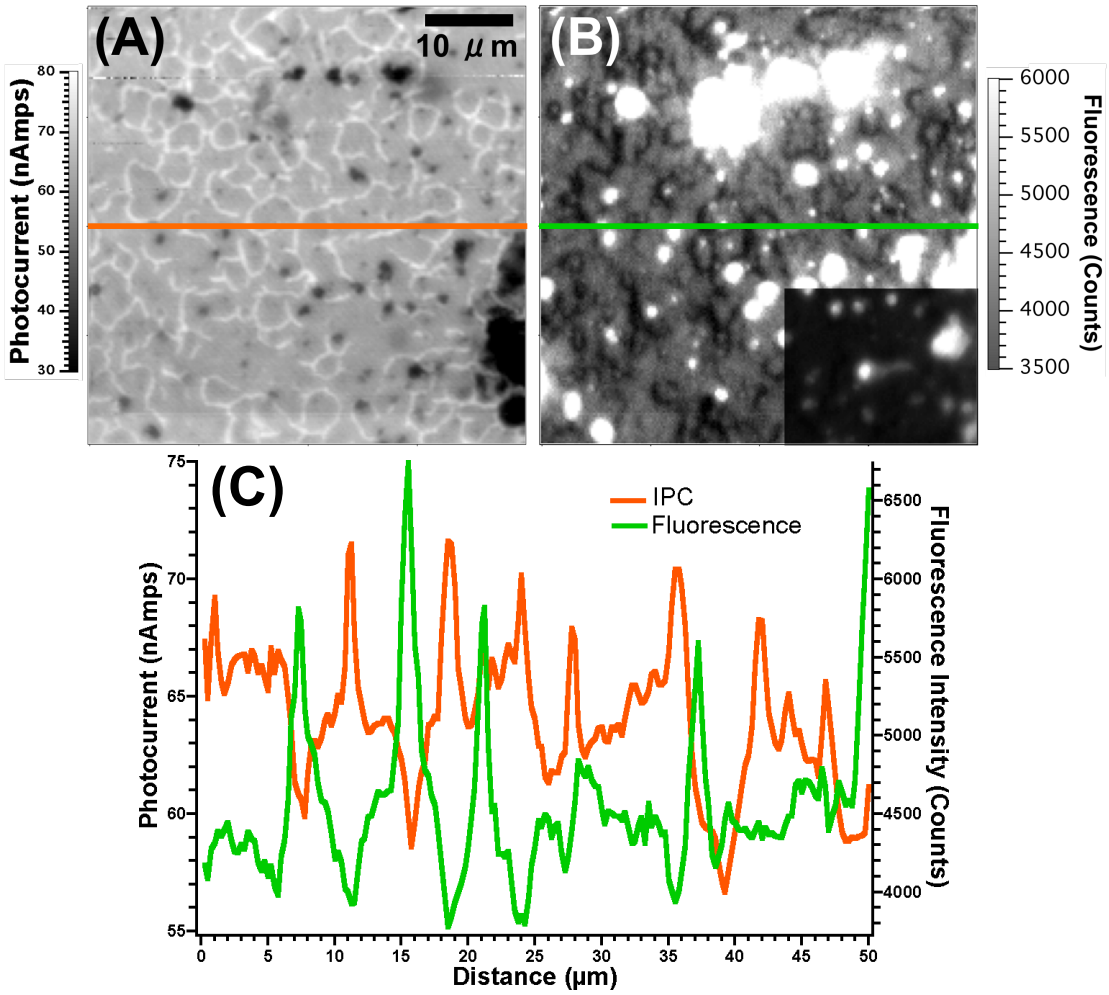

Figure 2.9: Image maps of (**A**) zero-bias induced photocurrent (IPC) and (**B**) fluorescence intensity for a CdS-capped CIGS nanocrystal PV device. Overlay in lower right corner of (**B**): that area of the fluorescence image shown at a different, non-saturated contrast scale of 3,500 to 20,000 counts. The units for image (A) are not exact due to use of a non-calibrated lock-in amplifier. (**C**) Line scans of the IPC and fluorescence images taken at the location of the lines shown on the images of (A) and (B), this analysis highlights the anti-correlation of IPC with fluorescence.

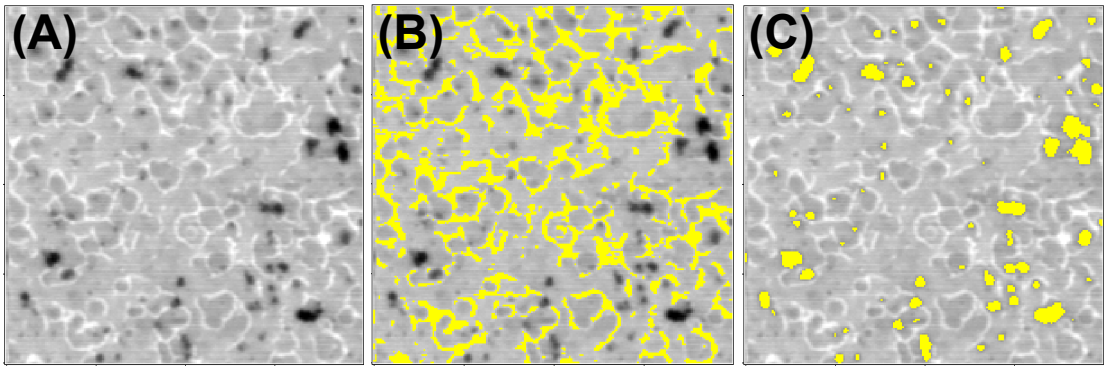

Figure 2.10: Image map of **(A)** zero-bias induced photocurrent (IPC) from Figure 2.3, and images with a threshold set to highlight areas of **(B)** high photocurrent and **(C)** low photocurrent.

Figure 2.11 shows the different steps of data processing needed to convert the lock-in measured voltage values to the corresponding magnitude of induced photocurrent the voltages represent. As mentioned, since the photocurrent levels from the LBIC technique are low (in this case on the order of nA), a pre-amplifier built in house that also functioned as a current to voltage converter was used. The same circuit board containing the pre-amplifier was equipped with a voltage biasing system to allow for scanning the voltage bias in the LVPC measurement.

Figure 2.11A shows the raw data as collected from the lock-in amplifier. Since the measurement is of the wave amplitude oscillating between the light and dark current values of the chopped incident light beam, the sign does not change. However, the bias voltage where the photocurrent changes direction and thus sign, can be distinguished by the peak (lowest negative) value of the graph. This peak is the point at which the light and dark current states are equal and thus yields the value of the background of the measurement. **Figure 2.11B** shows the same data as A but with the background noise (distance from peak data point to 0) subtracted. Since this is the point where the sign of the photocurrent changes direction, the sign of all the data collected at higher bias values than the peak was changed to positive as shown in **Figure 2.11C**. The data was then put through a 5-point boxcar average **Figure 2.11D**. The true photocurrent of the device is the peak-to-peak amplitude of the chopped signal. As the lock-in measured the RMS amplitude, the correction factor to convert the lock-in measured values to peak-to-peak amplitude was a factor of 2.79, as measured with a function generator and oscilloscope. **Figure 2.11E** shows the corrected peak-to-peak wave amplitude values that have also been corrected for the lock-in sensitivity setting used. **Figure 2.11F** shows the finalized LVPC data after conversion to Amps with Ohm's law and the resistance used in the pre-amplifier, along with conversion of mA to nA.

As discussed, the bias at zero current in the LVPC measurement is not the same as the V_{oc} of the device. The bias at which the LVPC is zero will be slightly higher than the V_{oc}. In the limit that the dark current is small, the bias at zero voltage will approach the V_{oc}.

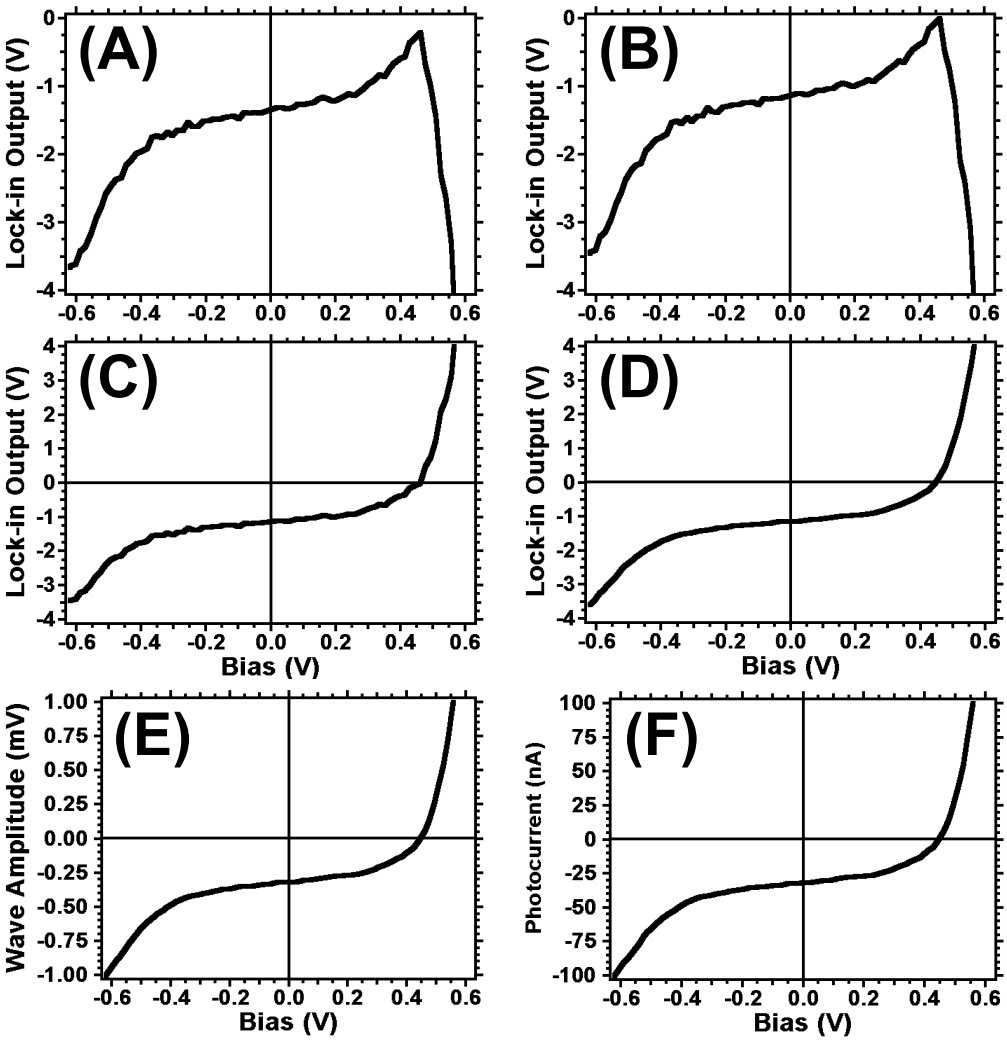

Figure 2.11: **A)** through **F)** show graphs of the LVPC data at different steps as the voltages measured by the lock-in amplifier are converted back to the original induced photocurrent (IPC) values.

Acknowledgements for co-author contributions: Goodfellow, Akhavan, Panthani and Prof. Korgel fabricated the CIGS devices and provided valuble discussions for data interpretation. Glaz helped to rescan the devices in order to verify the original data. Prof. Vanden Bout provided valuble direction for the work, mainly in instrument development and data interpretation.

2.6 REFERENCES

1. Bredas, J.-L.; Durrant, J. R., Organic Photovoltaics. *Accounts of Chemical Research* **2009**, *42*, 1689-1690.

2. Goetzberger, A.; Hebling, C.; Schock, H. W., Photovoltaic Materials, History, Status and Outlook. *Materials Science & Engineering R-Reports* **2003**, *40*, 1-46.

3. Yang, X.; Loos, J., Toward High-Performance Polymer Solar Cells: The Importance of Morphology Control. *Macromolecules* **2007**, *40*, 1353-1362.

4. Krebs, F. C., Fabrication and Processing of Polymer Solar Cells: A Review of Printing and Coating Techniques. *Solar Energy Materials and Solar Cells* **2009**, *93*, 394-412.

5. Brabec, C. J., Organic Photovoltaics: Technology and Market. *Solar Energy Materials and Solar Cells* **2004**, *83*, 273-292.

6. Saunders, B. R.; Turner, M. L., Nanoparticle-Polymer Photovoltaic Cells. *Advances in Colloid and Interface Science* **2008**, *138*, 1-23.

7. Spanggaard, H.; Krebs, F. C., A Brief History of the Development of Organic and Polymeric Photovoltaics. *Solar Energy Materials and Solar Cells* **2004**, *83*, 125-146.

8. McNeill, C. R.; Watts, B.; Thomsen, L.; Belcher, W. J.; Kilcoyne, A. L. D.; Greenham, N. C.; Dastoor, P. C., X-Ray Spectromicroscopy of Polymer/Fullerene Composites: Quantitative Chemical Mapping. *Small* **2006**, *2*, 1432-1435.

9. Pingree, L. S. C.; Reid, O. G.; Ginger, D. S., Electrical Scanning Probe Microscopy on Active Organic Electronic Devices. *Advanced Materials* **2009**, *21*, 19-28.

10. Kamat, P. V., Quantum Dot Solar Cells. Semiconductor Nanocrystals as Light Harvesters. *Journal of Physical Chemistry C* **2008**, *112*, 18737-18753.

11. Olson, D. C.; Shaheen, S. E.; Collins, R. T.; Ginley, D. S., The Effect of Atmosphere and ZnO Morphology on the Performance of Hybrid Poly(3-hexylthiophene)/Zno Nanofiber Photovoltaic Devices. *J. Phys. Chem. C* **2007**, *111*, 16670-16678.

12. Cadby, A.; Khalil, G.; Fox, A. M.; Lidzey, D. G., Mapping Exciton Quenching in Photovoltaic-Applicable Polymer Blends Using Time-Resolved Scanning Near-Field Optical Microscopy. *Journal of Applied Physics* **2008**, *103*, 093715.

13. Rozanski, L. J.; Cone, C. W.; Ostrowski, D. P.; Bout, D. A. V., Effect of Film Morphology on the Energy Transfer to Emissive Green Defects in Dialkyl Polyfluorenes. *Macromolecules* **2007**, *40*, 4524-4529.

14. Kwak, E. S.; Kang, T. J.; Bout, D. A. V., Fluorescence Lifetime Imaging with Near-Field Scanning Optical Microscopy. *Analytical Chemistry* **2001**, *73*, 3257-3262.

15. Teetsov, J.; Vanden Bout, D. A., Near-Field Scanning Optical Microscopy Studies of Nanoscale Order in Thermally Annealed Films of Poly(9,9-diakylfluorene). *Langmuir* **2002**, *18*, 897-903.

16. Gao, Y. Q.; Grey, J. K., Resonance Chemical Imaging of Polythiophene/Fullerene Photovoltaic Thin Films: Mapping Morphology-Dependent Aggregated and Unaggregated C=C Species. *Journal of American Chemical Society* **2009**, *131*, 9654-9662.

17. Coffey, D. C.; Ginger, D. S., Time-Resolved Electrostatic Force Microscopy of Polymer Solar Cells. *Nature Materials* **2006**, *5*, 735-740.

18. Coffey, D. C.; Reid, O. G.; Rodovsky, D. B.; Bartholomew, G. P.; Ginger, D. S., Mapping Local Photocurrents in Polymer/Fullerene Solar Cells with Photoconductive Atomic Force Microscopy. *Nano Letters* **2007**, *7*, 738-744.

19. Palermo, V.; Otten, M. B. J.; Liscio, A.; Schwartz, E.; de Witte, P. A. J.; Castriciano, M. A.; Wienk, M. M.; Nolde, F.; De Luca, G.; Cornelissen, J. J. L. M.; Janssen, R. A. J.; Müllen, K.; Rowan, A. E.; Nolte, R. J. M.; Samori, P., The Relationship between Nanoscale Architecture and Function in Photovoltaic Multichromophoric Arrays as Visualized by Kelvin Probe Force Microscopy. *Journal of the American Chemical Society* **2008**, *130*, 14605-14614.

20. Hoppe, H.; Glatzel, T.; Niggemann, M.; Hinsch, A.; Lux-Steiner, M. C.; Sariciftci, N. S., Kelvin Probe Force Microscopy Study on Conjugated Polymer/Fullerene Bulk Heterojunction Organic Solar Cells. *Nano Letters* **2005**, *5*, 269-274.

21. Douheret, O.; Swinnen, A.; Bertho, S.; Haeldermans, I.; D'Haen, J.; D'Olieslaeger, M.; Vanderzande, D.; Manca, J. V., High-Resolution Morphological and Electrical Characterisation of Organic Bulk Heterojunction Solar Cells by Scanning Probe Microscopy. *Progress in Photovoltaics* **2007**, *15*, 713-726.

22. Palermo, V.; Palma, M.; Samori, P., Electronic Characterization of Organic Thin Films by Kelvin Probe Force Microscopy. *Advanced Materials* **2006**, *18*, 145-164.

23. Pingree, L. S. C.; Reid, O. G.; Ginger, D. S., Imaging the Evolution of Nanoscale Photocurrent Collection and Transport Networks During Annealing of Polythiophene/Fullerene Solar Cells. *Nano Letters* **2009**, *9*, 2946-2952.

24. Bull, T. A.; Pingree, L. S. C.; Jenekhe, S. A.; Ginger, D. S.; Luscombe, C. K., The Role of Mesoscopic PCBM Crystallites in Solvent Vapor Annealed Copolymer Solar Cells. *Acs Nano* **2009**, *3*, 627-636.

25. Romero, M. J.; Morfa, A. J.; Reilly, T. H.; van de Lagemaat, J.; Al-Jassim, M., Nanoscale Imaging of Exciton Transport in Organic Photovoltaic Semiconductors by Tip-Enhanced Tunneling Luminescence. *Nano Lett*. **2009**, *9*, 3904-3908.

26. Durose, K.; Asher, S. E.; Jaegermann, W.; Levi, D.; McCandless, B. E.; Metzger, W.; Moutinho, H.; Paulson, P. D.; Perkins, C. L.; Sites, J. R.; Teeter, G.; Terheggen, M., Physical Characterization of Thin-Film Solar Cells. *Progress in Photovoltaics* **2004**, *12*, 177-217.

27. Acciarri, M.; Binetti, S.; Racz, A.; Pizzini, S.; Agostinelli, G., Fast LBIC in-Line Characterization for Process Quality Control in the Photovoltaic Industry. *Solar Energy Materials and Solar Cells* **2002**, *72*, 417-424.

28. McNeill, C. R.; Frohne, H.; Holdsworth, J. L.; Dastoor, P. C., Direct Influence of Morphology on Current Generation in Conjugated Polymer:Methanofullerene Solar Cells Measured by Near-Field Scanning Photocurrent Microscopy. *Synthetic Metals* **2004**, *147*, 101-104.

29. McNeill, C. R.; Frohne, H.; Holdsworth, J. L.; Dastoor, P. C., Near-Field Scanning Photocurrent Measurements of Polyfluorene Blend Devices: Directly Correlating Morphology with Current Generation. *Nano Letters* **2004**, *4*, 2503-2507.

30. McNeill, C. R.; Frohne, H.; Holdsworth, J. L.; Furst, J. E.; King, B. V.; Dastoor, P. C., Direct Photocurrent Mapping of Organic Solar Cells Using a Near-Field Scanning Optical Microscope. *Nano Letters* **2004**, *4*, 219-223.

31. Gao, Y. Q.; Martin, T. P.; Thomas, A. K.; Grey, J. K., Resonance Raman Spectroscopic and Photocurrent Imaging of Polythiophene/Fullerene Solar Cells. *Journal of Physical Chemistry Letters* **2010**, *1*, 178-182.

32. Thantsha, N. M.; Macabebe, E. Q. B.; Vorster, F. J.; van Dyk, E. E., Opto-Electronic Analysis of Silicon Solar Cells by LBIC Investigations and Current-Voltage Characterization. *Physica B-Condensed Matter* **2009**, *404*, 4445-4448.

33. Riehn, R.; Stevenson, R.; Richards, D.; Kang, D.-J.; Blamire, M.; Downes, A.; Cacialli, F., Local Probing of Photocurrent and Photoluminescence in a Phase-Separated Conjugated-Polymer Blend by Means of Near-Field Excitation. *Advanced Functional Materials* **2006**, *16*, 469-476.

34. Panthani, M. G.; Akhavan, V.; Goodfellow, B.; Schmidtke, J. P.; Dunn, L.; Dodabalapur, A.; Barbara, P. F.; Korgel, B. A., Synthesis of $CuInS_2$, $CuInSe_2$, and $Cu(In_xGa_{1-X})Se_2$ (CIGS) Nanocrystal "Inks" for Printable Photovoltaics. *Journal of the American Chemical Society* **2008**, *130*, 16770-16777.

35. Repins, I.; Contreras, M. A.; Egaas, B.; DeHart, C.; Scharf, J.; Perkins, C. L.; To, B.; Noufi, R., 19.9%-Efficient Zno/Cds/$CuInGaSe_2$ Solar Cell with 81.2% Fill Factor. *Progress in Photovoltaics* **2008**, *16*, 235-239.

36. Derkaoui, Z.; Kebbab, Z.; Miloua, R.; Benramdane, N., Theoretical Study of Optical Characteristics of Multilayer Coatings ZnO/CdS/CdTe Using First-Principles Calculations. *Solid State Communications* **2009**, *149*, 1231-1235.

37. McCandless, B. E.; Shafarman, W. N. Chemical Surface Deposition of Ultra-Thin Semiconductors. U.S. Patent 6,537,845, March 25, 2003.

Chapter 3: Correlation of Morphology with Photocurrent Generation in a Polymer Blend Photovoltaic Device

3.1 Introduction

Photovoltaics (PV) provide an environmentally friendly alternative for local energy production. As the world's energy demand continues to grow and the finite reserves of non-renewable fossil fuels continue to decrease, new methods for energy production are needed.[1] However, the price of present PV technology is too high to allow for wide spread use.[2,3] In order for PV technology to be a useful form of energy production, advances must be made to improve efficiency and lower cost.

One class of PV materials that shows promise for reducing PV cost is that of solution processable organic materials.[1-6] This class of organic materials possesses semiconducting properties that result from the delocalization of electrons along a conjugated molecular backbone. Alkyl side chains off of this backbone allow the materials to be soluble in common organic solvents and thus can be deposited at room temperature through numerous solution processing techniques.[7,8] This solution processing allows for significantly lower fabrication costs, however, the efficiency of these materials in PV devices is still too low for wide spread commercial use.[3]

A significant factor that affects the PV properties of these materials is the local morphology.[7,9] Most systems are binary, composed of a donor and an acceptor. The two molecules are mixed in a common solvent and then solution deposited simultaneously onto a substrate, forming a complex intermixed morphology known as a bulk heterojunction (BHJ) PV.[5,6,8,10] While the materials are in solution they are able to move around freely. However, once the solution is deposited, the solvent begins to dry and the molecules gradually lose mobility until being trapped once the solvent has dried. These systems rarely reach an equilibrium state before the solvent dries and thus the resulting

films possess a complex, kinetically determined morphology that varies across the PV. These morphological differences have significant effects on PV properties, and as such, need to be well understood in order for this class of materials and technology to move forward.

The emphasis of this work is on the effect that local morphological variations have on electronic and optical properties of a particular polymer blend donor and acceptor system: poly(9,9-dioctylfluorene-*co*-*bis*-*N*,*N*-(4-butylphenyl)-*bis*-*N*,*N*-phenyl-1,4-phenylenediamine (PFB) and poly(9,9-dioctylfluorene-*co*-benzothiadiazole) (F8BT). These polymers form a type-II heterojunction and charge separation is energetically favorable regardless of which polymer absorbs light.[11,12] When a 1:1 ratio solution of these materials is deposited on a substrate, the two polymers undergo phase separation through a favorable enthalpy of de-mixing.[13,14] The extent of phase separation in the film is affected by the amount of time the polymers are free to move before the solvent dries, the molecular weight of the polymers and the concentration of the deposited solution.[6,14,15] With longer solvent evaporation times, higher molecular weights and higher concentrations all resulting in longer-scale phase separation.[16] Once the solvent has dried the polymers are trapped in a kinetically determined, variable morphology. As PFB forms a wetting layer on the substrate, the micro-scale phases can be determined from an atomic force microscopy (AFM) topography image, which show alternating low and high lying domains.[14,17]

Chemical composition variations on films made from these polymers have been studied with Raman microscopy and scanning transmission X-ray microscopy (STXM).[15,18-23] These measurements showed the micro-scale domains are not pure phases but rather are alternating PFB-rich and F8BT-rich domains, with the interface region between the domains being the most pure. Thus, these films posses both a micro-scale

and nano-scale intermixing of the two polymers. There have been numerous studies on this material system in an effort to determine the effect this complex morphology has on PV properties.

Earlier studies suggested that charge transport is the limiting factor of PV performance in the PFB:F8BT blend.[13,15,24,25] From Kelvin probe force microscopy (KPFM), the most charge build up under illumination was observed at the interface of the domains suggesting that region to be the most efficient at PC generation, through to result from the enhanced charge transport to the electrodes at the higher purity domain interface.[15,25] However, later studies showed that the majority of the photocurrent (PC) was generated within the micro-scale domains and not at the interface between domains.[26-28] A recent study, used a variety of illumination wavelengths to map PC generation in a functional PFB:F8BT device with micro-scale domains on the order of 5 microns.[28] This study found that regardless of illumination wavelength, the same regions of the device produced the most PC, the F8BT-rich domains. Also, the strongest exciplex emission was observed in the PFB-rich domains, that STXM experiments have shown to be more intermixed (70% PFB) than the more pure F8BT-rich domains (90% F8BT).[19] This suggested more recombination of charge carriers occurs when there is a greater amount of intermixing between the two polymers.

The presented work studies the complex morphology of an as-fabricated PFB:F8BT blend PV device which possesses micro-scale phase separation on the order of 0.5 to 1 microns. This is a smaller phase separation than most studies in the literature that use higher molecular weight polymers and have micro-scale domains on the order of 5 microns. Raman microscopy and STXM have not been used to quantitatively map the chemical composition variations in films made from polymers of the molecular weights presented here. Scanning photocurrent (PC) and photoluminescence (PL) microscopy was

employed to create image maps of local PV and optical properties at a resolution of around 250 nm. These measurements allowed correlation of PC generation with PL from the specific emissive species in the device: PFB, F8BT and exciplex. The morphological regions of the device with the highest amount of PC generation were found to change under different illumination sources.

3.2 Experimental Methods

Materials were purchased from American Dye Source and used as is. PFB had a molecular weight of 12.5 kDa, while F8BT had a molecular weight of 28 kDa. Both polymers had a 2.2 polydispersity index (PDI).

'Bulk' Absorbance and Photoluminescence measurements: Absorbance measurements were collected using an ultraviolet-visible (UV-VIS, Agilent 8453) spectrometer and photoluminescence measurements were collected using a Fluorolog-3 (Horiba Jobin-Yvon) fluorometer.

Atomic Force Microscopy (AFM) topography measurements were performed in tapping mode using a Veeco Dimension 3100 AFM with a Nanoscope IV controller and cantilevers with resonance frequency of around 300 kHz from Vista Probes (T300R).

PV Device Fabrication: Indium Tin Oxide (ITO) was washed with detergent (Alconox) and water, rinsed with de-ionized water and sonicated in iso-propanol and acetone for ten minutes each. Two types of ITO were used both with a sheet resistance of 5-15 Ohms but on different thicknesses of glass. One type of ITO on thicker glass (1.1 mm thick) was purchased from Delta Technologies, Inc. (CB-50IN-0111). For scanning PC and PL microscopy measurements, devices were fabricated using ITO on cover glass (0.13 -0.17 mm thick) as purchased from Evaporated Coatings, Inc (09UTA507-A). This allowed for use of oil immersion optics for improved resolution.

The ITO was plasma etched at 50 W power under 40% oxygen atmosphere followed by spin casting onto the ITO a ~40 nm thick layer of PEDOT:PSS (poly(3,4-ethylenedioxythiophene):poly(styrenesulfonate); Clevios P VP AI 4083 from HC Stark). Before spin coating, the PEDOT:PSS solution was sonicated for fifteen minutes and then filtered through a 0.45 micron PVDF filter. After spin coating, the PEDOT:PSS layer was annealed in air at 140°C for ten minutes after which the substrates were transferred to a nitrogen filled glove box (Mbraun).

A 1:1 ratio by weight solution of PFB:F8BT in either *p*-xylene or chloroform was prepared; 17 mg of each polymer for 1 mL *p*-xylene or 5 mg of each polymer for 1 mL chloroform. After the polymers were dissolved the solution was filtered through a 0.1 micron Teflon filter before spin casting. The devices cast from a chloroform solution were spin cast at 3000 RPM, and had a thickness of 90 ± 20 nm. These PVs were used for external quantum efficiency (EQE) measurements while the devices cast from *p*-xylene were used for the scanning PC and PL microscopy studies. The solution in *p*-xylene was filtered through a 0.1 micron Teflon filter before being spin cast at 1600 RPM to yield a 150 ± 20 nm thick PFB:F8BT layer. The devices were completed by thermally evaporating around 100 nm of aluminum (Al) in a vacuum chamber in the glove box. The Al was deposited through a shadow mask at a rate of around 0.8 Angstroms/second and a pressure of around $7x10^{-7}$ Torr. Under nitrogen atmosphere the completed devices were transferred to another nitrogen filled glove box (Mbraun) where 'bulk' current-voltage (IV) characteristics and an EQE spectrum were measured. The devices were encapsulated using Torr Seal and another glass substrate before being taken out of the glove box for scanning PC and PL microscopy measurements. After encapsulation, 'bulk' PV measurements were retested to confirm no damage to the device had occurred during the encapsulation process.

'Bulk' PV Characterization: The conventional IV characteristics of the devices were measured using a Keithley 2400 general purpose sourcemeter. The illumination source used was a Xenon lamp solar simulator (Newport) with an AM1.5 filter. The lamp intensity to 100 mW/cm^2 was set using a NIST calibrated silicon photodiode. The external quantum efficiency (EQE) measurements were performed by spectrally separating particular wavelengths of light from the Xenon lamp solar simulator with a monochrometer (Newport Cornerstone 260 1/4M), the light was not passed through the AM 1.5 filter in the EQE measurement. The incident light was chopped at 214 Hz and PC was measured in a Lock-in amplifier (Stanford Research Systems, SR830). The spectral light intensity was determined through use of calibrated silicon (Hamamatsu) and germanium (Judson) photodiodes. All 'bulk' characterization of the devices were collected through the transparent ITO electrode.

The Scanning PC and PL Microscopy experiment localizes the measurement of PV and optical properties in a functional PV device through illuminating only a small region of the device at a time and measuring the light induced properties from that region. This experimental setup is similar to the one previously described.[29] The incident laser light is focused onto the photoactive layer of the PV device through an oil immersion microscope objective (Zeiss) with a 1.25 numerical aperture and 100x magnification. This focused laser spot is around 250 nm in diameter for the incident wavelengths used in the reported experiments. One illumination source was a 408 nm diode laser (Coherent) and the other illumination source was the 488 nm line from an Argon-ion laser (CVI Melles Griot). The typical laser power used for scanning PC and PL images was 2.75 μW, which results in an incident power density of around 5.6 kW/cm^2 being focused onto the sample through the objective. Even with these high laser powers no significant alteration of the device was observed after scanning. With a piezoelectric stage (Physik

Instrumente, E-501.00) mounted onto an inverted microscope (Nikon Diaphot 300), the sample was raster scanned over this focused illumination spot and PC and PL measurements were collected at each step. This allowed image maps of variation in PC generation and optical properties to be created pixel by pixel.

The PC generated from the illuminated region of the device is measured through a pre-amplifier (Stanford Research Systems, SR570). For further noise filtering the incident laser light is chopped (Thorlabs optical chopper, MC2000) at a frequency of 150 Hz and the resulting oscillating PC signal was sent through the pre-amplifier to a DSP (digital signal processing) Lock-in amplifier (EG&G, 7220) for detection.

The PL from the illuminated region of the device is collected back through the same microscope objective and imaged through a spectrometer (Acton Research Corporation, model 150) onto an em-CCD (electron multiplying charge coupled device, the iXon 885 from Andor Technology). This setup allowed for collection of a PL spectrum, with a wavelength range of 160 nm, at each pixel in the image. However, the wavelength range needed to gain information about the PL from PFB, F8BT and exciplex is around 270 nm. Thus, with each scan the angle of the diffraction grating in the spectrometer was set to measure either the wavelength range from 425 to 585 nm (PFB-PL and F8BT-PL) or from 530 to 690 nm (F8BT-PL and exciplex-PL). From these data, images of the PL intensity from PFB, F8BT and exciplex were generated through integration of each local spectrum over a wavelength range unique to each emissive species. The integrated wavelength ranges used were: 435 to 475 nm for PFB-PL, 530 to 570 nm for F8BT-PL and 620 to 685 nm for exciplex-PL. As the F8BT-PL tail tends to dominate the low intensity exciplex-PL, a pure F8BT-PL spectrum was subtracted from each local spectrum. Before subtraction, the pure F8BT-PL spectrum was scaled to the

emission intensity of the local spectrum at 560 nm, a wavelength dominated by F8BT emission.

Local voltage-dependent photocurrent (LVPC) measurements were collected by repositioning the device so the illumination beam was located on a particular region of interest from the device. A bias voltage was applied to the device with a Keithley 2400 sourcemeter while the PC generated was measured in the same fashion as described earlier for the PC image maps. LabTracer 2.0 software (from Keithley Instruments, Inc.) was used to sweep the applied bias. For LVPC measurements at 408 and 488 nm the same laser power was used of around 215 nW, which resulted in an incident power density of around 440 W/cm^2 being focused onto the sample through the objective. Data processing of the LVPC measurements was performed as previously described.[29]

3.3 Results and Discussion

Figure 3.1a shows the absorbance bands of a thin film of pure PFB and pure F8BT, along with the absorbance of a blend film spin cast from *p*-xylene (the same conditions used to make the active layer of the devices used in this study). There is little overlap of the absorbance of the two polymers at wavelengths above 350 nm. As the absorbance and emission bands of these two polymers are separated in energy space, it is possible to selectively illuminate one or both polymers and determine the emission intensity from each polymer specifically. In this work, local PV and optical properties are measured with two different illumination sources. One, at 488 nm is only absorbed by F8BT (marked by light blue line in Figure 3.1a). The other illumination source at 408 nm is absorbed by both of the polymers (marked by purple line in Figure 3.1a). Through fitting the PFB:F8BT film absorbance with a linear combination of the pure polymer films absorbance spectra, it was estimated that PFB absorbs about 2.5 times that of F8BT

at 408 nm. The EQE of a PFB:F8BT PV device spin cast from chloroform (supporting information), traces the absorbance profile of the PFB:F8BT film. The correlation of EQE with film absorbance, demonstrates PC is generated in this PV system regardless of which polymer is being illuminated.

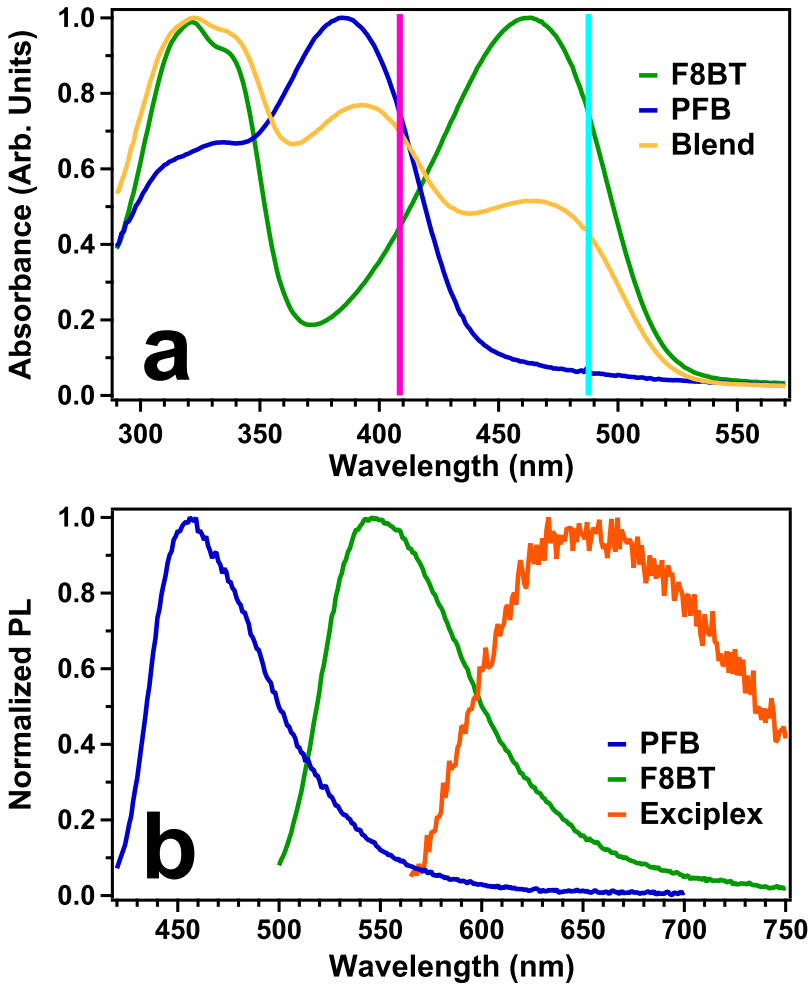

Figure 3.1: **a)** The absorbance spectra from films of pure F8BT, pure PFB and a PFB:F8BT blend spin cast from chloroform. The purple and light blue vertical lines are representative of the two excitation wavelengths used in this work: 408 nm and 488 nm laser light, respectively. **b)** Normalized PL spectra from films of pure PFB, pure F8BT and the exciplex. The exciplex PL spectrum was determined by subtracting the spectrum of pure F8BT from the spectrum of a PFB:F8BT blend film spin cast from chloroform.

The emission bands of pure PFB and F8BT films are also separated in wavelength. **Figure 3.1b** shows the PL spectra from the three emissive species present in a PFB:F8BT blend film: a PL spectrum from a pure PFB film, a pure F8BT film and an estimated PL spectrum for the exciplex. The exciplex PL spectrum was estimated by subtracting the pure F8BT film PL spectrum from a PL spectrum of the polymer blend film spin cast from chloroform, due to the fine scale intermixing of PFB:F8BT in this film the exciplex emission is more pronounced than in films spin cast from *p*-xylene. The exciplex-PL is attributed to radiative charge recombination from an excited state that is delocalized over a PFB and F8BT heterojunction.[30,31] A PL spectrum from 430 to 700 nm shows the PL intensity from PFB, F8BT and exciplex.

Figure 3.2 shows representative local voltage-dependent photocurrent (LVPC) measurements taken from regions of interest in the PV at either 408 nm or 488 nm illumination light. Numerous LVPC measurements were collected from regions of high and low PC or PL. The observed result is that the local diode characteristics and voltage at zero PC do not vary significantly for different regions of the device. The largest variations in PV performance are in the magnitude of the PC generated from each region, a value best observed by the magnitude of the PC at zero bias in the LVPC measurement. From these data it was concluded that image maps of the PC generation under zero bias voltage are sufficient to characterize the variations in PV performance across the device. Thus, all scanning PC and PL microscopy images reported here were collected under zero voltage bias conditions.

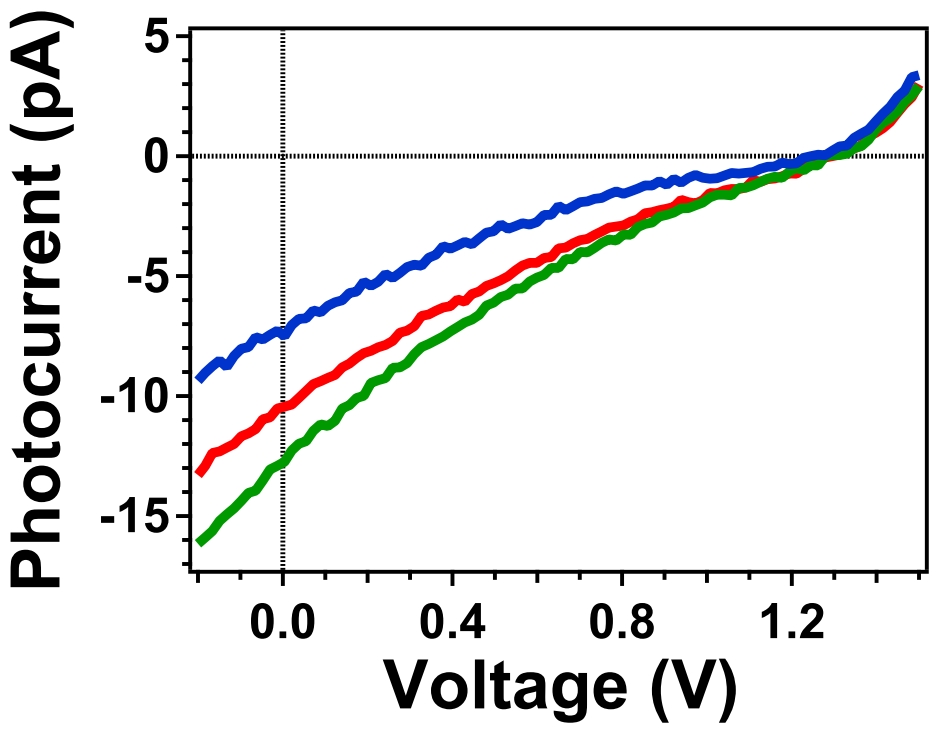

Figure 3.2: Graph of local voltage-dependent photocurrent (LVPC) measurements collected from regions of interest in a PFB:F8BT PV device with 408 nm light (blue trace) or 488 nm light (red and green traces). While many LVPC measurements were taken, the ones shown are representative of the differences in diode characteristics observed between regions. The shape of the traces are only significantly different in the magnitude of the PC generated, which is best observed by the value of PC at zero bias.

One set of scanning PC and PL microscopy images collected with 408 nm illumination are shown in **Figure 3.3**. While both polymers are absorbing light at this wavelength, it is estimated from bulk measurements that PFB absorbs about 2.5 times more light than F8BT. The simultaneously collected PC and PL spectra (from 425 to 585 nm) are used to create the image maps of local PC (Figure 3.3a), PFB-PL (Figure 3.3b), F8BT-PL (Figure 3.3c) and total-PL (Figure 3.3d). The contrast in the images appears to be dominated by the micro-scale morphological variations of the PFB:F8BT film; As the lateral contrast variations in intensity of these images are on a similar length scale to the micro-scale domains observed in an AFM topography image of a similar PFB:F8BT film to the one used in the device studied.

The total-PL and F8BT-PL images have the same contrast fluctuations. This shows the two images are highly correlated, demonstrating that the total-PL is dominated by F8BT-PL. This may be due to the higher PL quantum yield of F8BT than PFB; a pure F8BT film has been shown to have roughly a 4x higher PL efficiency than a pure PFB film.[16] In addition, fluorescence resonance energy transfer (FRET) is known to occur from PFB to F8BT.[32] Both of these factors result in the majority of the emission from the film coming from F8BT. The F8BT-PL with PFB-PL the images also show similar lateral features, however, the contrast of the images is inverted. This means the two images are anti-correlated, demonstrating that regions of more PFB-PL have less F8BT-PL and vice versa. As neither the PFB-PL or F8BT-PL images reach zero intensity, the micro-scale domains in the film are not pure and the device consists of alternating PFB-rich and F8BT-rich regions.

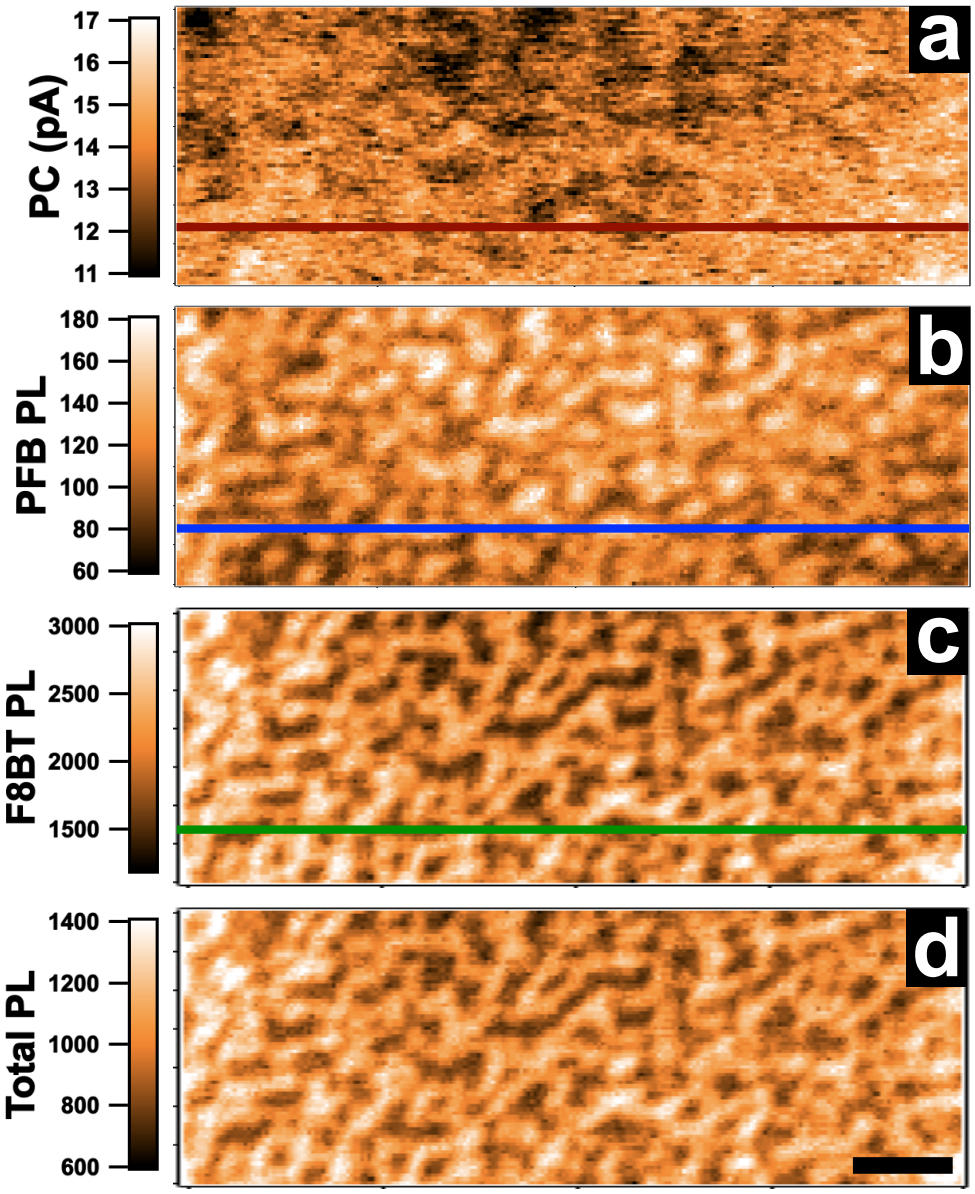

Figure 3.3: **a)** PC image map collected with 408 nm illumination and simultaneously collected PL images corresponding to **b)** PFB-PL, **c)** F8BT-PL and **d)** total-PL. The units of the PL images are in counts/channel, and the scale bar is 2.5 microns.

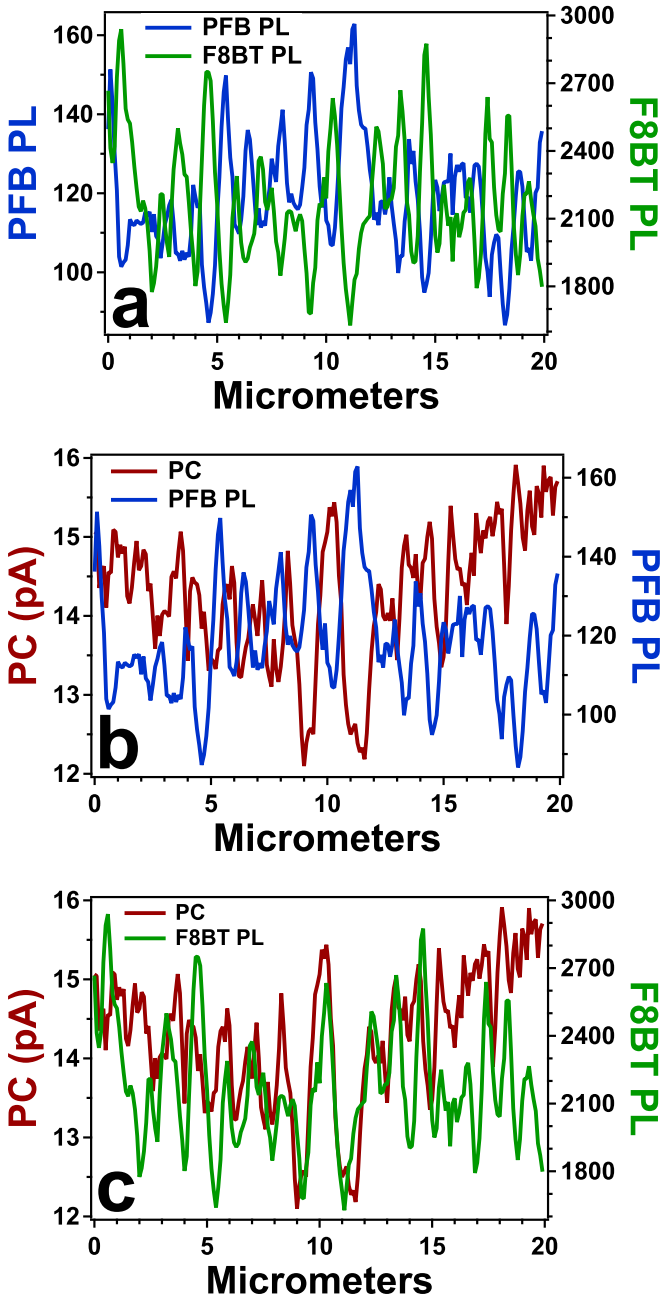

Figure 3.4: Line scans taken from the highlighted scan-lines shown on the images in Figure 3.3. **a)** Compare PFB-PL with F8BT-PL, **b)** compares PC with PFB-PL, and **c)** compares PC and F8BT-PL. Units of PL are in counts/channel.

The PFB-PL and PC image appear to be anti-correlated, however, this result is not as obvious from observation of the images. A more direct comparison of intensity fluctuations between images is obtained through a graph of the same single scan-line of each image. **Figure 3.4** displays graphs comparing intensity fluctuations extracted from the same scan-line in the PC, PFB-PL and F8BT-PL images (the scan-line used is highlighted on the images in Figure 3.3). The PC and PFB-PL line scans (Figure 3.4b) clearly displays anti-correlation in contrast. The anti-correlation of contrast in the PFB-PL and F8BT-PL images is also confirmed through the line scan comparison (Figure 3.4a). It logically follows that the PC and F8BT-PL images are correlated in intensity contrast, a result highlighted by the line scan comparison shown in Figure 3.4c. The correlation of the F8BT-PL and PC images shows that the most is generated in the F8BT-rich domains under 408 nm illumination.

A more thorough analysis, that uses data from the entire images to determine correlation or anti-correlation of intensity fluctuations, is a statistical linear correlation test (supporting information). This analysis calculates a linear correlation coefficient (r) between the two images. The value of r can range from -1 (completely anti-correlated) to 1 (completely correlated). A high, positive r of +0.9984 ± 0.0005 was calculated between the F8BT-PL and total-PL images (Figures 3.3c and 3.3d), confirming the two images are almost identical. The phase segregation of the polymers into micro-scale domains is observed from the anti-correlation between the images of F8BT-PL and PFB-PL (Figures 3.3b and 3.3c), the images have a negative value of r, -0.695 ± 0.006. The most interesting result is the correlation of the images of PC and F8BT-PL, which shows a strong positive correlation, r of +0.350 ± 0.008. Conversely, the PFB-PL and PC are anti-correlated with a negative r of -0.447 ± 0.008. This analysis confirms the main

conclusion from these data; with 408 nm illumination (where mostly PFB absorbs), the PC generation is highest in the F8BT-rich domains.

For examination the exciplex-PL, another set of scanning PC and PL microscopy data were collected under 408 nm illumination, with the local PL spectra collected over a different wavelength range (530 to 690 nm), **Figure 3.5**. The PC and PL spectra measurements are used to create the image maps of local PC generation (Figure 3.5a), exciplex-PL (Figure 3.5b), F8BT-PL (Figure 3.5c) and total-PL (Figure 3.5d). As these data were collected under the same illumination wavelength as the data shown in Figures 3.3 and 3.4, it was possible to re-affirm the trends observed in the previously described data. The same trends were observed with F8BT-PL and total-PL images being basically identical (Figures 3.5c and 3.5d; $r = +0.9965 \pm 0.0007$) along with the PC and F8BT-PL images being correlated (Figures 3.5a and 3.5c; line scans in **Figure 6a**; similar magnitude positive value of r equal to $+0.328 \pm 0.008$).

The additional feature of these data was comparison of images with that of exciplex-PL intensity. As the F8BT-PL tail tends to overshadow any exciplex-PL, a pure F8BT-PL spectrum was subtracted from each local PL spectrum after being scaled to the intensity of the local spectrum at 560 nm, a wavelength with only F8BT-PL. The intensity fluctuations in the exciplex-PL image do not appear to be particularly similar to the other PC and PL images, along with showing some unique features. The overall effect was calculated to be that the exciplex-PL is correlated with PC generation (Figures 3.5a and 3.5b, $r = +0.127 \pm 0.008$). From this fact and that F8BT-PL and PC generation are correlated, it follows that exciplex-PL and F8BT-PL are correlated (Figures 3.5b and 3.5c; $r = +0.136 \pm 0.008$). However, there are also some distinct regions of anti-correlation between exciplex-PL and both PC generation and F8BT-PL. This latter fact is highlighted in the scan-line graphs of Figures 3.6b and 3.6c, respectively.

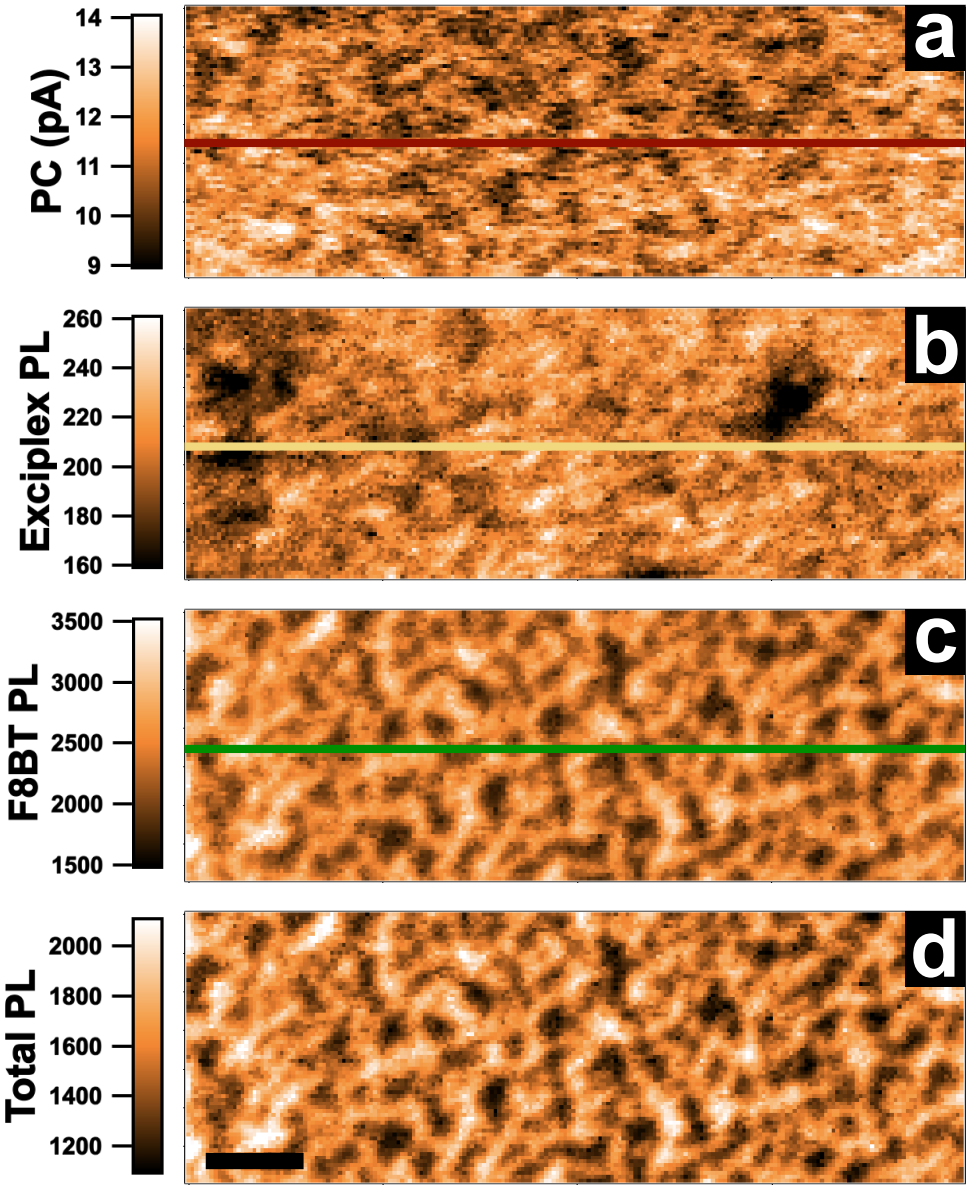

Figure 3.5: **a)** PC image map collected with 408 nm illumination and simultaneously collected PL images corresponding to **b)** exciplex-PL, **c)** F8BT-PL and **d)** total-PL. The units of the PL are in counts/channel and the scale bar is 2.5 microns.

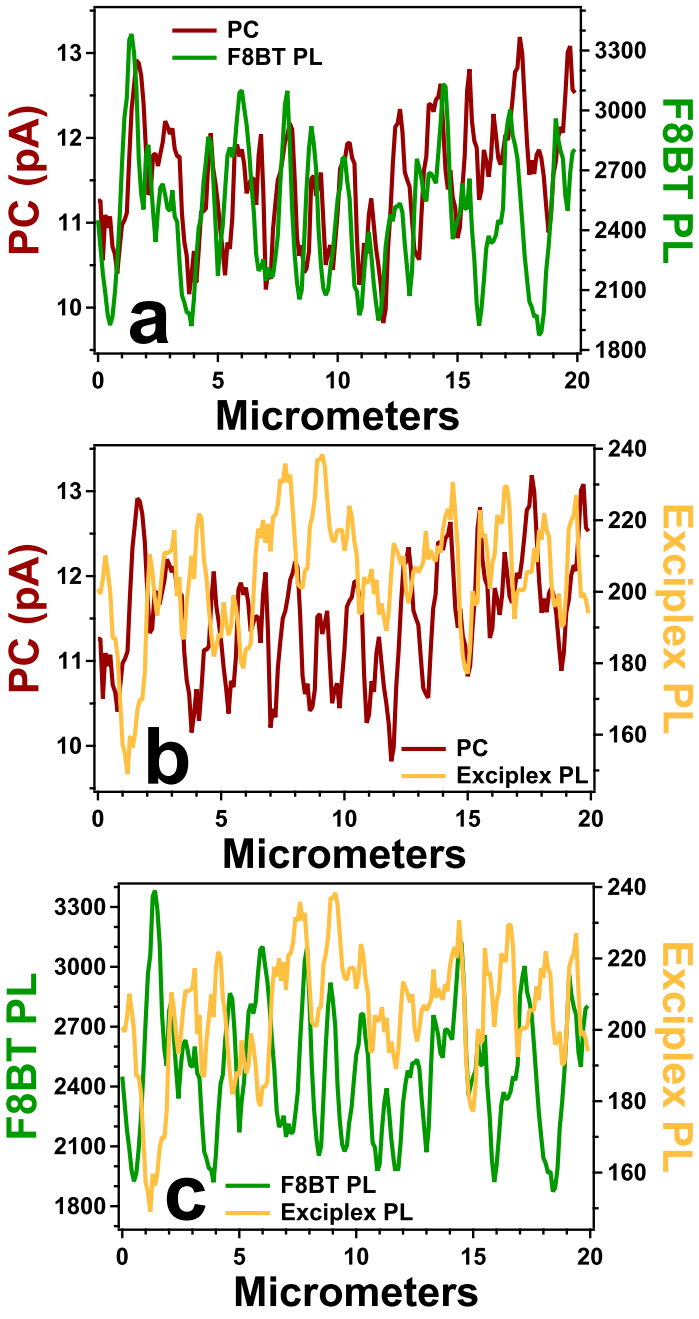

Figure 3.6: Line scans taken from the highlighted scan-lines shown on the images in Figure 3.5. **a**) Compares PC to F8BT-PL, **b**) compares PC with exciplex-PL and **c**) compares F8BT-PL with exciplex-PL. Units of PL are in counts/channel.

The main conclusion from these data is that the exciplex-PL is not a significant radiative loss mechanism for PC generation, as the PC and exciplex-PL images are not strongly anti-correlated. Results from the literature have suggested exciplex-PL is at highest intensity when there is the most intermixing of the PFB and F8BT.[28] Thus, the intensity fluctuations in the exciplex-PL image may highlight subtle variations in the fine scale intermixing of the two polymers, where the highest intensity exciplex-PL has the most polymer intermixing and vice versa.

In order to observe the local properties when only F8BT is illuminated, a third set of scanning PC and PL microscopy data were collected under 488 nm illumination, a wavelength where only F8BT absorbs light. **Figure 3.7** shows the corresponding images of PC generation (Figure 3.7a), exciplex-PL (Figure 3.7b), F8BT-PL (Figure 3.7c) and total-PL (Figure 3.7d). The total-PL intensity is again dominated by the F8BT-PL intensity, as the images of total-PL and F8BT-PL are basically identical ($r = 0.9975 \pm 0.0006$). However, the contrast in the PC image appears to be inverted with the F8BT-PL image. This is opposite to the result observed under 408 nm illumination. The anti-correlation of PC and F8BT-PL under 488 nm illumination is confirmed through comparison of the same scan-line in the PC and F8BT-PL image, **Figure 3.8a**, along with a negative value of r, -0.383 ± 0.007. This means the PFB-rich regions produce the most PC when illuminating only F8BT. Thus, once again the regions with the least concentration of absorber material are producing the most PC.

The exciplex-PL image again shows more complex intensity fluctuations than the other PC and PL images collected under 488 nm illumination. The overall effect was calculated to be similarly correlated with F8BT-PL ($r = +0.252 \pm 0.008$), but anti-correlated with the PC image ($r = -0.234 \pm 0.008$). Line scans comparing exciplex-PL to

F8BT-PL (Figure 3.8c) and exciplex-PL to PC generation (Figure 3.8b) show distinct regions of correlation and anti-correlation with both.

The main result from this work is that when only F8BT is illuminated (488 nm) the most PC is generated in the PFB-rich domains, but when both polymers are illuminated (408 nm), the opposite is observed, and the most PC is generated in F8BT rich domains. As the contrast in the PC image maps is reversed with 408 nm illumination (both polymers but mostly PFB absorbtion) when compared to the PC image under 488 nm illumination (only F8BT absorbtion), the effect of PFB illumination must overshadow the F8BT illumination when using 408 nm light. Thus, the conclusion is that the lesser the concentration of the polymer absorbing the light, the greater the PC generation. If PC generation differences resulted from better charge transport or collection in a particular domain type, one would expect the same domains to produce the most PC under both illumination conditions. Thus, the differences in PC image maps must then be due to either better charge separation or less charge recombination in the regions that have a lower concentration of the absorbing polymer. The better charge separation from illuminating the minority polymer is likely a result of the fact that the lower concentration polymer is always closer to the heterojunction than the higher concentration polymer. The observed result may also be due to vertical absorbance profile variations in the device. As the polymers both have a high absorbance, when the absorber is most concentrated a substantial amount of the incident light may be absorbed near the substrate, preventing a more comprehensive illumination of the bulk heterojunctions located in that region. While charge carrier recombination could be either radiative or non-radiative, the radiative recombination does not appear to be a significant loss mechanism in these devices as observed through the exciplex-PL and the fact that under 408 nm illumination, PC and total-PL images are correlated.

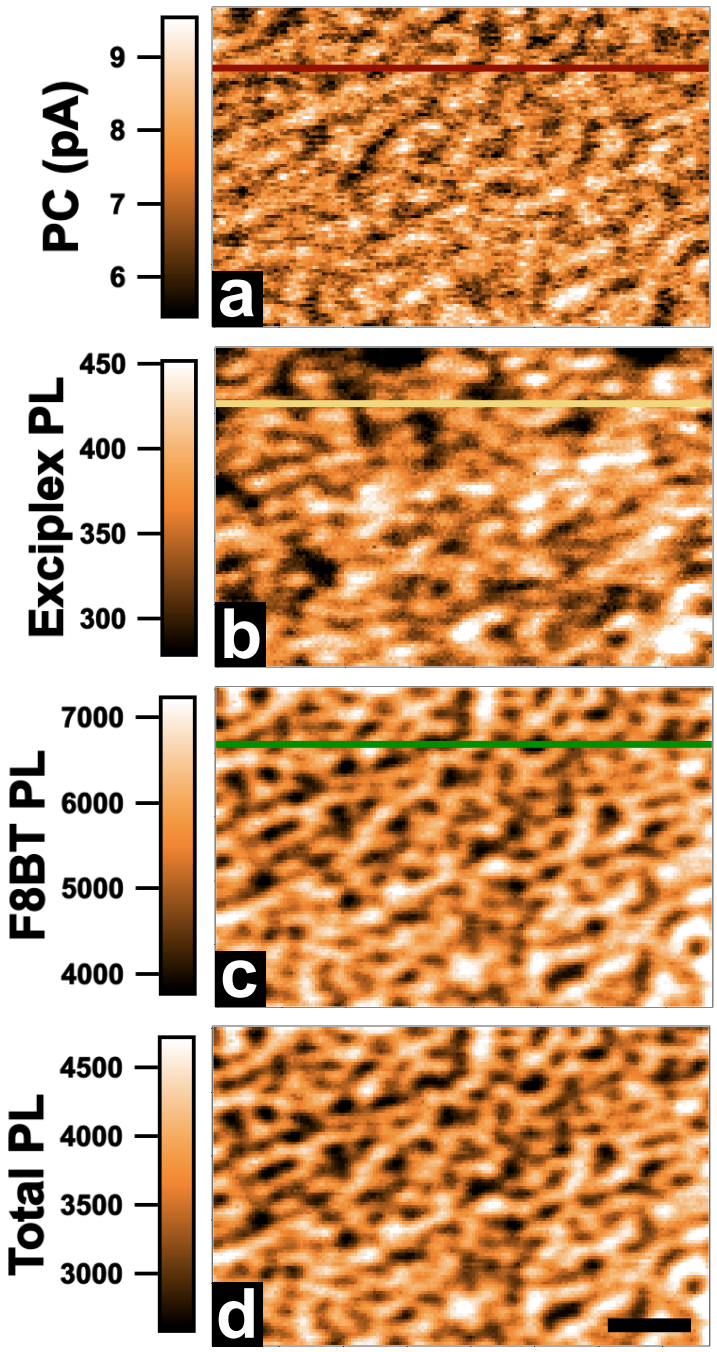

Figure 3.7: **a**) PC image map collected with 488 nm illumination (only F8BT absorbs light) and simultaneously collected PL images corresponding to **b**) exciplex-PL, **c**) F8BT-PL and **d**) total-PL. The units of the PL are in counts/channel and the scale bar is 2.5 microns.

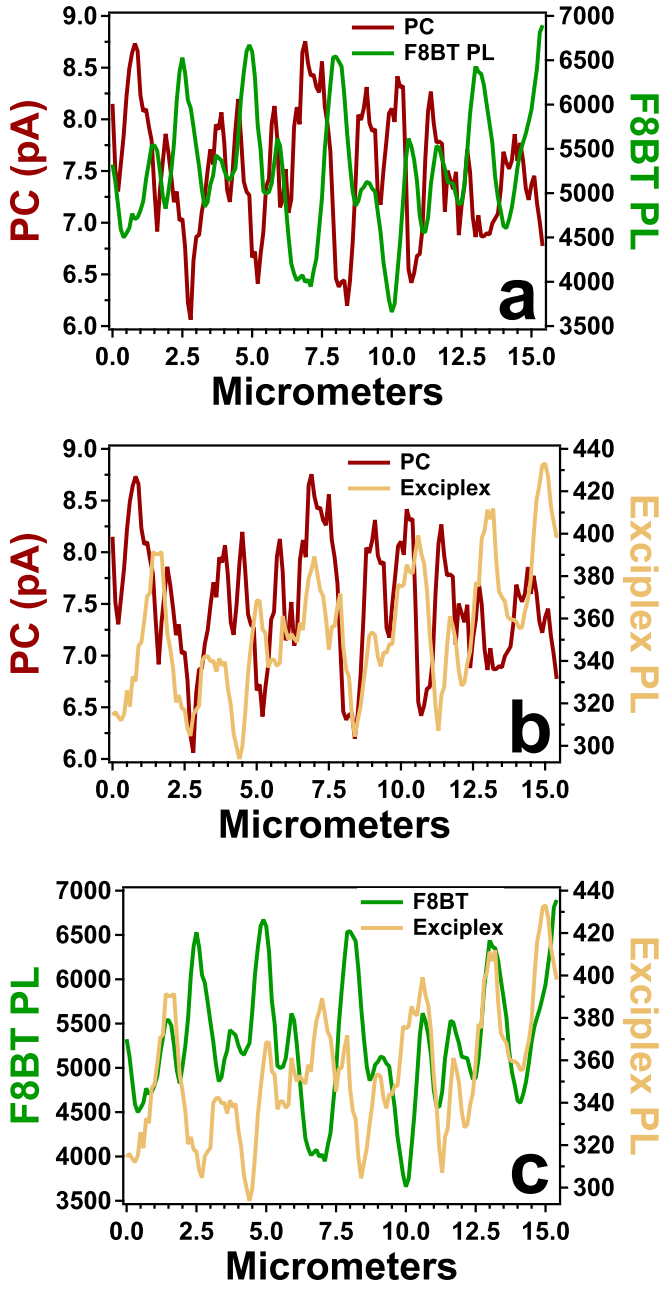

Figure 3.8: Line scans taken from the highlighted scan-lines shown on the images in Figure 3.7. **a)** Compares PC generation to F8BT-PL, **b)** compares PC generation with exciplex-PL and **c)** compares F8BT-PL with the exciplex-PL. Units of PL are in counts/channel.

3.4 CONCLUSIONS

Morphological effects on PV performance in PFB:F8BT devices were studied through local illumination of the device. Through LVPC measurements, it was observed that diode characteristics did not change between regions of different morphology, except in regard to the amount of PC generated. Thus, variations in PC generation across the device were sufficiently characterized by PC image maps collected at zero bias. The PL intensity was dominated by F8BT-PL under both of the illumination wavelengths used. Image maps of PFB-PL and F8BT-PL were strongly anti-correlated and showed an alternating network of PFB-rich and F8BT-rich domains on the length scale of 0.5 to 1 microns. A comparison of PC image maps with the PFB-PL and F8BT-PL images allowed for determination of which domains produced the most PC generation. This analysis showed that the domains that produced the highest PC generation were opposite under the different illumination wavelengths. Excitation of only the F8BT polymer with 488 nm illumination resulted in the most PC generated within the PFB-rich domains, while excitation of both polymers (but mostly PFB) with 408 nm illumination produced the most PC generation in the F8BT-rich domains. Thus, the morphology that contains the least amount of absorber material is the most effective at PC generation. This effect may be explained by the fact that the lower concentration polymer will always be closer to a heterojunction with the other material, which would increase charge separation efficiency in these regions. Another explanation may be from substantial variation in the vertical absorbance profile of the regions most concentrated in the absorber material. Through comparison of the PC image maps with the exciplex-PL images, the exciplex-PL was found to not be a significant radiative loss mechanism for charge carriers.

3.5 SUPPORTING INFORMATION

In this work, devices spin cast from *p*-xylene were studied rather than the typical devices cast from chloroform. Devices spin cast from chloroform have less time to phase separate than devices cast from *p*-xylene, due to quicker evaporation of chloroform. While the fine intermixing of donor and acceptor in devices cast from chloroform are shown to produce the highest PV efficiencies for this system,[16] the phase separation is below the resolution of the microscope technique used. Thus, in order to determine the morphological effects of micro-scale phase separation, PV devices spin-cast from *p*-xylene were studied.

One method to determine the morphological differences in PFB:F8BT films spin cast from chloroform or *p*-xylene is through AFM topography images (**Figure 3.9**). As the PFB forms a wetting layer on a substrate any phase separated domains, if present, are identifiable through a topographic AFM image: low-lying PFB-rich domains and high-lying F8BT-rich domains.[14,17] The length scale of the phase separated domains is on the order of 0.5 to 1 microns in the film spin cast from *p*-xylene (Figure 3.9a) while no micro-scale phase separation is observed in the film spin cast from chloroform (Figure 3.9b).

Performance of the *p*-xylene spin cast PVs were found to yield around an order of magnitude less power conversion efficiency (PCE) than those spin cast from chloroform, **Figure 3.10**. This is due to the higher J_{sc} and V_{oc} observed for a device spin cast from chloroform. The low FF observed in these devices is partially attributed to a Schottky barrier between polymer and the aluminum electrode and/or the fact that the materials may be slightly photoconductive. A deposition of a thin layer of calcium in between the PFB:F8BT and aluminum layers would lead to an Ohmic contact and may improve the

FF.[33] Details of the 'bulk' characterization experimental setup for these measurements are listed in the experimental section.

Another 'bulk' characterization method used was to measure a spectrum of the EQE of a PFB:F8BT device spin cast from chloroform (**Figure 3.11**). The EQE spectrum was shown to trace the absorbance spectrum of the PFB:F8BT blend film. The correlation of EQE with film absorbance demonstrates PC is generated in this PV system regardless of which polymer is being illuminated. This is expected as PFB and F8BT form a type II semiconductor heterojunction where charge separation is energetically favorable regardless of which polymer is absorbing the incident light.[12,34] The magnitude of the EQE values are comparable to others reported in the literature.[16,35,36] At the illumination wavelengths used in this work, the device is slightly more effective at 408 nm as compared to 488 nm in the bulk. This is also observed in the PC images, as the magnitude of the PC collected under 408 nm illumination shows slightly higher values than the images taken with 488 nm illumination.

Statistical Linear Correlation Test: The statistical linear correlations of the images compared in the main text were performed in IGOR Pro Version 6.22A using the "statslinearcorrelationtest" function. This analysis determined the linear correlation coefficient (r) between two data sets for n data points using equation 1.

$$r = \frac{\sum_{i=1}^{n} X_i Y_i - \frac{1}{n}\sum_{i=1}^{n} X_i \sum_{i=1}^{n} Y_i}{\sqrt{\left(\sum_{i=1}^{n} X_i^2 - \frac{1}{n}\left(\sum_{i=1}^{n} X_i\right)^2\right)\left(\sum_{i=1}^{n} Y_i^2 - \frac{1}{n}\left(\sum_{i=1}^{n} Y_i\right)^2\right)}} \qquad (1)$$

Then, using equation 2 the standard error (sr) of r is calculated.

$$sr = \sqrt{\frac{1 - r^2}{n - 2}} \qquad (2)$$

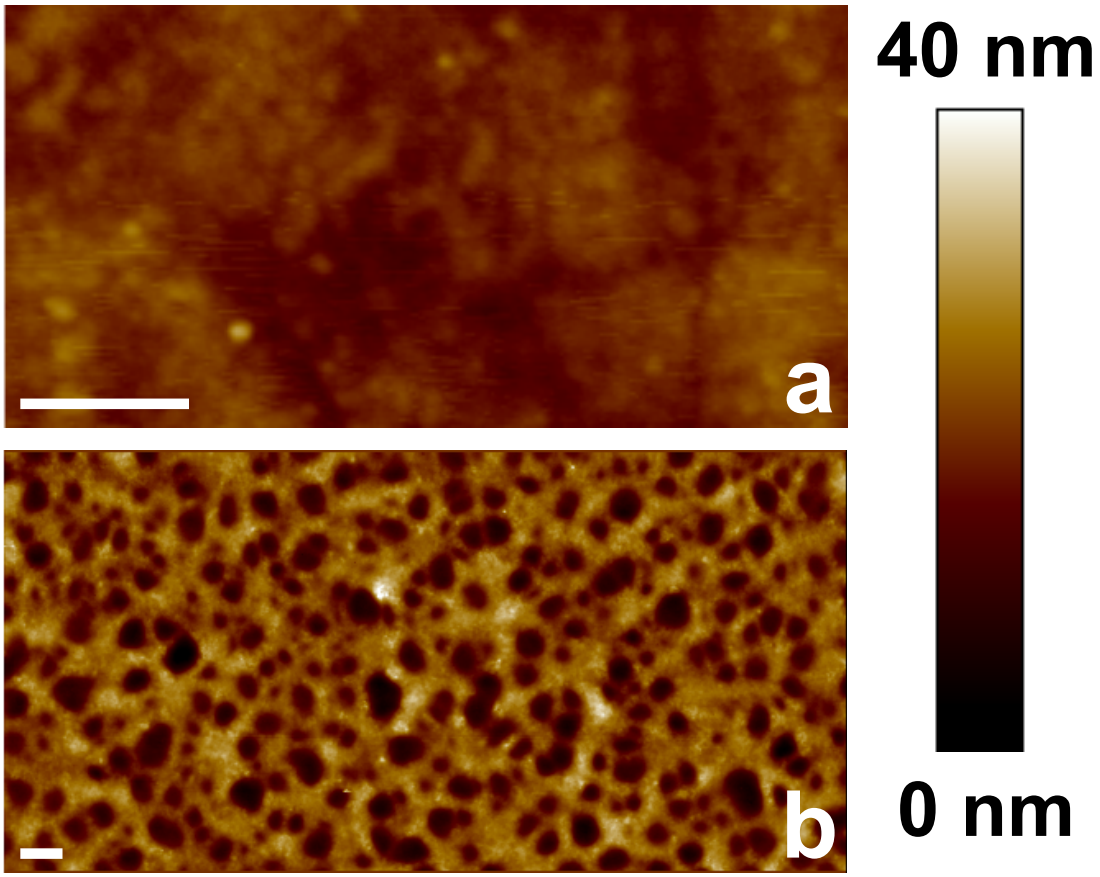

Figure 3.9: AFM topography images of PFB:F8BT film spin cast onto a glass substrate from (**a**) chloroform and (**b**) *p*-xylene solution. The parameters were the same as those used for the PV devices fabricated from chloroform or *p*-xylene. Both of the scale bars are 1 micron.

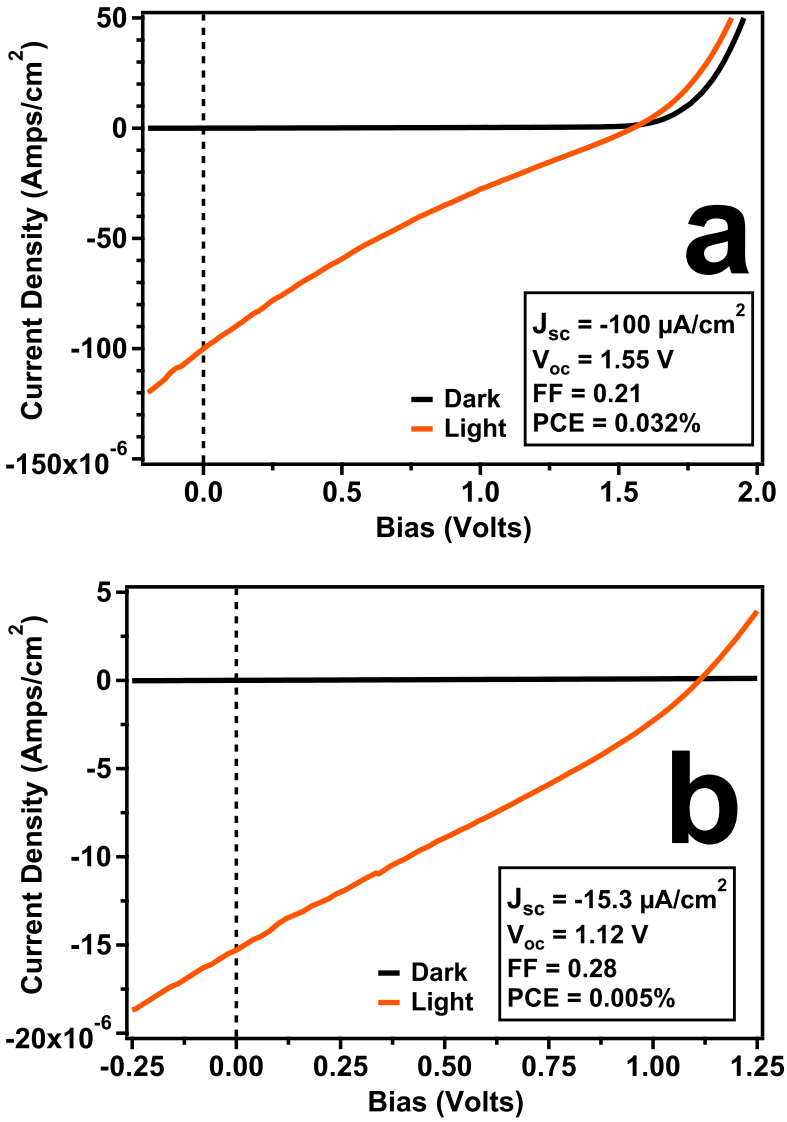

Figure 3.10: 'Bulk' Current density-voltage characteristics of an ITO/PEDOT:PSS/[PFB:F8BT]/Al PV device with the PFB:F8BT layer spin cast from a solution in (**a**) chloroform or (**b**) *p*-xylene.

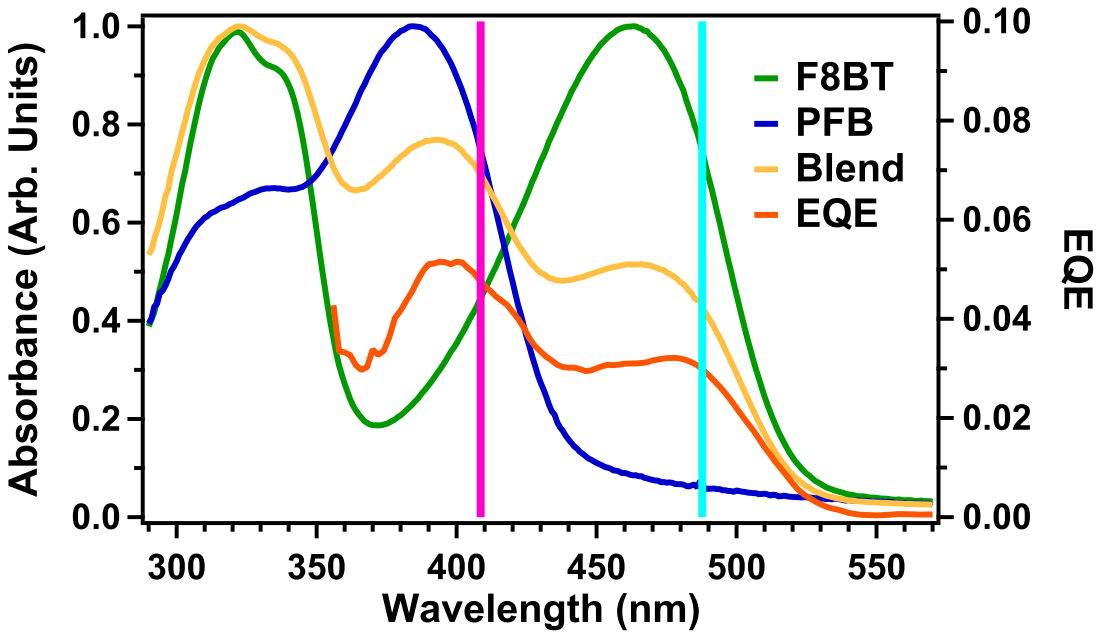

Figure 3.11: Shows the absorbance profiles from films of pure PFB (blue), pure F8BT (green), a blend of PFB:F8BT (tan) and the EQE (orange) of a PFB:F8BT PV device spin cast from chloroform. The two lines represent the illumination wavelengths used for scanning PC and PL images: 408 nm and 488 nm.

3.6 REFERENCES

1. Bredas, J.-L.; Durrant, J. R., Organic Photovoltaics. *Accounts of Chemical Research* **2009**, *42*, 1689-1690.
2. Brabec, C. J., Organic Photovoltaics: Technology and Market. *Solar Energy Materials and Solar Cells* **2004**, *83*, 273-292.
3. Brabec, C. J.; Gowrisanker, S.; Halls, J. J. M.; Laird, D.; Jia, S.; Williams, S. P., Polymer–Fullerene Bulk-Heterojunction Solar Cells. *Advanced Materials* **2010**, *22*, 3839-3856.
4. Lloyd, M. T.; Anthony, J. E.; Malliaras, G. G., Photovoltaics from Soluble Small Molecules. *Materials Today* **2007**, *10*, 34-41.
5. Walker, B.; Kim, C.; Nguyen, T. Q., Small Molecule Solution-Processed Bulk Heterojunction Solar Cells. *Chemistry of Materials* **2011**, *23*, 470-482.
6. McNeill, C. R.; Greenham, N. C., Conjugated-Polymer Blends for Optoelectronics. *Advanced Materials* **2009**, *21*, 3840-3850.
7. Yang, X.; Loos, J., Toward High-Performance Polymer Solar Cells: The Importance of Morphology Control. *Macromolecules* **2007**, *40*, 1353-1362.
8. Cai, W. Z.; Gong, X.; Cao, Y., Polymer Solar Cells: Recent Development and Possible Routes for Improvement in the Performance. *Solar Energy Materials and Solar Cells* **2010**, *94*, 114-127.
9. Groves, C.; Reid, O. G.; Ginger, D. S., Heterogeneity in Polymer Solar Cells: Local Morphology and Performance in Organic Photovoltaics Studied with Scanning Probe Microscopy. *Accounts of Chemical Research* **2010**, *43*, 612-620.
10. Giridharagopal, R.; Ginger, D. S., Characterizing Morphology in Bulk Heterojunction Organic Photovoltaic Systems. *Journal of Physical Chemistry Letters* **2010**, *1*, 1160-1169.
11. Kietzke, T.; Neher, D.; Kumke, M.; Montenegro, R.; Landfester, K.; Scherf, U., A Nanoparticle Approach to Control the Phase Separation in Polyfluorene Photovoltaic Devices. *Macromolecules* **2004**, *37*, 4882-4890.
12. Watkins, P. K.; Walker, A. B.; Verschoor, G. L. B., Dynamical Monte Carlo Modelling of Organic Solar Cells: The Dependence of Internal Quantum Efficiency on Morphology. *Nano Letters* **2005**, *5*, 1814-1818.
13. Snaith, H. J.; Arias, A. C.; Morteani, A. C.; Silva, C.; Friend, R. H., Charge Generation Kinetics and Transport Mechanisms in Blended Polyfluorene Photovoltaic Devices. *Nano Letters* **2002**, *2*, 1353-1357.
14. Kim, J.-S.; Ho, P. K. H.; Murphy, C. E.; Friend, R. H., Phase Separation in Polyfluorene-Based Conjugated Polymer Blends: Lateral and Vertical Analysis of Blend Spin-Cast Thin Films. *Macromolecules* **2004**, *37*, 2861-2871.

15. Shikler, R.; Chiesa, M.; Friend, R. H., Photovoltaic Performance and Morphology of Polyfluorene Blends: The Influence of Phase Separation Evolution. *Macromolecules* **2006**, *39*, 5393-5399.

16. Arias, A. C.; MacKenzie, J. D.; Stevenson, R.; Halls, J. J. M.; Inbasekaran, M.; Woo, E. P.; Richards, D.; Friend, R. H., Photovoltaic Performance and Morphology of Polyfluorene Blends: A Combined Microscopic and Photovoltaic Investigation. *Macromolecules* **2001**, *34*, 6005-6013.

17. Arias, A. C.; Corcoran, N.; Banach, M.; Friend, R. H.; MacKenzie, J. D.; Huck, W. T. S., Vertically Segregated Polymer-Blend Photovoltaic Thin-Film Structures through Surface-Mediated Solution Processing. *Applied Physics Letters* **2002**, *80*, 1695-1697.

18. Stevenson, R.; Arias, A. C.; Ramsdale, C.; MacKenzie, J. D.; Richards, D., Raman Microscopy Determination of Phase Composition in Polyfluorene Composites. *Applied Physics Letters* **2001**, *79*, 2178-2180.

19. McNeill, C. R.; Watts, B.; Thomsen, L.; Ade, H.; Greenham, N. C.; Dastoor, P. C., X-Ray Microscopy of Photovoltaic Polyfluorene Blends: Relating Nanomorphology to Device Performance. *Macromolecules* **2007**, *40*, 3263-3270.

20. Watts, B.; Schuettfort, T.; McNeill, C. R., Mapping of Domain Orientation and Molecular Order in Polycrystalline Semiconducting Polymer Films with Soft X-Ray Microscopy. *Advanced Functional Materials* **2011**, *21*, 1122-1131.

21. Swaraj, S.; Wang, C.; Yan, H. P.; Watts, B.; Jan, L. N.; McNeill, C. R.; Ade, H., Nanomorphology of Bulk Heterojunction Photovoltaic Thin Films Probed with Resonant Soft X-Ray Scattering. *Nano Letters* **2010**, *10*, 2863-2869.

22. McNeill, C. R.; Watts, B.; Swaraj, S.; Ade, H.; Thomsen, L.; Belcher, W.; Dastoor, P. C., Evolution of the Nanomorphology of Photovoltaic Polyfluorene Blends: Sub-100 nm Resolution with X-Ray Spectromicroscopy. *Nanotechnology* **2008**, *19*, 424015.

23. McNeill, C. R.; Watts, B.; Thomsen, L.; Belcher, W. J.; Greenham, N. C.; Dastoor, P. C.; Ade, H., Evolution of Laterally Phase-Separated Polyfluorene Blend Morphology Studied by X-Ray Spectromicroscopy. *Macromolecules* **2009**, *42*, 3347-3352.

24. Cadby, A.; Khalil, G.; Fox, A. M.; Lidzey, D. G., Mapping Exciton Quenching in Photovoltaic-Applicable Polymer Blends Using Time-Resolved Scanning near-Field Optical Microscopy. *Journal of Applied Physics* **2008**, *103*, 093715.

25. Chiesa, M.; Burgi, L.; Kim, J. S.; Shikler, R.; Friend, R. H.; Sirringhaus, H., Correlation between Surface Photovoltage and Blend Morphology in Polyfluorene-Based Photodiodes. *Nano Letters* **2005**, *5*, 559-563.

26. Coffey, D. C.; Ginger, D. S., Time-Resolved Electrostatic Force Microscopy of Polymer Solar Cells. *Nature Materials* **2006**, *5*, 735-740.

27. McNeill, C. R.; Frohne, H.; Holdsworth, J. L.; Dastoor, P. C., Near-Field Scanning Photocurrent Measurements of Polyfluorene Blend Devices: Directly Correlating Morphology with Current Generation. *Nano Letters* **2004**, *4*, 2503-2507.

28. Brenner, T. J. K.; McNeill, C. R., Spatially Resolved Spectroscopic Mapping of Photocurrent and Photoluminescence in Polymer Blend Photovoltaic Devices. *Journal of Physical Chemistry C* **2011**, *115*, 19364-19370.

29. Ostrowski, D. P.; Glaz, M. S.; Goodfellow, B. W.; Akhavan, V. A.; Panthani, M. G.; Korgel, B. A.; Vanden Bout, D. A., Mapping Spatial Heterogeneity in $Cu(In_{1-X}Ga_x)Se_2$ Nanocrystal-Based Photovoltaics with Scanning Photocurrent and Fluorescence Microscopy. *Small* **2010**, *6*, 2832-2836.

30. Huang, Y. S.; Westenhoff, S.; Avilov, I.; Sreearunothai, P.; Hodgkiss, J. M.; Deleener, C.; Friend, R. H.; Beljonne, D., Electronic Structures of Interfacial States Formed at Polymeric Semiconductor Heterojunctions. *Nature Materials* **2008**, *7*, 483-489.

31. Morteani, A. C.; Friend, R. H.; Silva, C., Exciton Trapping at Heterojunctions in Polymer Blends. *The Journal of Chemical Physics* **2005**, *122*, 244906.

32. Gao, J.; Grey, J. K., Spectroscopic Studies of Energy Transfer in Fluorene Co-Polymer Blend Nanoparticles. *Chemical Physical Letters* **2012**, *522*, 86-91.

33. Gupta, D.; Bag, M.; Narayan, K. S., Correlating Reduced Fill Factor in Polymer Solar Cells to Contact Effects. *Applied Physics Letters* **2008**, *92*, 093301.

34. Ramon, J. G. S.; Bittner, E. R., Exciton Regeneration Dynamics in Model Donor-Acceptor Polymer Heterojunctions. *Journal of Physical Chemistry B* **2006**, *110*, 21001-21009.

35. Reid, O. G.; Rayermann, G. E.; Coffey, D. C.; Ginger, D. S., Imaging Local Trap Formation in Conjugated Polymer Solar Cells: A Comparison of Time-Resolved Electrostatic Force Microscopy and Scanning Kelvin Probe Imaging. *The Journal of Physical Chemistry C* **2010**, *114*, 20672-20677.

36. McNeill, C. R.; Westenhoff, S.; Groves, C.; Friend, R. H.; Greenham, N. C., Influence of Nanoscale Phase Separation on the Charge Generation Dynamics and Photovoltaic Performance of Conjugated Polymer Blends: Balancing Charge Generation and Separation. *Journal of Physical Chemistry C* **2007**, *111*, 19153-19160.

Chapter 4: The Effects of Aggregation on Electronic and Optical Properties of Oligothiophene Particles

This chapter was reproduced in part from: Ostrowski, D. P.; Lytwak, L. A.; Mejia, M. L.; Stevenson, K. J.; Holliday, B. J.; Vanden Bout, D. A., The Effects of Aggregation on Electronic and Optical Properties of Oligothiophene Particles. *Acs Nano* **2012**, *6*, 5507-5513.

4.1 INTRODUCTION

New environmentally friendly energy sources are needed to meet the world's increasing demand for energy.[1] Solution processable photovoltaic materials show promise due to their low cost and scalability. However, the efficiency of these technologies remains well below the threshold required for commercial viability.[2] One factor affecting the photovoltaic properties of these materials is molecular morphology, in particular, the extent to which a molecule is electronically coupled (aggregated) to neighboring molecules.[3-5] Within a solution deposited thin film, the local morphology has been observed to vary substantially across the film, ranging from amorphous to highly aggregated.[6-11] Thus, design and control of optimized materials for efficient charge separation requires a fundamental understanding of the role that these morphological variations have on the optical and electronic properties of a material.

This work presents a study of how morphology, specifically molecular aggregation, affects optical and electronic properties. Different solution processing conditions were used to produce a variety of particle morphologies from the same conjugated small molecule. While this method produced numerous random and undistinguishable particles, there were also a number of consistently occurring particle shapes formed that were microscopically identifiable. These identifiable particles were

found to have similar optical and electronic properties as other particles of the same shape. However, distinct optical and electronic properties were observed for each different shape of particle studied. Typically, differences in molecular aggregation result in variations of the optical properties of the aggregates.[12,13] Herein, we show that molecular aggregation also affects the electronic properties of the molecules, in particular the LCP difference of the material as deduced from KPFM measurements. This variation of the electronic properties with morphology has clear implications for understanding the relative energy level changes of organic materials in solution-processed films used for bulk heterojunction photovoltaics.

4.2 Experimental Methods

Materials, Molecule and Particle Synthesis: The 3',3'''',4',4''''-tetraoctyl-2,2':5',2'':5'',2''':5''',2'''':5'''',2''''':-sexithiophene (O6T) particle fabrication included dissolving the molecule in a "good" solvent (one O6T is soluble in) at 5 mM concentration and injecting 100 μL of that solution into 10 mL of a stirred "bad" solvent (one O6T is only partially or not soluble in). The "good" solvents used include tetrahydrofuran (THF) and hexanes; the "bad" solvents used were nanopure water (H_2O), methanol (MeOH) and ethanol (EtOH). It is important that the solvent combination used be miscible. The particles from each solvent combination were isolated onto glass substrates through drop casting.

Fluorometer: The ensemble fluorescence images were collected with a SPEX Fluorolog 1 from Horiba Jobin Yvon that was controlled with LabVIEW. The excitation source was a 450 W Xenon lamp and two photomultiplier tube modules from Hamamatsu were used for detection of excitation and emission intensity.

Kelvin probe force microscopy (KPFM): A Veeco Dimension 3100 atomic force microscope (AFM) with a Nanoscope IV controller was used to collect both the topographic and surface potential images. The cantilevers used were from MikroMasch (CSC21/Cr-Au) and had a ~ 105 kHz resonant frequency and 2.0 N/m spring constant. Images were collected under dark conditions in attractive mode with a lift height around 40 nm and drive amplitude around 2.5 V. For setting the drive phase, a standard sample step edge of chromium to gold metal was utilized. Typically, a drive phase of ~40° was used. As the absolute voltage of the instrument would drift over time, the particles surface potential was measured relative to the glass substrate through a plot profile analysis as shown in Figure 4.7. Numerous measurements were collected from different particles of each shape and the reported surface potential differences were obtained by comparing the average of those values. The error in measurements were determined by error propogation of the noise in the instrument (~7.5 mV) with the standard deviation of the average potentials. The noise in the instrument was determined from the fluctuations in surface potential on a gold film.

Polarized Scanning Confocal Microscopy and Individual Particle Spectra. The confocal images were collected using a laboratory built microscope. The 408 nm excitation beam from a Coherent diode laser was focused onto the sample through a 60x Nikon objective with 0.7 numerical aperture. The fluorescence was collected through the same objective and isolated from the excitation with a dichroic mirror. A cube polarizing beam splitter was used to separate the fluorescence into two orthogonal polarizations that were imaged onto two Perkin Elmer avalanche photodiodes (APDs). The polarizations were defined as I_x and I_y, with X and Y defined in terms of the lab plane. The sample was scanned through a two-dimensional piezo stage from Queensgate Instruments that was controlled by LabVIEW. After scanning, the LabVIEW program could be used to move

the piezo stage to points of interest on the sample and the fluorescence rerouted from the APDs to an Acton spectrometer connected to a liquid nitrogen cooled charged coupled device (LN-CCD) from Princeton Instruments for collection of localized fluorescence spectra. The Gaussian fits to the spectra were performed with the Multipeak Fitting 2 analysis in Igor Pro.

4.3 RESULTS AND DISCUSSION

The structure of the oligothiophene molecule, 3',3'''',4',4''''-tetraoctyl-2,2':5',2'':5'',2''':5''',2'''':5'''',2''''':-sexithiophene (**O6T**), used in this work is shown in the inset of Figure 4.1. Particles of O6T were fabricated by injecting 100 μL of an O6T solution into 10 mL of a stirred 'bad' solvent (one O6T is only partially or not soluble in but that is miscible with the solvent used for the initial solution of O6T). As the O6T molecules are forced out of solution, O6T particles are formed. The resulting colloidal suspension of O6T particles can then be drop cast onto a substrate. Drop casting isolates the particles, allowing for optical and electronic studies of individual aggregates. Once isolated, the particles were studied with a variety of characterization techniques including: fluorescence spectroscopy, polarized scanning confocal microscopy, scanning electron microscopy (SEM), atomic force microscopy (AFM) and Kelvin probe force microscopy (KPFM).

The ensemble average emission spectrum (collected from a substrate containing a set of deposited particles from a particular solvent combination) were studied with a standard fluorometer. **Figure 4.1** shows these ensemble emission spectra from the particle sets prepared from different solvent combinations, along with the spectra from solvated O6T molecules in a tetrahydrofuran (THF) solution. The solvated emission spectrum of O6T shows a typical vibronic progression dominated by a single vibrational

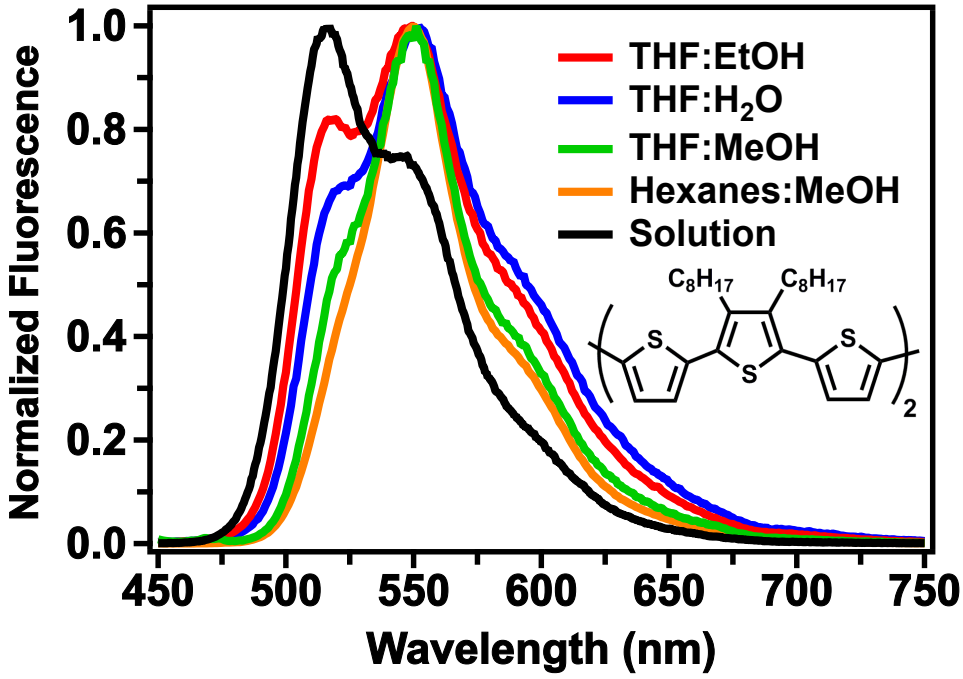

Figure 4.1: Emission spectra from the O6T particles that resulted from solution processing with different solvent combinations, along with the spectrum of O6T in THF solution. The solution spectrum was shifted 8.5 nm higher in wavelength to allow better comparison with the other spectra. The particles were drop cast onto a glass substrate for analysis. Inset shows structure of O6T molecule.

mode. The emission spectrum of the particle sets are similar, except with regard to the intensity of the highest energy 0-0 vibronic band, which varies in intensity as the solvent combination is changed. Theoretical work from Spano *et al*. has shown that the suppression of the 0-0 vibronic band in the emission spectrum to be a characteristic of weakly coupled H-aggregates, with the intensity of the 0-0 band in the emission spectrum being related to the extent of energetic disorder present in the aggregate.[13,14] Figure 4.1 demonstrates that the 0-0 band intensity varies between particles prepared from different solvent combinations, indicating that the nature of these aggregates could be tuned through solution processing.

For investigating the geometric heterogeneity and physical shape of the particles, AFM and SEM were used. For any given particle sample set from a particular solvent combination, a number of identifiable morphologies were observed along with other aggregates of less defined morphology. As the identifiable particles had a distinct and reproducible shape, it was possible to classify particular aggregates as belonging to one or another morphology and to correlate their optical and electronic properties as measured in two distinct experiments. The main morphologies targeted for this study were those formed from the THF/H_2O and THF/methanol ("good"/"bad") solvent combinations. These samples contained paticles that clustered into a small number of distinct shapes.

To study the optical properties of individual particles, polarized scanning confocal microscopy was used (see Experimental Methods section). As a substrate containing isolated particles was raster scanned over the focused 408 nm excitation light, two-dimensional emission images were collected point by point in two orthogonal emission polarizations. After collecting these images, the excitation source could be repositioned

onto a specific particle identified in the image to collect an emission spectrum of that individual particle. This allowed for correlation of particle shape and optical properties.

Figure 4.2a shows a fluorescence image collected from particles made from the THF/H_2O solvent combination. Two types of particles, identifiable by shape, were studied from this sample: the cylindrical particles called discoids and the oblong particles called ellipses. The two morphologies are identified in Figure 4.2a with green dots (discoid) and light blue dots (ellipse). Emission spectra were collected from a large number of discoid and ellipse particles to compare the two morphologies. Spectra collected from numerous particles of the same shape only showed slight spectral variations as shown in **Figure 4.2b**. Thus, different particles of the same shape possess similar morphological properties and molecular aggregation. Since nearly identical emission spectra are observed for similarly shaped particles, the spectra for numerous particles of each shape can be averaged together to better compare the two morphologies.

The averaged fluorescence spectra from both ellipse and discoid particles are shown in **Figure 4.2c**. The emission spectra for discoids and ellipses are similar except with regard to the intensity of the 0-0 vibronic band. There is the possibility that this is simply an effect of self-absorbance. However, the epi-illumination and collection geometry of the microscope allows for the same absorption and emission depths from each particle measured; thus, any self-absorbance would be consistent for all particles. Additionally, some particles have essentially no 0-0 vibronic band emission intensity, which could not result solely form self-absorption given this geometry. There is also a lack of consistent correlation between particle brightness (which is an indication of particle thickness) and decreased intensity of the 0-0 vibronic band. As a result this 0-0 vibronic band suppression is attributed to H-aggregate formation. For strongly coupled H-aggregates one would expect no fluorescence as the emission is completely symmetry

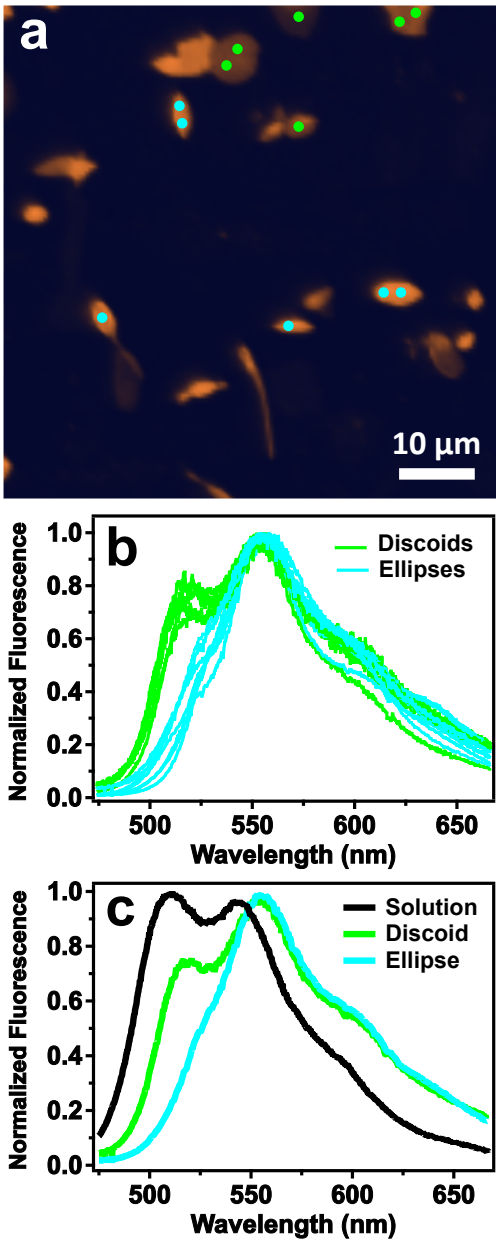

Figure 4.2: **a)** Total fluorescence image obtained from scanning confocal microscopy of the THF/H_2O solvent combination particles drop cast onto a glass substrate. The intensity scale ranges from 100 to 37,500 counts. **b)** Individual spectra of particles were collected at the blue points (ellipse) and green points (discoids) marked in image (a). **c)** Averaged spectra taken from numerous particles of elliptic (blue) or discoidal (green) morphology.

forbidden. However, for weakly coupled H-aggregates, only the 0-0 vibronic band is forbidden. This transition can be weakly allowed due to the breaking of symmetry in the aggregate by energetic disorder.[13,15] This disorder is characterized by two factors: the total energetic disorder (σ) and the spatial correlation of the disorder (β).[14,16] The intensity of the 0-0 emission peak is also affected by the free exciton bandwidth (W) and the Huang-Rhys factor (λ^2). From Figure 4.2c, it is observed that both the ellipse and the discoid spectra show some emission in the lowest energy 0-0 peak, but this emission is clearly suppressed when compared to the peak ratios of the O6T molecule isolated in a THF solution. To quantify the changes in the 0-0 vibronic band intensity, each emission spectrum was fit to a vibronic emission model consisting of a series of four Gaussian peaks separated by equal amounts of energy spacing (details and Figures of the fits are included in the Supporting Information). The ratios of 0-0 to 0-1 band intensity were quantified from the Gaussian fits to the experimental data, and were 0.29, 0.64 and 0.93 for the ellipse, discoid and solution spectra, respectively. The width of the peaks is reflective of the total energetic disorder (σ). Since the same peak width could be used to fit all the particle spectra, the value of the total energetic disorder (σ) is the same for all particles studied. Additionally, the Huang-Rhys factor (λ^2) is inherently the same for all the aggregates. The Huang-Rhys factor was determined to be 1.07 from the spectra of O6T molecules in solution. There are only two other parameters that can affect the intensity ratio of the 0-0 to 0-1 vibronic peaks: the values β and W.[14,16] To estimate possible variations in β, between the morphologies, an approximate value for W of 2000 cm^{-1} was used based on the results of previous studies.[15,17] The value of β, which can range between 0 and 1, was determined to be 0.37 and 0.65 for discoid and ellipse particles, respectively. From β the spatial correlation length (ℓ_0) in dimensionless units of lattice spacing is determined through the relationship $\ell_0 = -1/\ln(\beta)$.[16] The spatial

correlation length was found to range from 1.0 for discoid particles to 2.3 for ellipse particles. This shows in the ellipse particles the energetic disorder is correlated over a little more twice as many molecules as in the discoid particles.

One possible source for the energetic disorder in the particles is geometric irregularities in the molecular packing. To compare the molecular order within each particle, polarized confocal images were collected to examine the emission polarization of each particle. The fluorescence collected during scanning confocal microscopy imaging of the sample was sent through a polarizing beam splitter, allowing for collection of the two orthogonal emission polarizations. The fluorescence images of the horizontal and vertical polarizations, defined in terms of the lab plane, are shown in **Figure 4.3**. From these images, the fluorescence dichroism (FD) can be determined at each pixel by calculating the difference between the two images divided by the sum. The FD is an indication of how well aligned the transition dipole moments are for a given sample. Since these particles are composed of the same molecule, the FD is an indication of the geometric order of the molecules within the particle. The FD values can range from -1 to 1; an FD value of 0 indicates there is no distinct emission polarization and the sample is isotropic, which means there is no geometric alignment of the molecules. However, when FD is closer to -1 or 1, the sample has a distinct emission polarization and is well aligned. The FD values for the ellipse and discoid particles were 0.7 and 0.8, respectively. It is important to note that these are the minimum values possible, as no experimental methods were used to ensure that the emission particle polarization of a particle was completely aligned with one of the detectors. These high FD values indicate that the

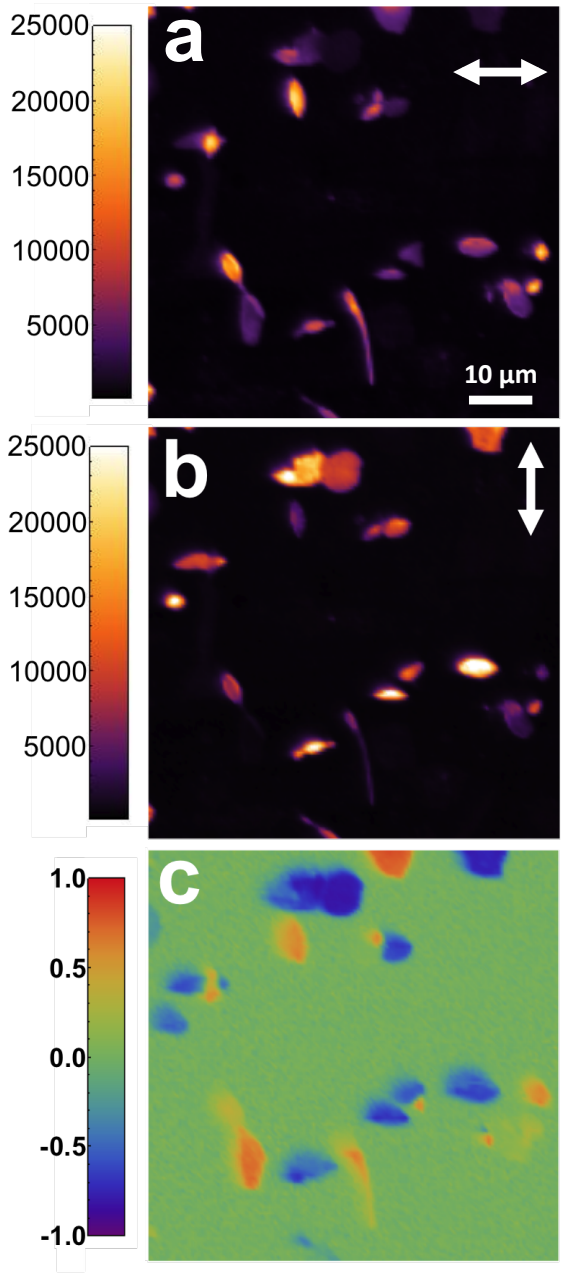

Figure 4.3: **a)** Horizontally and **b)** vertically polarized fluorescence images (defined in terms of the lab plan) obtained from polarized scanning confocal microscopy of the same particles shown in Figure 4.2. **c)** Fluorescence dichroism (FD) image calculated from the fluorescence images (a) and (b).

molecules within each particle are highly aligned and that the spectral differences must be a result of other factors such as intermolecular spacing.

While the different particles have shown a distinguishable variation in optical properties, the question remains as to what affect, if any, these morphological differences have on electronic properties. For electronic property characterization, each particle was studied with KPFM. KPFM is a non-contact, non-destructive electronic technique that simultaneously measures structural features as well as the local contact potential (LCP) difference between the scanning probe tip and the surface, which is closely related to intermolecular charge distribution.[18-27] First, the topographic AFM data are obtained and then the same line is rescanned at a specified lift height while the voltage difference between AFM tip and surface is determined at each point in the image. The bias voltage (V_{dc}) applied to the AFM tip is equal to the LCP difference between the tip and surface, and is determined through nullification of the capacitance force between tip and surface. The LCP maps were measured for oligothiophene particles deposited on an insulating substrate (glass) to eliminate any electronic contributions from the underlying substrate. A representative topography and LCP image is shown in **Figure 4.4**. Data analysis was performed on unaltered images (example shown in Supporting Information) but for lucidity both images in Figure 4.4 were linearly flattened. The LCP between ellipse and discoid particles was found to be 70 ± 30 mV. This LCP difference suggests that subtle morphological changes in particle shape and molecular packing are accompanied by a redistribution of charge within or between oligothiophene molecules. For instance, the local surface charge density (σ_{cd}), can be estimated by applying the Helmholtz equation for a parallel plate capacitor to the LCP measurement (more details in the Supporting Information).[28-32]

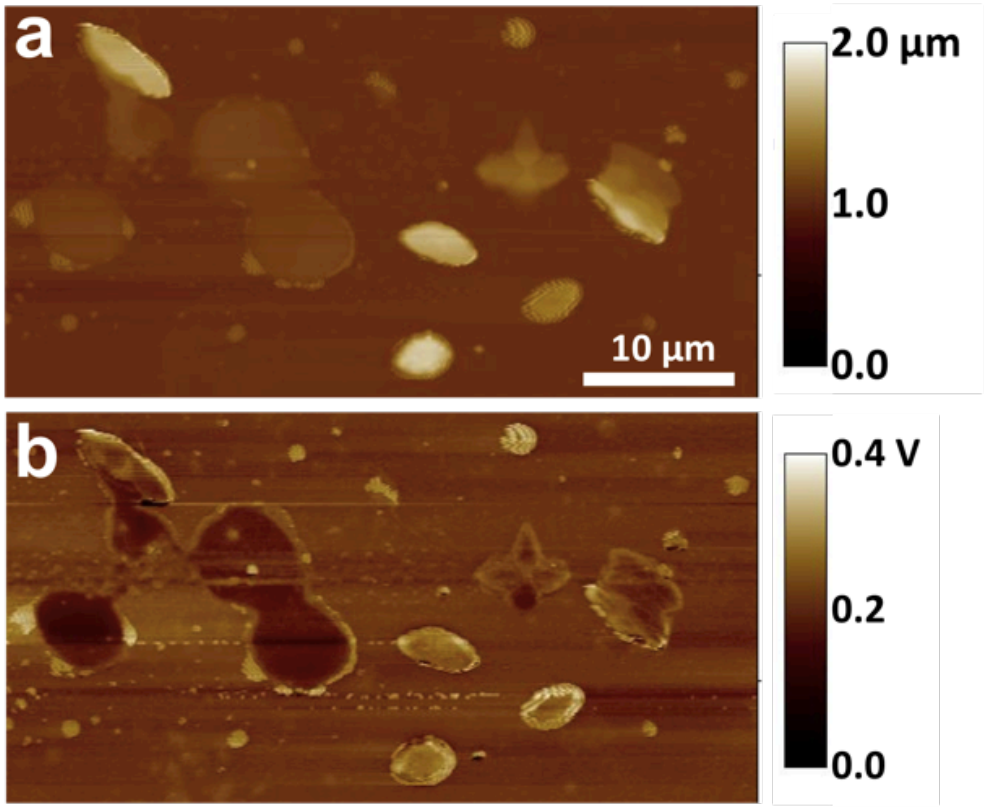

Figure 4.4: **a)** Topography and **b)** LCP images of ellipse and discoid particles on a glass substrate. Both images were linearly flattened for lucidity. Data analysis was performed on the unaltered images.

For this calculation the permittivity of O6T was estimated to be 3 from the value for un-substituted α-sexithiophene.[33] The higher surface potential for the ellipse particles corresponds to a higher σ_{cd} of ~0.012 charges per nm^2 above the discoid particles (assuming a capacitor thickness of 1 nm). Subtle changes in σ_{cd} (or intermolecular charge distribution) such as these could result from a variation in molecular packing density or molecular orientation between the different particles.

The variation in LCP suggests that the effective position of the highest occupied molecular orbital (HOMO) level of a molecule may shift at least 70 mV as result of small changes in molecular packing and aggregation. As this difference was measured between particles of similar aggregation, the difference between amorphous and highly aggregated molecules could be even larger. This result correlates to a varying energy landscape in these π-conjugated material thin films as a result of the local morphology, which has been previously suggested.[34] Changes in the relative energy levels of a molecule with morphology would have an effect on the charge separation efficiency at a donor-acceptor interface and ultimately on the efficiency of thin film photovoltaic devices.

To investigate if this trend (decreased 0-0 vibronic band emission intensity correlating to an increased LCP) holds for more than just these two morphologies, a third particle from a different solvent mixture was studied. Rectangular particles from the THF/methanol solvent combination were studied (see Supporting Information). The ratio of the 0-0 to 0-1 vibronic bands in the fluorescence spectrum of these particles was found to be 0.54, a slightly lower value than that of the discoid particles and in between the values for discoid and ellipse particles. The FD value again was high for these particles at 0.8, which shows that these particles also possess a high degree of molecular alignment. The LCP of the rectangular morphology particles falls in between the values for the ellipse and discoid particles but is closer to the discoid value than the ellipse, which is

expected based on the optical properties. The rectangular particle surface potential was ~ 23 ± 14 mV higher than the discoid particles and ~ 50 ± 30 mV lower than ellipse particles. These results show there is a correlated trend in the morphological effects on optical and electronic properties. More specifically, the suppression of the 0-0 vibronic band in the emission spectrum correlates to a decrease in the LCP of the particle, despite being composed of the same molecule.

4.4 CONCLUSION

This work demonstrates that morphology affects not only optical properties of a molecule, but also electronic properties. Here, numerous identifiable particles were produced through solution processing of the same small molecule, O6T. Once the particles were isolated on a substrate, their individual properties could be studied and correlated. Emission spectra of particles of different shape showed a range of intensities in the 0-0 vibronic band as a result of variations in molecular aggregation between particles. Through KPFM, differences in the local contact potential and therefore intermolecular charge distribution of distinct particles were measured. A direct correlation between optical and electronic properties of the different oligothiophene particle morphologies showed an observed trend; more well-defined aggregates (as signified by increased suppression of the 0-0 vibronic band intensity in emission spectra) also exhibit an increased LCP. This result signifies that these measurements are capable of detecting subtle variations in molecular packing density or molecular orientation between the different particle morphologies. From this result we can conclude that a thin film of organic materials composed of molecules with varying degrees of aggregation will have a correspondingly heterogeneous energy landscape. Given that the alignment of energy levels in a donor/acceptor system is known to affect charge separation, it is

expected that the differences in local aggregation will have substantial effects on charge separation at bimolecular heterojunctions in thin film photovoltaics. Further studies are currently underway to correlate the affect molecular aggregation has in donor/acceptor systems through controlling aggregated states to optimize charge separation.

4.5 SUPPORTING INFORMATION

From **Figure 4.5**, the rectangular particle emission spectrum shows a 0-0 vibronic band intensity in between that of the discoid and ellipse particles. The amount of suppression is closer to that of the discoid particles than it is to that of the ellipse particles.

The FD of ~0.8 for rectangular particles, **Figure 4.6**, shows that the molecular transition dipole moments within these particles are geometrically well-aligned. Thus the variable energetic disorder, gauged by the 0-0 vibronic band suppression in the different particle shapes, is not a result of geometric molecular order, as the FD values for all particle shapes (discoid, rectangular and ellipse) are similar.

The LCP values, **Figure 4.7**, for the rectangular morphology were found to be 23 ± 14 mV higher then the discoid particles and 50 ± 30 mV lower than ellipse particles. This is where the surface potential of the rectangular particles is expected to fall based on the optical properties, as the 0-0 vibronic band suppression is in between that of discoid and ellipse particles.

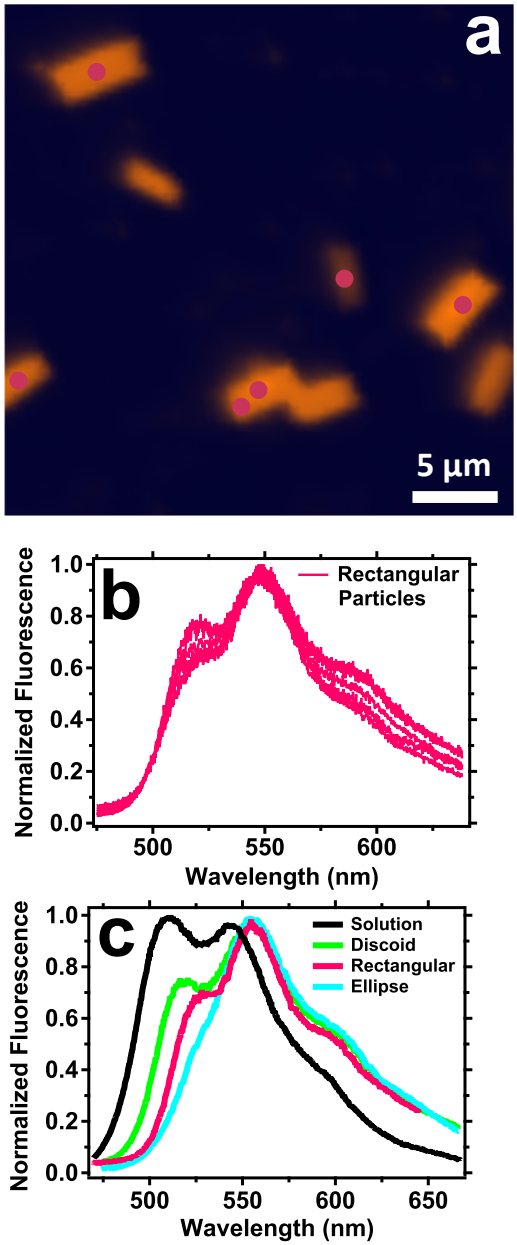

Figure 4.5: **a)** Total fluorescence image of rectangular particles found in the THF/MeOH solvent combination; intensity scale is from 0 to 55,000 counts. **b)** Emission spectra collected from the individual particles at the points marked in (a). **c)** Comparison of the averaged rectangular, discoid and ellipse particle emission spectra, along with spectra of O6T in THF solution.

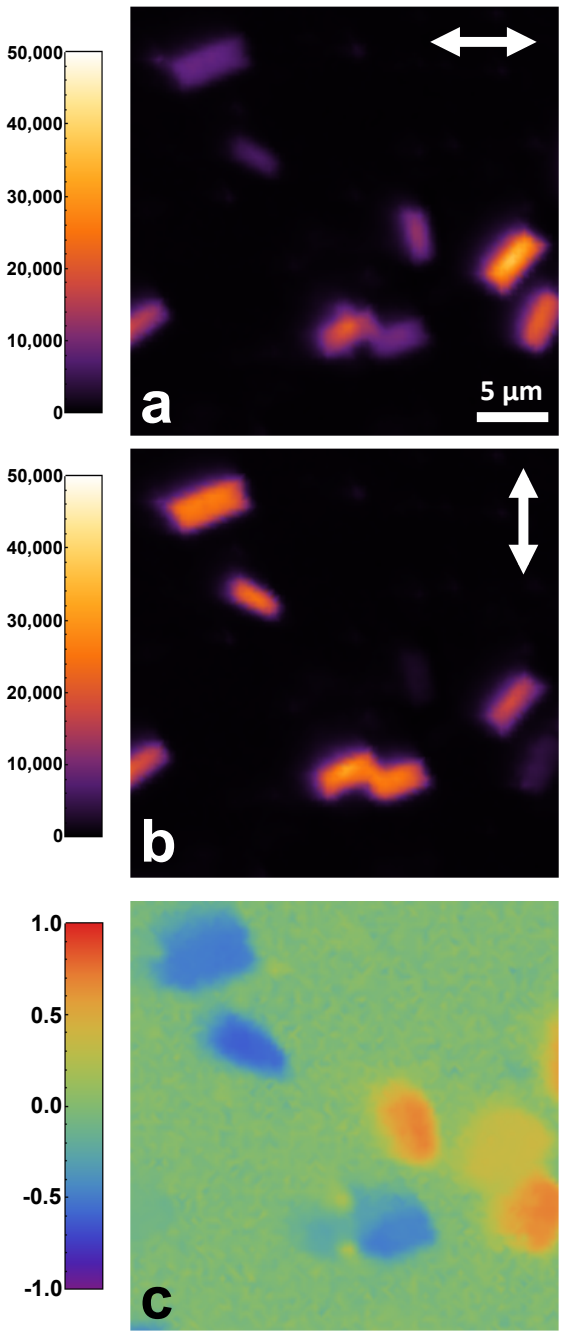

Figure 4.6: **a)** Horizontally and **b)** vertically polarized fluorescence images, defined in terms of the lab plane. **c)** The fluorescence dichroism (FD) image calculated from the fluorescence images shown in (a) and (b).

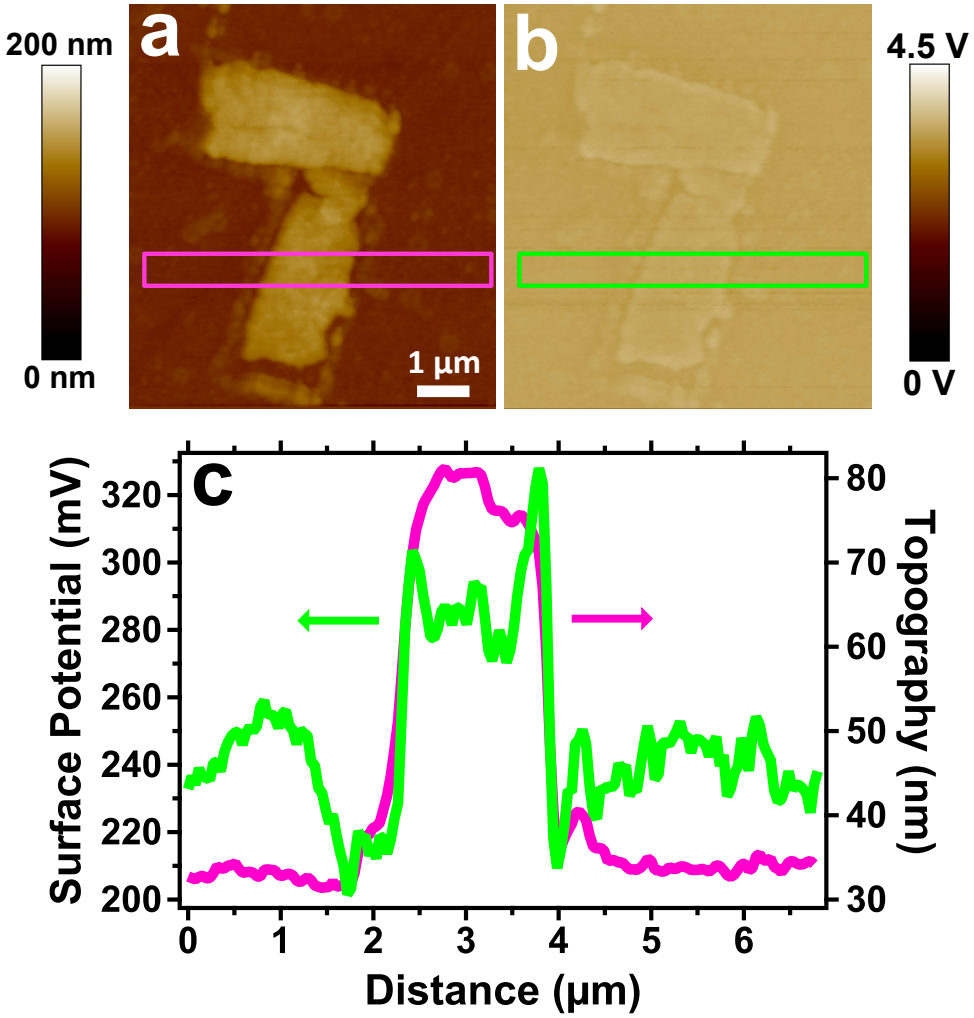

Figure 4.7: **a)** Topography and **b)** LCP images of the rectangular morphology from the THF/MeOH solvent combination deposited on glass. **c)** The cross-sectional plot from the region of interest marked in images (a) and (b).

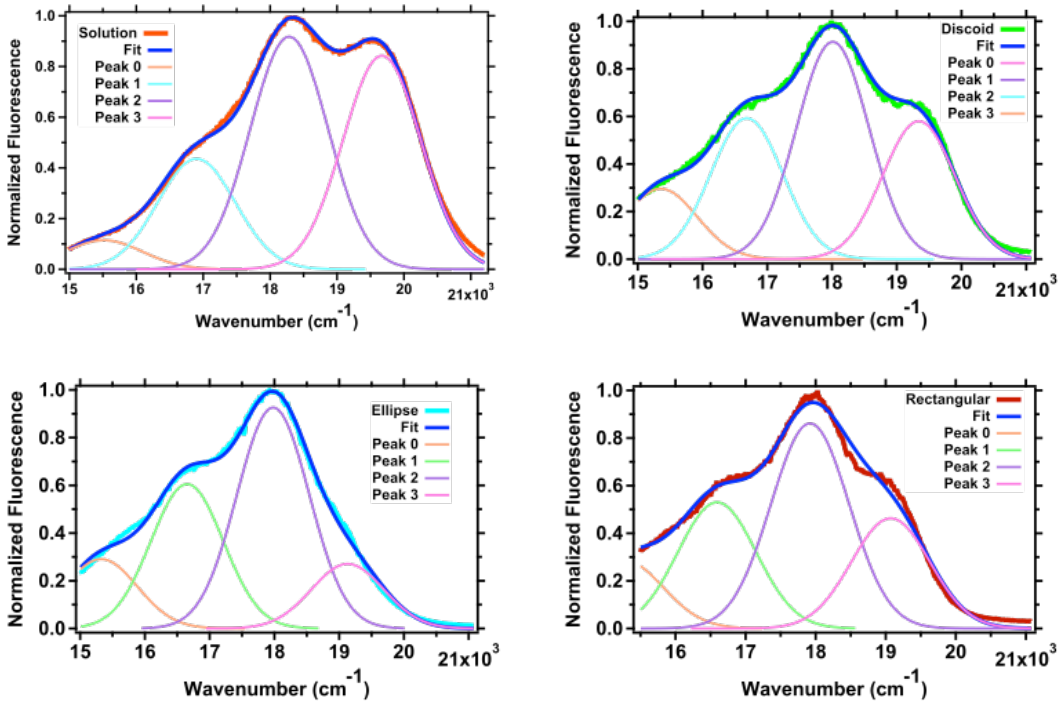

Figure 4.8: Overlay of each emission spectrum with the fit for the spectrum and the four Gaussian peaks composing each fit. **Top left)** O6T in THF solution. **Top right)** discoid particles. **Bottom left)** ellipse particles. **Bottom right)** rectangular particles.

As mentioned in the main text, to better quantify the extent to which the 0-0 vibronic band is suppressed, all the emission spectra were fit to a series of four Gaussian peaks (**Figure 4.8**). In order to remain consistent with a vibronic progression model where each vibrational level is energetically separated by the same amount, the peaks were kept at a constant energy spacing of 1328 cm^{-1}. The only exceptions to this were in the spectra where the 0-0 vibronic band was most suppressed, the ellipse and rectangular particle spectra. For these spectra, the spacing was constant at 1328 cm^{-1} as well, except the spacing between the 0-0 and 0-1 bands was decreased by shifting the 0-0 band to lower energy by 178 cm^{-1}. The solution spectrum in THF and the particle spectra from Figure 4.2c were all collected with the same instrumental setup so direct comparison between peak intensities are possible without instrument correction. For a consistent model, the widths of the Gaussian peaks were held constant for a particular spectrum. Also, all particle spectra were fit using the same peak width. The full-width-half-max and energetic spacing used to fit the solution spectra were 1365 cm^{-1} and 1385 cm^{-1}, respectively. This was slightly different than the full-width-half-max and energetic spacing used for the particle spectra fits of 1315 cm^{-1} and 1328 cm^{-1}, respectively. These differences are attributed to solvent effects.

Frank Spano has developed models for correlating the spectral properties of weakly coupled aggregates with energetic disorder and electronic coupling parameters.[13-16, 35, 36] For strongly coupled H-aggregates, the 0-0 vibronic band should be completely suppressed, as it is a symmetrically forbidden transition. However, when energetic disorder is added to the system, the symmetry is broken and the 0-0 vibronic band may be observed to a varying extent. It is also true that even in the presence of energetic disorder, if the disorder is spatially correlated enough, the 0-0 vibronic band may be completely suppressed as well.[14] The character β is the amount of spatial correlation to the energetic

disorder of the aggregate and can range from 0 to 1. The energetic disorder, denoted as σ, is estimated from the standard deviation multiplied by √2 of the Gaussian peaks used to fit the spectra. It is possible that some motional narrowing occurs in the peak width.[16] However, it holds that the σ from experimental spectra is the minimal possible value and is used in further calculations. Another parameter used in the models is the free exciton bandwidth (W). For determination of W from these models, the absorbance spectrum of the aggregate is needed.[13] However, due to the large extent of optical scattering off of the particle aggregates deposited on glass and no setup for localized absorbance measurements, absorbance spectra of the different particle shapes was unattainable. Thus, for these aggregates, W could not be calculated from this model. As an approximation of W for these O6T particles, a value of 2000 cm^{-1} was used. This was determined based on the results of previous studies. One study where W for a poly(3-hexylthiophene) (P3HT) film spun from chloroform was found to be ~ 968 cm^{-1} and another study where a 6 unit oligothiophene molecule was shown to have around double the electronic coupling value of the polymer at the same intermolecular distance of 4 angstroms.[15, 17]

Since the same value of σ was used to fit the spectra of all the targeted particle shapes, the suppression in the vibronic 0-0 band must be a result of variation in another parameter. As previously mentioned, the other parameters that affect the intensity of the 0-0 vibronic band are β and W.[14, 16] Here, we estimated the range β could vary between particles to obtain the experimentally determined intensity ratio of 0-0 to 0-1 bands for each particle shape. For this, the σ from the fit spectra was used along with Equations 3 and 4.[14]

$$I_{0\text{–}0} \approx \frac{(1-\beta)}{(1+\beta)} \frac{\sigma^2}{2e^{-1}W^2} \left(1 - \frac{0.24W}{\omega_0}\right)^2 \qquad (3)$$

$$I_{0-1} \approx e^{-1}(1-\frac{0.39W}{\omega_0})^2 \qquad (4)$$

I_{0-0} and I_{0-1} are the intensities of the 0-0 and 0-1 vibronic bands, respectively. The Haung-Rhys factor (λ^2) is calculated from the ratio of I_{0-0}/I_{0-1} from the solution (non-interacting molecular) spectrum, with $I_{0-0}/I_{0-1} = 1/\lambda^2$. Equations 1 and 2 apply only when the Huang-Rhys factor is 1; therefore, 1 has been inserted in place of λ^2 in the $e^{-\lambda^2}$ term of both equations shown above. The Huang-Rhys factor for this molecule was determined to be 1.07; for simplicity, the equations were used as written with an assumed value for the Huang-Rhys factor of 1, which was very close to the measured value. With a constant value for W (2000 cm^{-1}), β was determined to be 0.37, 0.44 and 0.65 for discoid, rectangular and ellipse particles, respectively. These β values were then used to calculate the spatial correlation length (ℓ_0), in dimensionless units, of lattice spacing, as determined through the relationship $\ell_0 = -1/\ln(\beta)$.[16] The spatial correlation lengths were determined to be 1.0, 1.2 and 2.3 for discoid, rectangular and ellipse particles, respectively.

In the original fits shown in Figure 4.8, the energy spacing between the peaks in the particle spectra was kept at a constant 1328 cm^{-1}. However, the energy spacing between the 0-0 and 0-1 vibronic peaks in the ellipse and rectangular particle spectra fits was decreased by 178 cm^{-1}. This shift in energy spacing could be the result of self-absorption of the particles, with more self-absorption resulting in decreased 0-0 band intensity. Reasons disproving self-absorption have been discussed in the main text. However, to test what effect, if any, this shift in energetic spacing would have on the 0-0/0-1 intensity ratio, the ellipse and rectangular particle spectra were refit with a constant energy spacing of 1328 cm^{-1}. These fits are shown in **Figure 4.9**; the fit purposefully misses the high energy edge of the spectra to exaggerate any possible effect from self-

absorption. From these modified fits, the 0-0/0-1 intensity ratio was determined to be 0.35 and 0.58 for ellipse and rectangular particles, respectively. These values are very similar to those deduced from the original fits shown in Figure 4.8: values of 0.29 for ellipse particles and 0.54 for rectangular particles. The discoid particle fit was not modified keeping the 0.64 value for the 0-0/0-1 intensity ratio. This shows that even with constant vibronic energy spacing in the fits of all the particles, the resulting 0-0/0-1 intensity ratios are essentially the same as the original fits discussed in the text, and more importantly the trend in the data is unaffected.

Surface charge density (σ_{cd}) calculation: The σ_{cd} was calculated from the LCP measurements and equation 5.[28, 29]

$$LCP = \frac{\sigma_{cd} d}{\epsilon_r \epsilon_0} \qquad (5)$$

where ϵ_r and ϵ_0 are the relative and vacuum permittivity respectively and d is the distance between the two plates of the theoretical capacitor. For this calculation ϵ_r was estimated to be 3 from the value for un-substituted α-sexithiophene.[33] The value for d was estimated to be 1 nm based on the approximate size of the O6T molecule.

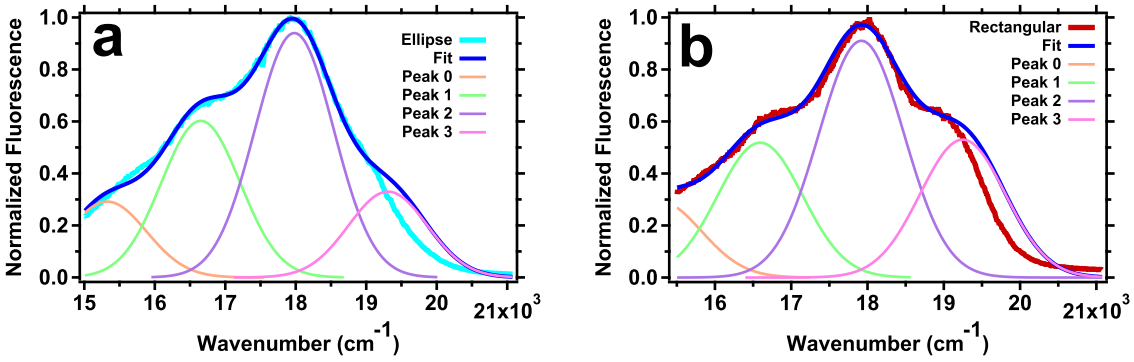

Figure 4.9: A modified version (from Figure 4.8) of the fit and four Gaussian peaks composing each fit to the emission spectra of **a)** ellipse and **b)** rectangular particles. These fits purposefully miss the high energy edge of the spectra to exaggerate any possible effect of self-absorption.

Acknowledgements for co-author contributions: Lytwak, Mejia and Prof. Holliday performed the synthesis of the O6T molecule and helped with the particle fabrication. Prof. Stevenson aided in the direction of the work and interpretation of the KPFM results. Prof. Vanden Bout also provided valuable direction, data interpretation and made extensive contribution to the optical modeling.

4.6 REFERENCES

1. Kamat, P. V., Meeting the Clean Energy Demand: Nanostructure Architectures for Solar Energy Conversion. *Journal of Physical Chemistry C* **2007**, *111*, 2834-2860.
2. Dennler, G.; Scharber, M. C.; Brabec, C. J., Polymer-Fullerene Bulk-Heterojunction Solar Cells. *Advanced Materials* **2009**, *21*, 1323-1338.
3. Bredas, J. L.; Norton, J. E.; Cornil, J.; Coropceanu, V., Molecular Understanding of Organic Solar Cells: The Challenges. *Accounts of Chemical Research* **2009**, *42*, 1691-1699.
4. Yang, X.; Loos, J., Toward High-Performance Polymer Solar Cells: The Importance of Morphology Control. *Macromolecules* **2007**, *40*, 1353-1362.
5. Roncali, J.; Leriche, P.; Cravino, A., From One to Three-Dimensional Organic Semiconductors: In Search of the Organic Silicon? *Advanced Materials* **2007**, *19*, 2045-2060.
6. Peet, J.; Heeger, A. J.; Bazan, G. C., "Plastic" Solar Cells: Self-Assembly of Bulk Heterojunction Nanomaterials by Spontaneous Phase Separation. *Accounts of Chemical Research* **2009**, *42*, 1700-1708.
7. Heremans, P.; Cheyns, D.; Rand, B. P., Strategies for Increasing the Efficiency of Heterojunction Organic Solar Cells: Material Selection and Device Architecture. *Accounts of Chemical Research* **2009**, *42*, 1740-1747.
8. Po, R.; Maggini, M.; Camaioni, N., Polymer Solar Cells: Recent Approaches and Achievements. *Journal of Physical Chemistry C* **2010**, *114*, 695-706.
9. Leclere, P.; Surin, M.; Brocorens, P.; Cavallini, M.; Biscarini, F.; Lazzaroni, R., Supramolecular Assembly of Conjugated Polymers: From Molecular Engineering to Solid-State Properties. *Materials Science and Engineering R* **2006**, *55*, 1-56.
10. Facchetti, A., Pi-Conjugated Polymers for Organic Electronics and Photovoltaic Cell Applications. *Chemical Materials* **2011**, *23*, 733-758.
11. Gearba, R. I.; Mills, T.; Morris, J.; Pindak, R.; Black, C. T.; Zhu, X. Y., Quantifying Interfacial Electric Fields and Local Crystallinity in Polymer-Fullerene Bulk-Heterojunction Solar Cells. *Advanced Functional Materials* **2011**, *21*, 2666-2673.
12. Sherwood, G. A.; Cheng, R.; Chacon-Madrid, K.; Smith, T. M.; Peteanu, L. A.; Wildeman, J., Chain Length and Substituent Effects on the Formation of Excimer-Like States in Nanoaggregates of CN-PPV Model Oligomers. *Journal of Physical Chemistry C* **2010**, *114*, 12078-12089.
13. Spano, F. C., The Spectral Signatures of Frenkel Polarons in H- and J-Aggregates. *Accounts of Chemical Research* **2010**, *43*, 429-439.

14. Spano, F. C.; Clark, J.; Silva, C.; Friend, R. H., Determining Exciton Coherence from the Photoluminescence Spectral Line Shape in Poly(3-Hexylthiophene) Thin Films. *Journal of Chemical Physics* **2009**, *130*, 074904.

15. Clark, J.; Chang, J. F.; Spano, F. C.; Friend, R. H.; Silva, C., Determining Exciton Bandwidth and Film Microstructure in Polythiophene Films Using Linear Absorption Spectroscopy. *Applied Physics Letters* **2009**, *94*, 163306.

16. Spano, F. C., Modeling Disorder in Polymer Aggregates: The Optical Spectroscopy of Regioregular Poly(3-hexylthiophene) Thin Films. *Journal of Chemical Physics* **2005**, *122*, 234701.

17. Gierschner, J.; Huang, Y. S.; Van Averbeke, B.; Cornil, J.; Friend, R. H.; Beljonne, D., Excitonic *Versus* Electronic Couplings in Molecular Assemblies: The Importance of Non-Nearest Neighbor Interactions. *Journal of Chemical Physics* **2009**, *130*, 044105.

18. Mohn, F.; Gross, L.; Moll, N.; Meyer, G., Imaging the Charge Distribution within a Single Molecule. *Nature Nanotechnology* **2012**, DOI: 10.1038/NNANO.2012.20.

19. Liscio, A.; Palermo, V.; Samori, P., Probing Local Surface Potential of Quasi-One-Dimensional Systems: A KPFM Study of P3HT Nanofibers. *Advanced Functional Materials* **2008**, *18*, 907-914.

20. Liscio, A.; Palermo, V.; Fenwick, O.; Braun, S.; Mullen, K.; Fahlman, M.; Cacialli, F.; Samori, P., Local Surface Potential of Pi-Conjugated Nanostructures by Kelvin Probe Force Microscopy: Effect of the Sampling Depth. *Small* **2011**, *7*, 634-639.

21. Palermo, V.; Palma, M.; Samori, P., Electronic Characterization of Organic Thin Films by Kelvin Probe Force Microscopy. *Advanced Materials* **2006**, *18*, 145-164.

22. Liscio, A.; Palermo, V.; Samori, P., Nanoscale Quantitative Measurement of the Potential of Charged Nanostructures by Electrostatic and Kelvin Probe Force Microscopy: Unraveling Electronic Processes in Complex Materials. *Accounts of Chemical Research* **2010**, *43*, 541-550.

23. Palermo, V.; Liscio, A.; Palma, M.; Surin, M.; Lazzaroni, R.; Samori, P., Exploring Nanoscale Electrical and Electronic Properties of Organic and Polymeric Functional Materials by Atomic Force Microscopy Based Approaches. *Chemical Communications* **2007**, 3326-3337.

24. Melitz, W.; Shen, J.; Kummel, A. C.; Lee, S., Kelvin Probe Force Microscopy and Its Application. *Surface Science Reports* **2011**, *66*, 1-27.

25. Groves, C.; Reid, O. G.; Ginger, D. S., Heterogeneity in Polymer Solar Cells: Local Morphology and Performance in Organic Photovoltaics Studied with Scanning Probe Microscopy. *Accounts of Chemical Research* **2010**, *43*, 612-620.

26. Barth, C.; Foster, A. S.; Henry, C. R.; Shluger, A. L., Recent Trends in Surface Characterization and Chemistry with High-Resolution Scanning Force Methods. *Advanced Materials* **2011**, *23*, 477-501.

27. Puntambekar, K.; Dong, J. P.; Haugstad, G.; Frisbie, C. D., Structural and Electrostatic Complexity at a Pentacene/Insulator Interface. *Advanced Functional Materials* **2006**, *16*, 879-884.

28. Taylor, D. M.; Bayes, G. F., Calculating the Surface-Potential of Unionized Monolayers. *Physical Review E* **1994**, *49*, 1439-1449.

29. Maldonado, S.; Smith, T. J.; Williams, R. D.; Morin, S.; Barton, E.; Stevenson, K. J., Surface Modification of Indium Tin Oxide *Via* Electrochemical Reduction of Aryldiazonium Cations. *Langmuir* **2006**, *22*, 2884-2891.

30. Zuppiroli, L.; Si-Ahmed, L.; Kamaras, K.; Nuesch, F.; Bussac, M. N.; Ades, D.; Siove, A.; Moons, E.; Gratzel, M., Self-Assembled Monolayers as Interfaces for Organic Opto-Electronic Devices. *Eur. Phys. J. B* **1999**, *11*, 505-512.

31. Sugimura, H.; Hayashi, K.; Saito, N.; Nakagiri, N.; Takai, O., Surface Potential Microscopy for Organized Molecular Systems. *Applied Surface Science* **2002**, *188*, 403-410.

32. Fujihira, M., Kelvin Probe Force Microscopy of Molecular Surfaces. *Annual Review of Materials Science* **1999**, *29*, 353-380.

33. Aruta, C.; D'Angelo, P.; Barra, M.; Ausanio, G.; Cassinese, A., Improved Structural Ordering in Sexithiophene Thick Films Grown on Single Crystal Oxide Substrates. *Applied Physics A: Materials Science and Processing* **2009**, *97*, 387-394.

34. Kaake, L. G.; Barbara, P. F.; Zhu, X. Y., Intrinsic Charge Trapping in Organic and Polymeric Semiconductors: A Physical Chemistry Perspective. *Journal of Physical Chemistry Letters* **2010**, *1*, 628-635.

35. Spano, F. C.; Yamagata, H., Vibronic Coupling in J-Aggregates and Beyond: A Direct Means of Determining the Exciton Coherence Length from the Photoluminescence Spectrum. *Journal of Physical Chemistry B* **2011**, *115*, 5133-5143.

36. Clark, J.; Silva, C.; Friend, R. H.; Spano, F. C., Role of Intermolecular Coupling in the Photophysics of Disordered Organic Semiconductors: Aggregate Emission in Regioregular Polythiophene. *Physical Review Letters* **2007**, *98*, 206406.

Chapter 5: Future Work and Directions for Research

5.1 Dissertation Summary

The goal of the research presented in this dissertation was to develop methods for characterizing the effects of local morphological heterogeneity on solution processable PV materials and through these methods, provide a better understanding of the influence morphology has on electronic and optical properties. Chapters 2 and 3 present microscopy measurements on functional PV devices, with the localization of the measurement resulting from only illuminating a small region of the device at a time. Through correlation of local PC generation with optical properties, a valuable understanding into the effects of morphological heterogenetiy on device performance was gained. This understanding yields feedback for device fabrication by providing a target morphology for maximum PV performance. Chapter 4 presents an approach focused on selecting a morphological parameter known to vary in solution processable PV materials and creating a sample set with a tunable variation of that parameter for study. The parameter of interest was the extent of molecular aggregation (or intermolecular coupling) through a sample set of particles created from solution processing of the same oligothiophene molecule. The particles, identifiable by shape, could then be studied with various optical and electronic techniques. The studies found a correlation of less energetic disorder with an increased LCP, meaning as energetic disorder in the molecular system is decreased the effective work function of the material is decreased by up to 70 meV (between particles of moderate to low energetic disorder). This effect is likely to have substantial implications for charge separation efficiency at the donor/acceptor interface, as the driving force for charge separation is the energetic differences between the respective HOMO or LUMO (lowest occupied molecular orbital) levels of the donor and acceptor. The electronic and optical variations result only from the morphology

present in the different particles as they are all composed of the same molecule, illustrating the significant effects morphology can have on properties. Also, through the experimental techniques used to study the particles, the morphological effects were quantified. The presented work has demonstrated the valuable understanding gained into morphological effects on PV properties from use of these novel characterization methodologies. In addition, these techniques are not limited to the material systems studied here but can be more universally applied to better characterize heterogeneity in other PV relevant systems. There are also extensions of these techniques, discussed in this chapter, which would provide an even more comprehensive understanding of heterogeneity in PV relevant materials.

5.2 MAPPING PV PERFORMANCE HETEROGENEITY UNDER AN APPLIED BIAS VOLTAGE

The scanning PC and PL microscopy setup described here was primarily used to map the device properties under zero applied bias. The LVPC measurements collected on both the CIGS nanocrystal and PFB:F8BT systems studied showed the only significant difference in diode characteristics to be the magnitude of PC generated. This result suggested that a comprehensive view of the PV performance heterogeneity in these material systems is gained through the images of PC generation with zero bias voltage. However, while the LVPC measurements were valuable, they only allowed for study of the bias dependent properties of a few specific regions within each collected image. Also, in other materials systems, substantial variations in the local diode characteristics have been observed.[1] A more comprehensive picture of the bias dependent PV variations and optical properties would be obtained from collecting images under an applied bias, or collecting an image of the induced photovoltage variations.

An insightful parameter in PV characterization is the V_{oc}, the applied bias at zero PC. The V_{oc} in the 'bulk' characterization I-V measurement is the applied bias at which the sum of the dark current and photocurrent is zero. As the experimental setup used for scanning PC and PL microscopy uses an optical chopper and lock-in amplifier to improve the signal to noise ratio, the dark current is filtered out of the measurement and only the magnitude of the PC is measured, the amplitude of the oscillating wave from light off (dark current) to light on (photocurrent). Thus, as described in chapter 2, in the LVPC measurement scheme only the PC is measured with applied bias voltage. Thus, the voltage at zero PC measurement in the LVPC is the point at which the dark current is equal to the photocurrent, and not the V_{oc} in the traditional sense. However, the value measured in the LVPC measurement would approach the V_{oc} in the limit of small to negligible dark current. Regardless, mapping of the local induced photovoltage would yield valuable information on the electronic variations across the device. This information may yield insight into charge recombination mechanisms and the energy variations of the CT state in donor/acceptor systems.[2,3]

Experimentally, for the I-V sweep (and the LVPC measurement) the source voltage (applied bias) is scanned and the current is measured. In a similar manner the measurement could be modified to source current and monitor the local photo-induced voltage. An alternative route may be that the input resistance on the lock-in amplifier is sufficient to prevent the current flow and measure the induced photovoltage directly. Sourcing zero current and mapping the induced photovoltage produced with local illumination at each step would create image maps of variations in the voltage at zero PC. As the dark current is minimal the voltage with the light off should be close to zero and then with the light on the voltage would be representative of the local V_{oc}. Thus, using this approach it may be possible to measure image maps that allow correlation of relative

changes in V_{oc}, PC and PL. Furthermore, through collecting multiple images each at a slightly different applied bias, the LVPC measurement could be compiled at each point in an image. This would yield a comprehensive view of any variation present in the local diode characteristics.

This experiment, however, would be more difficult to interpret than the PC image maps. With PC imaging the path the charge carriers take to get out of the device is not significant to the resolution of the images. However, with a local measurement of induced photovoltage, this process is more complicated as the extracted charge carriers end up at the same conductive electrodes and thus would have a similar potential difference. Any leakage current in the regions surrounding the illuminated region may have a substantial effect on the measurement as a result the resolution may be more determined by surrounding leakage current effects than the region of the device being illuminated. As with all these techniques it is a question of the resolution of the measurement versus the length scale of the heterogeneity in PV properties.

5.3 Optical extensions to the Scanning PC and PL Microscopy Technique

In the presented work, PC generation was simultaneously collected with PL properties (either total PL or a PL spectrum). The PL was essential in determining some of the chemical composition variations that influenced the amount of PC generation. In the case of the CIGS nanocrystal based PV, the PL allowed for identification of CdS aggregates that were having a detrimental effect on PC generation. While in the bulk heterojunction PFB:F8BT based PV device, the PL allowed for qualitative characterization of the local chemical composition variations along with the intensity fluctuations across the device of particular charge recombination mechanisms such as exciplex-PL. Thus, this work has demonstrated that PL measurements yield valuable

insight into material identification, qualitative chemical composition variations, and the extent of local radiative charge recombination mechanisms occurring across the PV device. However, the optical collection capabilities of this setup could be expanded to further characterize the heterogeneity through measurement of many other spectroscopic properties including: electroluminescence (EL),[4-7] Raman spectroscopy,[8-11] polarized PL,[12,13] time resolved PL[14-17] along with absorbance and reflectivity measurements. In the following text the beneficial details to electroluminescence (EL) and Raman spectroscopy measurements are presented.

5.3a Electroluminescence Measurements

Electroluminescence (EL) measurement involves injection of charge carriers from the electrodes into the PV device through an applied voltage, some of the charge carriers will meet in the device and radiatively recombine, the emitted light is the EL. This is the operation mode of a light emitting diode (LED), the reverse mechanism of the PV device in which charge carriers are generated through light absorption and extracted from the device at the electrodes. The intensity variations in EL across the PV device could be mapped in a small amount of time through a wide field microscopy image, or local EL spectra could be obtained from the scanning confocal microscope setup used in optical collection mode.

Recently, EL intensity has been shown to correlate with numerous factors affecting the PV performance along with certain PV characteristics: V_{oc}, J_{sc}, electrode contact characterization, fabrication defects and charge transfer (CT) state radiative recombination.[2-7,18-20] The energy of the peak in EL intensity resulting from CT state radiative recombination has shown direct correlation with the V_{oc} measured in the same PV device.[3] Thus, collection of local EL spectra may actually be an alternative method to

mapping heterogeneity in V_{oc} than the local induced photovoltage method described previously. There has also been work correlating the intensity of the EL with the J_{sc} measured locally with LBIC.[19] The voltage dependence of EL has been used to study the radiative recombination mechanisms in donor/acceptor PV devices.[2] Images of EL in these systems also would yield information into variation in the radiative recombination efficiency and, more importantly, any difference in the energy of emission from the CT-state across the film.[4]

Experimentally, this would involve applying a bias and monitoring the emitted light intensity. With wide-field microscopy, an image of the EL intensity variations across the device is collected simultaneously. Wavelength dependent intensity measurements in the wide-field mode would require use of optical filters to narrow the wavelength range of collection. With scanning confocal microscopy operated in collection mode, EL spectra at each point in an image could be collected from a film for more extensive EL information. The difficulties with EL measurements will result from likely low signal to noise ratios and the fact that in many materials systems the EL emission is in the infrared, which would require optical detection sensors more sensitive to infrared radiation than the silicon detectors currently used in the experimental setup.

5.3b Raman Spectroscopy

The PL measurements presented in this work provided information towards radiative recombination effects, chemical identification, and qualitative chemical composition variations across the device. The compositional variations determined from PL are only qualitative because the intensity of the PL is affected by many properties. The main factors affecting PL are the PL quantum yield and light absorption variations (resulting from both local concentration and the absorbance profile of the sample),

neither of these properties were measured directly in these experiments. Further complications result from the charge extraction that the PV device is designed for, the possibility of FRET (fluorescence resonance energy transfer) from one material to the other, and the possibility of other radiative charge recombination mechanisms such as exciplex PL.

One spectroscopic technique that is capable of providing a more straightforward quantitative analysis without these types of complications is that of Raman spectroscopy. Ramam microscopy measurements have been used to determine quantitative chemical composition the extent of molecular order present locally.[8-11] Through these types of experiments in resonance Raman mode, PC can be simultaneously studied with variations in resonance Raman intensities.[9,10]

Experimentally this would involve moving the diffraction grating in the spectrometer to view the wavelength range of the Raman signal, which is dependent on the illumination wavelength. The Raman measurements could be done simultaneously with PC image maps in resonance Raman mode, or could be done separately in just Raman mode. As Raman is a scattering technique that does not require light absorption a wide range of illumination wavelengths are possible to gather the same information. One difficulty of this measurement may be the signal to noise ratio, as Raman intensity is generally much less intense than PL intensity. Initially Raman measurements from regions of interest in the PC image map could be obtained followed by imaging of the Raman intensity fluctuations.

5.4 Quantitative Measurement of the Effect of Molecular Aggregation on Charge Separation at a Donor/Acceptor Heterojunction

The decrease in effective work function of the same molecule as a result of morphology (presented in chapter 4), would likely have a substantial effect on charge

separation at the donor/acceptor interface.[13] Thus, it would be interesting to quantify the influence the effective work function change between the particles has on charge separation. This measurement could be done with KPFM, similar to an experiment described in the literature.[21]

For this measurement a sample consisting of both isolated and overlapping donor and acceptor particles is needed. The oligothiophene particles (donor) are already isolated and scattered across the glass substrate. Thermal deposition of a common acceptor material (C_{60}) onto glass has resulted in island growth of this material (**Figure 5.1**). This was achieved through a low deposition rate, around 0.1 Angstroms per second, and stopping the deposition before a complete monolayer of material is formed. The island size varies with the amount of material deposited. Thus, through thermal deposition of C_{60} onto the substrate containing the oligothiophene particles the desired sample is obtained. The measurement involves KPFM of the LCP under dark and illuminated conditions. Through observation of the change from dark to light in LCP of the isolated particles compared to the change for overlapping donor and acceptor particles, the number of charges transferred between donor and acceptor particle is determined.[21] These measurements would allow for quantitative determination of the difference in charge separation efficiency between the C_{60} and oligothiophene particles of moderate to low energetic disorder. These data would show the impact that a 70 meV difference in work function has on charge separation. The result would be valuable in understanding the effect that morphological variations can have on local charge separation in donor/acceptor PV systems along with information into the energetic driving force needed for charge separation to occur.

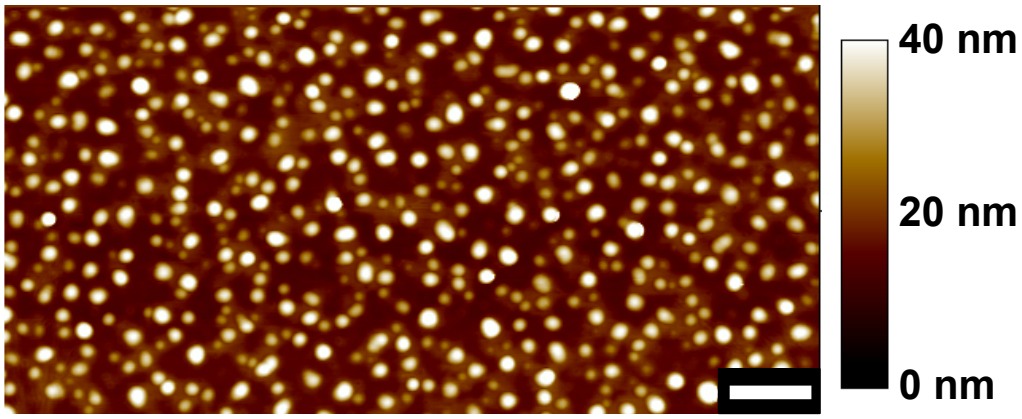

Figure 5.1: An AFM topography image of islands of C_{60} (acceptor material) on glass. The islands were grown by thermal deposition in a vacuum chamber located in a nitrogen filled glove box. The diameter of the islands is controllable through the amount of C_{60} deposited. Scale bar is 0.5 microns.

5.5 CONCLUDING REMARK:

The value of the methodologies presented in determining the morphological effects on PV performance in solution processable PV materials was demonstrated. These techniques are not specific to the material systems studied here but could also be applied more universally to a wide range of PV devices and material systems. The information gained provides direct insight into the factors affecting PV performance, which provides a guide for fabrication of improved efficiency PV devices. Thus, this enhanced characterization aids in developing a useful, environmentally friendly energy source for future generations.

5.5 REFERENCES

1. Coffey, D. C.; Reid, O. G.; Rodovsky, D. B.; Bartholomew, G. P.; Ginger, D. S., Mapping Local Photocurrents in Polymer/Fullerene Solar Cells with Photoconductive Atomic Force Microscopy. *Nano Letters* **2007**, *7*, 738-744.
2. Wetzelaer, G.-J. A. H.; Kuik, M.; Blom, P. W. M., Identifying the Nature of Charge Recombination in Organic Solar Cells from Charge-Transfer State Electroluminescence. *Advanced Energy Materials* **2012**, DOI: 10.1002/aenm.201200009.
3. Tvingstedt, K.; Vandewal, K.; Gadisa, A.; Zhang, F.; Manca, J.; Inganäs, O., Electroluminescence from Charge Transfer States in Polymer Solar Cells. *Journal of American Chemical Society* **2009**, *131*, 11819-11824.
4. Hoyer, U.; Wagner, M.; Swonke, T.; Bachmann, J.; Auer, R.; Osvet, A.; Brabec, C. J., Electroluminescence Imaging of Organic Photovoltaic Modules. *Applied Physics Letters* **2010**, *97*, 233303.
5. Johnston, S.; Repins, I.; Call, N.; Sundaramoorthy, R.; Jones, K. M.; To, B. In *Applications of Imaging Techniques to Si, Cu(In,Ga)Se_2, and CdTe and Correlation to Solar Cell Parameters*, Photovoltaic Specialists Conference (PVSC), 2010 35th IEEE, 20-25 June 2010; 2010; pp 001727-001732.
6. Hallermann, M.; Haneder, S.; Da Como, E., Charge-Transfer States in Conjugated Polymer/Fullerene Blends: Below-Gap Weakly Bound Excitons for Polymer Photovoltaics. *Applied Physics Letters* **2008**, *93*, 053307-3.
7. Seeland, M.; Rosch, R.; Hoppe, H., Quantitative Analysis of Electroluminescence Images from Polymer Solar Cells. *Journal of Applied Physics* **2012**, *111*, 024505-5.

8. Gao, Y. Q.; Grey, J. K., Resonance Chemical Imaging of Polythiophene/Fullerene Photovoltaic Thin Films: Mapping Morphology-Dependent Aggregated and Unaggregated C=C Species. *Jounal of the American Chemical Society* **2009**, *131*, 9654-9662.

9. Gao, Y. Q.; Martin, T. P.; Niles, E. T.; Wise, A. J.; Thomas, A. K.; Grey, J. K., Understanding Morphology-Dependent Polymer Aggregation Properties and Photocurrent Generation in Polythiophene/Fullerene Solar Cells of Variable Compositions. *Journal of Physical Chemistry C* **2010**, *114*, 15121-15128.

10. Gao, Y. Q.; Martin, T. P.; Thomas, A. K.; Grey, J. K., Resonance Raman Spectroscopic- and Photocurrent Imaging of Polythiophene/Fullerene Solar Cells. *Journal of Physical Chemistry Letters* **2010**, *1*, 178-182.

11. Shikler, R.; Chiesa, M.; Friend, R. H., Photovoltaic Performance and Morphology of Polyfluorene Blends: The Influence of Phase Separation Evolution. *Macromolecules* **2006**, *39*, 5393-5399.

12. Teetsov, J.; Vanden Bout, D. A., Near-Field Scanning Optical Microscopy Studies of Nanoscale Order in Thermally Annealed Films of Poly(9,9-Diakylfluorene). *Langmuir* **2002**, *18*, 897-903.

13. Ostrowski, D. P.; Lytwak, L. A.; Mejia, M. L.; Stevenson, K. J.; Holliday, B. J.; Vanden Bout, D. A., The Effects of Aggregation on Electronic and Optical Properties of Oligothiophene Particles. *Acs Nano* **2012**, *6*, 5507-5513.

14. Cadby, A.; Khalil, G.; Fox, A. M.; Lidzey, D. G., Mapping Exciton Quenching in Photovoltaic-Applicable Polymer Blends Using Time-Resolved Scanning Near-Field Optical Microscopy. *Journal of Applied Physics* **2008**, *103*, 093715.

15. Cadby, A. J.; Dean, R.; Elliott, C.; Jones, R. A. L.; Fox, A. M.; Lidzey, D. G., Imaging the Fluorescence Decay Lifetime of a Conjugated-Polymer Blend by Using a Scanning Near-Field Optical Microscope. *Advanced Materials* **2007**, *19*, 107-111.

16. Kwak, E. S.; Kang, T. J.; Bout, D. A. V., Fluorescence Lifetime Imaging with Near-Field Scanning Optical Microscopy. *Analytical Chemistry* **2001**, *73*, 3257-3262.

17. Kwak, E. S.; Kang, T. J.; Teetsov, J.; Vanden Bout, D. A., Fluorescence Lifetime Imaging of Organic Thin Films in near-Field Scanning Optical Microscopy. *Abstracts of Papers of the American Chemical Society* **2000**, *220*, U89-U89.

18. Seeland, M.; Rosch, R.; Hoppe, H., Luminescence Imaging of Polymer Solar Cells: Visualization of Progressing Degradation. *Journal of Applied Physics* **2011**, *109*, 064513-5.

19. Hoyer, U.; Pinna, L.; Swonke, T.; Auer, R.; Brabec, C. J.; Stubhan, T.; Li, N., Comparison of Electroluminescence Intensity and Photocurrent of Polymer Based Solar Cells. *Advanced Energy Materials* **2011**, *1*, 1097-1100.

20. Vandewal, K.; Tvingstedt, K.; Manca, J. V.; Ingana; x; s, O., Charge-Transfer States and Upper Limit of the Open-Circuit Voltage in Polymer:Fullerene Organic Solar Cells. *Selected Topics in Quantum Electronics, IEEE Journal of* **2010**, *16*, 1676-1684.

21. Liscio, A.; De Luca, G.; Nolde, F.; Palermo, V.; Mullen, K.; Samori, P., Photovoltaic Charge Generation Visualized at the Nanoscale: A Proof of Principle. *Journal of the American Chemical Society* **2007**, *130*, 780-781.

Bibliography

- Acciarri, M.; Binetti, S.; Racz, A.; Pizzini, S.; Agostinelli, G., Fast LBIC in-Line Characterization for Process Quality Control in the Photovoltaic Industry. *Solar Energy Materials and Solar Cells* **2002**, *72*, 417-424.
- Arias, A. C.; Corcoran, N.; Banach, M.; Friend, R. H.; MacKenzie, J. D.; Huck, W. T. S., Vertically Segregated Polymer-Blend Photovoltaic Thin-Film Structures through Surface-Mediated Solution Processing. *Applied Physics Letters* **2002**, *80*, 1695-1697.
- Arias, A. C.; MacKenzie, J. D.; Stevenson, R.; Halls, J. J. M.; Inbasekaran, M.; Woo, E. P.; Richards, D.; Friend, R. H., Photovoltaic Performance and Morphology of Polyfluorene Blends: A Combined Microscopic and Photovoltaic Investigation. *Macromolecules* **2001**, *34*, 6005-6013.
- Aruta, C.; D'Angelo, P.; Barra, M.; Ausanio, G.; Cassinese, A., Improved Structural Ordering in Sexithiophene Thick Films Grown on Single Crystal Oxide Substrates. *Applied Physics A: Materials Science and Processing* **2009**, *97*, 387-394.
- Barth, C.; Foster, A. S.; Henry, C. R.; Shluger, A. L., Recent Trends in Surface Characterization and Chemistry with High-Resolution Scanning Force Methods. *Advanced Materials* **2011**, *23*, 477-501.
- Brabec, C. J., Organic Photovoltaics: Technology and Market. *Solar Energy Materials and Solar Cells* **2004**, *83*, 273-292.
- Brabec, C. J.; Durrant, J. R., Solution-Processed Organic Solar Cells. *MRS Bulletin* **2008**, *33*, 670-675.
- Brabec, C. J.; Gowrisanker, S.; Halls, J. J. M.; Laird, D.; Jia, S.; Williams, S. P., Polymer–Fullerene Bulk-Heterojunction Solar Cells. *Advanced Materials* **2010**, *22*, 3839-3856.
- Bredas, J. L.; Norton, J. E.; Cornil, J.; Coropceanu, V., Molecular Understanding of Organic Solar Cells: The Challenges. *Accounts of Chemical Research* **2009**, *42*, 1691-1699.
- Bredas, J.-L.; Durrant, J. R., Organic Photovoltaics. *Accounts of Chemical Research* **2009**, *42*, 1689-1690.
- Brenner, T. J. K.; McNeill, C. R., Spatially Resolved Spectroscopic Mapping of Photocurrent and Photoluminescence in Polymer Blend Photovoltaic Devices. *Journal of Physical Chemistry C* **2011**, *115*, 19364-19370.

- Bull, T. A.; Pingree, L. S. C.; Jenekhe, S. A.; Ginger, D. S.; Luscombe, C. K., The Role of Mesoscopic PCBM Crystallites in Solvent Vapor Annealed Copolymer Solar Cells. *Acs Nano* **2009**, *3*, 627-636.
- Cadby, A. J.; Dean, R.; Elliott, C.; Jones, R. A. L.; Fox, A. M.; Lidzey, D. G., Imaging the Fluorescence Decay Lifetime of a Conjugated-Polymer Blend by Using a Scanning near-Field Optical Microscope. *Advanced Materials* **2007**, *19*, 107-111.
- Cadby, A.; Khalil, G.; Fox, A. M.; Lidzey, D. G., Mapping Exciton Quenching in Photovoltaic-Applicable Polymer Blends Using Time-Resolved Scanning near-Field Optical Microscopy. *Journal of Applied Physics* **2008**, *103*, 093715.
- Cai, W. Z.; Gong, X.; Cao, Y., Polymer Solar Cells: Recent Development and Possible Routes for Improvement in the Performance. *Solar Energy Materials and Solar Cells* **2010**, *94*, 114-127.
- Chiesa, M.; Burgi, L.; Kim, J. S.; Shikler, R.; Friend, R. H.; Sirringhaus, H., Correlation between Surface Photovoltage and Blend Morphology in Polyfluorene-Based Photodiodes. *Nano Letters* **2005**, *5*, 559-563.
- Clark, J.; Chang, J. F.; Spano, F. C.; Friend, R. H.; Silva, C., Determining Exciton Bandwidth and Film Microstructure in Polythiophene Films Using Linear Absorption Spectroscopy. *Applied Physics Letters* **2009**, *94*, 163306.
- Clark, J.; Silva, C.; Friend, R. H.; Spano, F. C., Role of Intermolecular Coupling in the Photophysics of Disordered Organic Semiconductors: Aggregate Emission in Regioregular Polythiophene. *Physical Review Letters* **2007**, *98*, 206406.
- Coffey, D. C.; Ginger, D. S., Time-Resolved Electrostatic Force Microscopy of Polymer Solar Cells. *Nature Materials* **2006**, *5*, 735-740.
- Coffey, D. C.; Reid, O. G.; Rodovsky, D. B.; Bartholomew, G. P.; Ginger, D. S., Mapping Local Photocurrents in Polymer/Fullerene Solar Cells with Photoconductive Atomic Force Microscopy. *Nano Letters* **2007**, *7*, 738-744.
- Dang, X. D.; Tamayo, A. B.; Seo, J.; Hoven, C. V.; Walker, B.; Nguyen, T. Q., Nanostructure and Optoelectronic Characterization of Small Molecule Bulk Heterojunction Solar Cells by Photoconductive Atomic Force Microscopy. *Advanced Functional Materials* **2010**, *20*, 3314-3321.
- Dante, M.; Peet, J.; Nguyen, T. Q., Nanoscale Charge Transport and Internal Structure of Bulk Heterojunction Conjugated Polymer/Fullerene Solar Cells by Scanning Probe Microscopy. *Journal of Physical Chemistry C* **2008**, *112*, 7241-7249.
- Dennler, G.; Scharber, M. C.; Brabec, C. J., Polymer-Fullerene Bulk-Heterojunction Solar Cells. *Advanced Materials* **2009**, *21*, 1323-1338.

- Derkaoui, Z.; Kebbab, Z.; Miloua, R.; Benramdane, N., Theoretical Study of Optical Characteristics of Multilayer Coatings ZnO/CdS/CdTe Using First-Principles Calculations. *Solid State Communications* **2009**, *149*, 1231-1235.
- Douheret, O.; Swinnen, A.; Bertho, S.; Haeldermans, I.; D'Haen, J.; D'Olieslaeger, M.; Vanderzande, D.; Manca, J. V., High-Resolution Morphological and Electrical Characterisation of Organic Bulk Heterojunction Solar Cells by Scanning Probe Microscopy. *Progress in Photovoltaics* **2007**, *15*, 713-726.
- Durose, K.; Asher, S. E.; Jaegermann, W.; Levi, D.; McCandless, B. E.; Metzger, W.; Moutinho, H.; Paulson, P. D.; Perkins, C. L.; Sites, J. R.; Teeter, G.; Terheggen, M., Physical Characterization of Thin-Film Solar Cells. *Progress in Photovoltaics* **2004**, *12*, 177-217.
- Facchetti, A., Pi-Conjugated Polymers for Organic Electronics and Photovoltaic Cell Applications. *Chemical Materials* **2011**, *23*, 733-758.
- Fujihira, M., Kelvin Probe Force Microscopy of Molecular Surfaces. *Annual Review of Materials Science* **1999**, *29*, 353-380.
- Gao, J.; Grey, J. K., Spectroscopic Studies of Energy Transfer in Fluorene Co-Polymer Blend Nanoparticles. *Chemical Physical Letters* **2012**, *522*, 86-91.
- Gao, Y. Q.; Grey, J. K., Resonance Chemical Imaging of Polythiophene/Fullerene Photovoltaic Thin Films: Mapping Morphology-Dependent Aggregated and Unaggregated C=C Species. *Journal of American Chemical Society* **2009**, *131*, 9654-9662.
- Gao, Y. Q.; Martin, T. P.; Niles, E. T.; Wise, A. J.; Thomas, A. K.; Grey, J. K., Understanding Morphology-Dependent Polymer Aggregation Properties and Photocurrent Generation in Polythiophene/Fullerene Solar Cells of Variable Compositions. *Journal of Physical Chemistry C* **2010**, *114*, 15121-15128.
- Gao, Y. Q.; Martin, T. P.; Thomas, A. K.; Grey, J. K., Resonance Raman Spectroscopic and Photocurrent Imaging of Polythiophene/Fullerene Solar Cells. *Journal of Physical Chemistry Letters* **2010**, *1*, 178-182.
- Gearba, R. I.; Mills, T.; Morris, J.; Pindak, R.; Black, C. T.; Zhu, X. Y., Quantifying Interfacial Electric Fields and Local Crystallinity in Polymer-Fullerene Bulk-Heterojunction Solar Cells. *Advanced Functional Materials* **2011**, *21*, 2666-2673.
- Gierschner, J.; Huang, Y. S.; Van Averbeke, B.; Cornil, J.; Friend, R. H.; Beljonne, D., Excitonic *Versus* Electronic Couplings in Molecular Assemblies: The Importance of Non-Nearest Neighbor Interactions. *Journal of Chemical Physics* **2009**, *130*, 044105.

- Giridharagopal, R.; Ginger, D. S., Characterizing Morphology in Bulk Heterojunction Organic Photovoltaic Systems. *Journal of Physical Chemistry Letters* **2010**, *1*, 1160-1169.
- Goetzberger, A.; Hebling, C.; Schock, H. W., Photovoltaic Materials, History, Status and Outlook. *Materials Science & Engineering R-Reports* **2003**, *40*, 1-46.
- Groves, C.; Reid, O. G.; Ginger, D. S., Heterogeneity in Polymer Solar Cells: Local Morphology and Performance in Organic Photovoltaics Studied with Scanning Probe Microscopy. *Accounts of Chemical Research* **2010**, *43*, 612-620.
- Gunes, S.; Neugebauer, H.; Sariciftci, N. S., Conjugated Polymer-Based Organic Solar Cells. *Chemical Reviews* **2007**, *107*, 1324-1338.
- Gupta, D.; Bag, M.; Narayan, K. S., Correlating Reduced Fill Factor in Polymer Solar Cells to Contact Effects. *Applied Physics Letters* **2008**, *92*, 093301.
- Hallermann, M.; Haneder, S.; Da Como, E., Charge-Transfer States in Conjugated Polymer/Fullerene Blends: Below-Gap Weakly Bound Excitons for Polymer Photovoltaics. *Applied Physics Letters* **2008**, *93*, 053307-3.
- Heremans, P.; Cheyns, D.; Rand, B. P., Strategies for Increasing the Efficiency of Heterojunction Organic Solar Cells: Material Selection and Device Architecture. *Accounts of Chemical Research* **2009**, *42*, 1740-1747.
- Hibberd, C. J.; Chassaing, E.; Liu, W.; Mitzi, D. B.; Lincot, D.; Tiwari, A. N., Non-Vacuum Methods for Formation of Cu(In,Ga)(Se,S)$_2$ Thin Film Photovoltaic Absorbers. *Progress in Photovoltaics: Research and Applications* **2010**, *18*, 434-452.
- Hoppe, H.; Glatzel, T.; Niggemann, M.; Hinsch, A.; Lux-Steiner, M. C.; Sariciftci, N. S., Kelvin Probe Force Microscopy Study on Conjugated Polymer/Fullerene Bulk Heterojunction Organic Solar Cells. *Nano Letters* **2005**, *5*, 269-274.
- Hoyer, U.; Pinna, L.; Swonke, T.; Auer, R.; Brabec, C. J.; Stubhan, T.; Li, N., Comparison of Electroluminescence Intensity and Photocurrent of Polymer Based Solar Cells. *Advanced Energy Materials* **2011**, *1*, 1097-1100.
- Hoyer, U.; Wagner, M.; Swonke, T.; Bachmann, J.; Auer, R.; Osvet, A.; Brabec, C. J., Electroluminescence Imaging of Organic Photovoltaic Modules. *Applied Physics Letters* **2010**, *97*, 233303.
- Huang, Y. S.; Westenhoff, S.; Avilov, I.; Sreearunothai, P.; Hodgkiss, J. M.; Deleener, C.; Friend, R. H.; Beljonne, D., Electronic Structures of Interfacial States Formed at Polymeric Semiconductor Heterojunctions. *Nature Materials* **2008**, *7*, 483-489.

- Johnston, S.; Repins, I.; Call, N.; Sundaramoorthy, R.; Jones, K. M.; To, B. In *Applications of Imaging Techniques to Si, Cu(In,Ga)Se_2, and CdTe and Correlation to Solar Cell Parameters*, Photovoltaic Specialists Conference (PVSC), 2010 35th IEEE, 20-25 June 2010; 2010; pp 001727-001732.
- Kaake, L. G.; Barbara, P. F.; Zhu, X. Y., Intrinsic Charge Trapping in Organic and Polymeric Semiconductors: A Physical Chemistry Perspective. *Journal of Physical Chemistry Letters* **2010**, *1*, 628-635.
- Kamat, P. V., Meeting the Clean Energy Demand: Nanostructure Architectures for Solar Energy Conversion. *Journal of Physical Chemistry C* **2007**, *111*, 2834-2860.
- Kamat, P. V., Quantum Dot Solar Cells. Semiconductor Nanocrystals as Light Harvesters. *Journal of Physical Chemistry C* **2008**, *112*, 18737-18753.
- Kietzke, T.; Neher, D.; Kumke, M.; Montenegro, R.; Landfester, K.; Scherf, U., A Nanoparticle Approach to Control the Phase Separation in Polyfluorene Photovoltaic Devices. *Macromolecules* **2004**, *37*, 4882-4890.
- Kim, J.-S.; Ho, P. K. H.; Murphy, C. E.; Friend, R. H., Phase Separation in Polyfluorene-Based Conjugated Polymer Blends: Lateral and Vertical Analysis of Blend Spin-Cast Thin Films. *Macromolecules* **2004**, *37*, 2861-2871.
- Krebs, F. C., Fabrication and Processing of Polymer Solar Cells: A Review of Printing and Coating Techniques. *Solar Energy Materials and Solar Cells* **2009**, *93*, 394-412.
- Krebs, F. C.; Tromholt, T.; Jorgensen, M., Upscaling of Polymer Solar Cell Fabrication Using Full Roll-to-Roll Processing. *Nanoscale* **2010**, *2*, 873-886.
- Kwak, E. S.; Kang, T. J.; Bout, D. A. V., Fluorescence Lifetime Imaging with Near-Field Scanning Optical Microscopy. *Analytical Chemistry* **2001**, *73*, 3257-3262.
- Kwak, E. S.; Kang, T. J.; Teetsov, J.; Vanden Bout, D. A., Fluorescence Lifetime Imaging of Organic Thin Films in Near-Field Scanning Optical Microscopy. *Abstracts of Papers of the American Chemical Society* **2000**, *220*, U89-U89.
- Leclere, P.; Surin, M.; Brocorens, P.; Cavallini, M.; Biscarini, F.; Lazzaroni, R., Supramolecular Assembly of Conjugated Polymers: From Molecular Engineering to Solid-State Properties. *Materials Science and Engineering R* **2006**, *55*, 1-56.
- Liscio, A.; De Luca, G.; Nolde, F.; Palermo, V.; Mullen, K.; Samori, P., Photovoltaic Charge Generation Visualized at the Nanoscale: A Proof of Principle. *Journal of the American Chemical Society* **2007**, *130*, 780-781.
- Liscio, A.; Palermo, V.; Fenwick, O.; Braun, S.; Mullen, K.; Fahlman, M.; Cacialli, F.; Samori, P., Local Surface Potential of Pi-Conjugated Nanostructures

by Kelvin Probe Force Microscopy: Effect of the Sampling Depth. *Small* **2011**, *7*, 634-639.

- Liscio, A.; Palermo, V.; Samori, P., Nanoscale Quantitative Measurement of the Potential of Charged Nanostructures by Electrostatic and Kelvin Probe Force Microscopy: Unraveling Electronic Processes in Complex Materials. *Accounts of Chemical Research* **2010**, *43*, 541-550.
- Liscio, A.; Palermo, V.; Samori, P., Probing Local Surface Potential of Quasi-One-Dimensional Systems: A KPFM Study of P3HT Nanofibers. *Advanced Functional Materials* **2008**, *18*, 907-914.
- Lloyd, M. T.; Anthony, J. E.; Malliaras, G. G., Photovoltaics from Soluble Small Molecules. *Materials Today* **2007**, *10*, 34-41.
- Maldonado, S.; Smith, T. J.; Williams, R. D.; Morin, S.; Barton, E.; Stevenson, K. J., Surface Modification of Indium Tin Oxide Via Electrochemical Reduction of Aryldiazonium Cations. *Langmuir* **2006**, *22*, 2884-2891.
- McCandless, B. E.; Shafarman, W. N. Chemical Surface Deposition of Ultra-Thin Semiconductors. U.S. Patent 6,537,845, March 25, 2003.
- McNeill, C. R.; Frohne, H.; Holdsworth, J. L.; Dastoor, P. C., Direct Influence of Morphology on Current Generation in Conjugated Polymer:Methanofullerene Solar Cells Measured by Near-Field Scanning Photocurrent Microscopy. *Synthetic Metals* **2004**, *147*, 101-104.
- McNeill, C. R.; Frohne, H.; Holdsworth, J. L.; Dastoor, P. C., Near-Field Scanning Photocurrent Measurements of Polyfluorene Blend Devices: Directly Correlating Morphology with Current Generation. *Nano Letters* **2004**, *4*, 2503-2507.
- McNeill, C. R.; Frohne, H.; Holdsworth, J. L.; Furst, J. E.; King, B. V.; Dastoor, P. C., Direct Photocurrent Mapping of Organic Solar Cells Using a Near-Field Scanning Optical Microscope. *Nano Letters* **2004**, *4*, 219-223.
- McNeill, C. R.; Greenham, N. C., Conjugated-Polymer Blends for Optoelectronics. *Advanced Materials* **2009**, *21*, 3840-3850.
- McNeill, C. R.; Watts, B.; Swaraj, S.; Ade, H.; Thomsen, L.; Belcher, W.; Dastoor, P. C., Evolution of the Nanomorphology of Photovoltaic Polyfluorene Blends: Sub-100 nm Resolution with X-Ray Spectromicroscopy. *Nanotechnology* **2008**, *19*, 424015.
- McNeill, C. R.; Watts, B.; Thomsen, L.; Ade, H.; Greenham, N. C.; Dastoor, P. C., X-Ray Microscopy of Photovoltaic Polyfluorene Blends: Relating Nanomorphology to Device Performance. *Macromolecules* **2007**, *40*, 3263-3270.

- McNeill, C. R.; Watts, B.; Thomsen, L.; Belcher, W. J.; Greenham, N. C.; Dastoor, P. C.; Ade, H., Evolution of Laterally Phase-Separated Polyfluorene Blend Morphology Studied by X-Ray Spectromicroscopy. *Macromolecules* **2009**, *42*, 3347-3352.
- McNeill, C. R.; Watts, B.; Thomsen, L.; Belcher, W. J.; Kilcoyne, A. L. D.; Greenham, N. C.; Dastoor, P. C., X-Ray Spectromicroscopy of Polymer/Fullerene Composites: Quantitative Chemical Mapping. *Small* **2006**, *2*, 1432-1435.
- McNeill, C. R.; Westenhoff, S.; Groves, C.; Friend, R. H.; Greenham, N. C., Influence of Nanoscale Phase Separation on the Charge Generation Dynamics and Photovoltaic Performance of Conjugated Polymer Blends: Balancing Charge Generation and Separation. *Journal of Physical Chemistry C* **2007**, *111*, 19153-19160.
- Melitz, W.; Shen, J.; Kummel, A. C.; Lee, S., Kelvin Probe Force Microscopy and Its Application. *Surface Science Reports* **2011**, *66*, 1-27.
- Milner, R. G.; Arias, A. C.; Stevenson, R.; Mackenzie, J. D.; Richards, D.; Friend, R. H.; Kang, D. J.; Blamire, M., Phase Separation in Polyfluorene Blends Investigated with Complementary Scanning Probe Microscopies. *Materials Science and Technology-London* **2002**, *18*, 759-762.
- Mitzi, D. B.; Yuan, M.; Liu, W.; Kellock, A. J.; Chey, S. J.; Deline, V.; Schrott, A. G., A High-Efficiency Solution-Deposited Thin-Film Photovoltaic Device. *Advanced Materials* **2008**, *20*, 3657-3662.
- Mohn, F.; Gross, L.; Moll, N.; Meyer, G., Imaging the Charge Distribution within a Single Molecule. *Nature Nanotechnology* **2012**, DOI: 10.1038/NNANO.2012.20.
- Morteani, A. C.; Friend, R. H.; Silva, C., Exciton Trapping at Heterojunctions in Polymer Blends. *The Journal of Chemical Physics* **2005**, *122*, 244906.
- Nozik, A. J., Quantum Dot Solar Cells. *Physica E-Low-Dimensional Systems & Nanostructures* **2002**, *14*, 115-120.
- Olson, D. C.; Shaheen, S. E.; Collins, R. T.; Ginley, D. S., The Effect of Atmosphere and ZnO Morphology on the Performance of Hybrid Poly(3-hexylthiophene)/Zno Nanofiber Photovoltaic Devices. *J. Phys. Chem. C* **2007**, *111*, 16670-16678.
- Ostrowski, D. P.; Glaz, M. S.; Goodfellow, B. W.; Akhavan, V. A.; Panthani, M. G.; Korgel, B. A.; Vanden Bout, D. A., Mapping Spatial Heterogeneity in $Cu(In_{1-X}Ga_x)Se_2$ Nanocrystal-Based Photovoltaics with Scanning Photocurrent and Fluorescence Microscopy. *Small* **2010**, *6*, 2832-2836.

- Ostrowski, D. P.; Lytwak, L. A.; Mejia, M. L.; Stevenson, K. J.; Holliday, B. J.; Vanden Bout, D. A., The Effects of Aggregation on Electronic and Optical Properties of Oligothiophene Particles. *Acs Nano* **2012**, *6*, 5507-5513.
- Palermo, V.; Liscio, A.; Palma, M.; Surin, M.; Lazzaroni, R.; Samori, P., Exploring Nanoscale Electrical and Electronic Properties of Organic and Polymeric Functional Materials by Atomic Force Microscopy Based Approaches. *Chemical Communications* **2007**, 3326-3337.
- Palermo, V.; Otten, M. B. J.; Liscio, A.; Schwartz, E.; de Witte, P. A. J.; Castriciano, M. A.; Wienk, M. M.; Nolde, F.; De Luca, G.; Cornelissen, J. J. L. M.; Janssen, R. A. J.; Müllen, K.; Rowan, A. E.; Nolte, R. J. M.; Samori, P., The Relationship between Nanoscale Architecture and Function in Photovoltaic Multichromophoric Arrays as Visualized by Kelvin Probe Force Microscopy. *Journal of the American Chemical Society* **2008**, *130*, 14605-14614.
- Palermo, V.; Palma, M.; Samori, P., Electronic Characterization of Organic Thin Films by Kelvin Probe Force Microscopy. *Advanced Materials* **2006**, *18*, 145-164.
- Panthani, M. G.; Akhavan, V.; Goodfellow, B.; Schmidtke, J. P.; Dunn, L.; Dodabalapur, A.; Barbara, P. F.; Korgel, B. A., Synthesis of $CuInS_2$, $CuInSe_2$, and $Cu(In_xGa_{1-X})Se_2$ (CIGS) Nanocrystal "Inks" for Printable Photovoltaics. *J Am Chem Soc* **2008**, *130*, 16770-16777.
- Peet, J.; Heeger, A. J.; Bazan, G. C., "Plastic" Solar Cells: Self-Assembly of Bulk Heterojunction Nanomaterials by Spontaneous Phase Separation. *Accounts of Chemical Research* **2009**, *42*, 1700-1708.
- Pingree, L. S. C.; Reid, O. G.; Ginger, D. S., Electrical Scanning Probe Microscopy on Active Organic Electronic Devices. *Advanced Materials* **2009**, *21*, 19-28.
- Pingree, L. S. C.; Reid, O. G.; Ginger, D. S., Imaging the Evolution of Nanoscale Photocurrent Collection and Transport Networks During Annealing of Polythiophene/Fullerene Solar Cells. *Nano Letters* **2009**, *9*, 2946-2952.
- Po, R.; Maggini, M.; Camaioni, N., Polymer Solar Cells: Recent Approaches and Achievements. *Journal of Physical Chemistry C* **2010**, *114*, 695-706.
- Puntambekar, K.; Dong, J. P.; Haugstad, G.; Frisbie, C. D., Structural and Electrostatic Complexity at a Pentacene/Insulator Interface. *Advanced Functional Materials* **2006**, *16*, 879-884.
- Ramon, J. G. S.; Bittner, E. R., Exciton Regeneration Dynamics in Model Donor-Acceptor Polymer Heterojunctions. *Journal of Physical Chemistry B* **2006**, *110*, 21001-21009.

- Reid, O. G.; Munechika, K.; Ginger, D. S., Space Charge Limited Current Measurements on Conjugated Polymer Films Using Conductive Atomic Force Microscopy. *Nano Letters* **2008**, *8*, 1602-1609.
- Reid, O. G.; Rayermann, G. E.; Coffey, D. C.; Ginger, D. S., Imaging Local Trap Formation in Conjugated Polymer Solar Cells: A Comparison of Time-Resolved Electrostatic Force Microscopy and Scanning Kelvin Probe Imaging†. *The Journal of Physical Chemistry C* **2010**, *114*, 20672-20677.
- Repins, I.; Contreras, M. A.; Egaas, B.; DeHart, C.; Scharf, J.; Perkins, C. L.; To, B.; Noufi, R., 19.9%-Efficient Zno/Cds/$CuInGaSe_2$ Solar Cell with 81.2% Fill Factor. *Progress in Photovoltaics* **2008**, *16*, 235-239.
- Riehn, R.; Stevenson, R.; Richards, D.; Kang, D. J.; Blamire, M.; Downes, A.; Cacialli, F., Local Probing of Photocurrent and Photoluminescence in a Phase-Separated Conjugated-Polymer Blend by Means of Near-Field Excitation. *Advanced Functional Materials* **2006**, *16*, 469-476.
- Romero, M. J.; Morfa, A. J.; Reilly, T. H., III; van de Lagemaat, J.; Al-Jassim, M., Nanoscale Imaging of Exciton Transport in Organic Photovoltaic Semiconductors by Tip-Enhanced Tunneling Luminescence. *Nano Letters* **2009**, *9*, 3904-3908.
- Roncali, J.; Leriche, P.; Cravino, A., From One to Three-Dimensional Organic Semiconductors: In Search of the Organic Silicon? *Advanced Materials* **2007**, *19*, 2045-2060.
- Rozanski, L. J.; Cone, C. W.; Ostrowski, D. P.; Bout, D. A. V., Effect of Film Morphology on the Energy Transfer to Emissive Green Defects in Dialkyl Polyfluorenes. *Macromolecules* **2007**, *40*, 4524-4529.
- Saunders, B. R.; Turner, M. L., Nanoparticle-Polymer Photovoltaic Cells. *Advances in Colloid and Interface Science* **2008**, *138*, 1-23.
- Seeland, M.; Rosch, R.; Hoppe, H., Luminescence Imaging of Polymer Solar Cells: Visualization of Progressing Degradation. *Journal of Applied Physics* **2011**, *109*, 064513-5.
- Seeland, M.; Rosch, R.; Hoppe, H., Quantitative Analysis of Electroluminescence Images from Polymer Solar Cells. *Journal of Applied Physics* **2012**, *111*, 024505-5.
- Sherwood, G. A.; Cheng, R.; Chacon-Madrid, K.; Smith, T. M.; Peteanu, L. A.; Wildeman, J., Chain Length and Substituent Effects on the Formation of Excimer-Like States in Nanoaggregates of CN-PPV Model Oligomers. *Journal of Physical Chemistry C* **2010**, *114*, 12078-12089.

- Shikler, R.; Chiesa, M.; Friend, R. H., Photovoltaic Performance and Morphology of Polyfluorene Blends: The Influence of Phase Separation Evolution. *Macromolecules* **2006**, *39*, 5393-5399.
- Snaith, H. J.; Arias, A. C.; Morteani, A. C.; Silva, C.; Friend, R. H., Charge Generation Kinetics and Transport Mechanisms in Blended Polyfluorene Photovoltaic Devices. *Nano Letters* **2002**, *2*, 1353-1357.
- Spanggaard, H.; Krebs, F. C., A Brief History of the Development of Organic and Polymeric Photovoltaics. *Solar Energy Materials and Solar Cells* **2004**, *83*, 125-146.
- Spano, F. C., Modeling Disorder in Polymer Aggregates: The Optical Spectroscopy of Regioregular Poly(3-hexylthiophene) Thin Films. *Journal of Chemical Physics* **2005**, *122*, 234701.
- Spano, F. C., The Spectral Signatures of Frenkel Polarons in H- and J-Aggregates. *Accounts of Chemical Research* **2010**, *43*, 429-439.
- Spano, F. C.; Clark, J.; Silva, C.; Friend, R. H., Determining Exciton Coherence from the Photoluminescence Spectral Line Shape in Poly(3-Hexylthiophene) Thin Films. *Journal of Chemical Physics* **2009**, *130*, 074904.
- Spano, F. C.; Yamagata, H., Vibronic Coupling in J-Aggregates and Beyond: A Direct Means of Determining the Exciton Coherence Length from the Photoluminescence Spectrum. *Journal of Physical Chemistry B* **2011**, *115*, 5133-5143.
- Stevenson, R.; Arias, A. C.; Ramsdale, C.; MacKenzie, J. D.; Richards, D., Raman Microscopy Determination of Phase Composition in Polyfluorene Composites. *Applied Physics Letters* **2001**, *79*, 2178-2180.
- Sugimura, H.; Hayashi, K.; Saito, N.; Nakagiri, N.; Takai, O., Surface Potential Microscopy for Organized Molecular Systems. *Applied Surface Science* **2002**, *188*, 403-410.
- Swaraj, S.; Wang, C.; Yan, H. P.; Watts, B.; Jan, L. N.; McNeill, C. R.; Ade, H., Nanomorphology of Bulk Heterojunction Photovoltaic Thin Films Probed with Resonant Soft X-Ray Scattering. *Nano Letters* **2010**, *10*, 2863-2869.
- Tang, J. A.; Sargent, E. H., Infrared Colloidal Quantum Dots for Photovoltaics: Fundamentals and Recent Progress. *Advanced Materials* **2011**, *23*, 12-29.
- Taylor, D. M.; Bayes, G. F., Calculating the Surface-Potential of Unionized Monolayers. *Physical Review E* **1994**, *49*, 1439-1449.
- Teetsov, J.; Vanden Bout, D. A., Near-Field Scanning Optical Microscopy Studies of Nanoscale Order in Thermally Annealed Films of Poly(9,9-diakylfluorene). *Langmuir* **2002**, *18*, 897-903.

- Teetsov, J.; Vanden Bout, D. A., Near-Field Scanning Optical Microscopy (NSOM) Studies of Nanoscale Polymer Ordering in Pristine Films of Poly(9,9-dialkylfluorene). *Journal of Physical Chemistry B* **2000**, *104*, 9378-9387.
- Thantsha, N. M.; Macabebe, E. Q. B.; Vorster, F. J.; van Dyk, E. E., Opto-Electronic Analysis of Silicon Solar Cells by Lbic Investigations and Current-Voltage Characterization. *Physica B-Condensed Matter* **2009**, *404*, 4445-4448.
- Tvingstedt, K.; Vandewal, K.; Gadisa, A.; Zhang, F.; Manca, J.; Inganäs, O., Electroluminescence from Charge Transfer States in Polymer Solar Cells. *Journal of American Chemical Society* **2009**, *131*, 11819-11824.
- Vandewal, K.; Tvingstedt, K.; Manca, J. V.; Ingana; x; s, O., Charge-Transfer States and Upper Limit of the Open-Circuit Voltage in Polymer:Fullerene Organic Solar Cells. *Selected Topics in Quantum Electronics, IEEE Journal of* **2010**, *16*, 1676-1684.
- Walker, B.; Kim, C.; Nguyen, T. Q., Small Molecule Solution-Processed Bulk Heterojunction Solar Cells. *Chemistry of Materials* **2011**, *23*, 470-482.
- Watkins, P. K.; Walker, A. B.; Verschoor, G. L. B., Dynamical Monte Carlo Modelling of Organic Solar Cells: The Dependence of Internal Quantum Efficiency on Morphology. *Nano Letters* **2005**, *5*, 1814-1818.
- Watts, B.; Schuettfort, T.; McNeill, C. R., Mapping of Domain Orientation and Molecular Order in Polycrystalline Semiconducting Polymer Films with Soft X-Ray Microscopy. *Advanced Functional Materials* **2011**, *21*, 1122-1131.
- Wetzelaer, G.-J. A. H.; Kuik, M.; Blom, P. W. M., Identifying the Nature of Charge Recombination in Organic Solar Cells from Charge-Transfer State Electroluminescence. *Advanced Energy Materials* **2012**, DOI: 10.1002/aenm.201200009.
- Yang, X.; Loos, J., Toward High-Performance Polymer Solar Cells: The Importance of Morphology Control. *Macromolecules* **2007**, *40*, 1353-1362.
- Zuppiroli, L.; Si-Ahmed, L.; Kamaras, K.; Nuesch, F.; Bussac, M. N.; Ades, D.; Siove, A.; Moons, E.; Gratzel, M., Self-Assembled Monolayers as Interfaces for Organic Opto-Electronic Devices. *Eur. Phys. J. B* **1999**, *11*, 505-512.